UCRL-13572

SUPERPLASTIC DEFORMATION AND HIGH TEMPERATURE CREEP OF A MONOTECTOID-COMPOSITION URANIUM-BASE ALLOY

P.O. 8424617

Donald Lee Bly

April 1973

SU-DMS-73-T-52

Department of MATERIALS SCIENCE AND ENGINEERING
STANFORD UNIVERSITY

SUPERPLASTIC DEFORMATION AND HIGH TEMPERATURE CREEP OF A MONOTECTOID-COMPOSITION URANIUM-BASE ALLOY

A DISSERTATION

SUBMITTED TO THE DEPARTMENT OF MATERIALS SCIENCE

AND ENGINEERING

AND THE COMMITTEE ON GRADUATE STUDIES

OF STANFORD UNIVERSITY

IN PARTIAL FULFILLMENT OF THE REQUIREMENTS

FOR THE DEGREE OF

DOCTOR OF PHILOSOPHY

By

Donald Lee Bly

April 1973

ABSTRACT

The elevated-temperature creep properties of a monotectoid-composition uranium-base alloy have been studied as a function of microstructure. The alloy used in this investigation, U-7.5Nb-2.5Zr (wt. pct), exists as a single γ phase above 637°C and transforms to a two-phase structure ($\alpha + \gamma_1$) below 637°C. Three areas of investigation were undertaken: (1) thermomechanical processing techniques to achieve a fine-grain equiaxed $\alpha + \gamma_1$ microstructure; (2) creep deformation of the fine-grain equiaxed $\alpha + \gamma_1$ structure; (3) creep deformation of the coarse-grain γ structure. Deformation behavior was studied using tension and compression tests performed in the temperature range 500 - 1000°C on an Instron machine using an inert atmosphere.

Deformation-enhanced spheroidization was studied as a technique to produce a fine-grain equiaxed microstructure from the lamellar $\alpha + \gamma_1$ structure formed by isothermal transformation. The spheroidization kinetics were slower than observed in a eutectoid-composition Fe-C alloy at the same homologous temperature and strain rate. Although incomplete spheroidization was observed after strains as large as $\varepsilon = 1.9$, the results were in qualitative agreement with spheroidization mechanisms proposed for steels.

A fine-grain equiaxed $\alpha + \gamma_1$ structure can be most efficiently produced by employing a quench-cold work-anneal treatment before hot working. An equiaxed structure with a 0.5 μm grain size was produced by gamma quenching, cold working to $\varepsilon \approx 0.5$, annealing at 550°C for

24 h and hot working at 600°C to $\varepsilon = 1.5$ (total strain).

The equiaxed $\alpha + \gamma_1$ structure with a stable 1.7 μm grain diameter was superplastic only at temperatures immediately below the monotectoid temperature. At 635°C, maximum elongations were about 550 pct. Superplastic creep was described by a phenomemological equation,

$$\frac{\dot{\gamma}\, k\, T}{D_B\, G\, b} = 485 \left(\frac{b}{d}\right)^2 \left(\frac{\tau}{G}\right)^2$$

for which general agreement with data of other superplastic materials is reported. In this equation $\dot{\gamma}$ is the shear strain rate, k is Boltzmann's constant, T is the absolute temperature, D_B is the grain boundary diffusion coefficient, G is the shear modulus, b is Burgers vector, d is the grain diameter and τ is the shear stress.

At high stresses where $\tau/G > 10^{-3}$ there was a transition from superplastic creep to dislocation climb-controlled creep where the stress exponent is 5. Creep data at 550 - 600°C were in this transition range centered at $\tau/G \cong 10^{-3}$, while data at 500 - 525°C exhibited only five-power creep.

Because the composition of the γ_1 phase changed significantly in the range 500 - 625°C and because the diffusion coefficient is sensitive to the Nb and Zr content, the diffusion coefficient in the γ_1 phase was strongly temperature-sensitive. An apparent activation energy for lattice diffusion at equilibrium γ_1 composition was calculated to be 130 kcal/mole between 500 and 625°C. This value was in good agreement with an average value of 123 kcal/mole calculated from creep data at 513 - 613°C. Therefore, in the dislocation climb region and the transition region, creep is believed to be controlled by lattice diffusion. The creep activation energy at 631°C was about 60 kcal/mole, which was

related to grain boundary diffusion and is consistent with superplastic creep behavior.

When annealed to form a single γ phase with a 40 μm grain size, the U-7.5Nb-2.5Zr alloy deformed by a viscous glide creep mechanism during initial straining ($\varepsilon = 0.01$) at 670 - 1000°C. The creep equation was found to be:

$$\frac{\dot{\gamma}\, k\, T}{D_L\, G\, b} = 11 \left(\frac{\tau}{G}\right)^3$$

where D_L is the lattice diffusion coefficient. Power law breakdown was found to occur at $\tau/G \cong 2 \times 10^{-3}$.

Structural changes occurred during deformation at 670 - 1000°C. At stresses less than about 1600 psi, hardening was observed which was related to subgrain formation and grain growth. At stresses greater than about 1600 psi, softening occurred. The softening was related to the formation of small recrystallized grains at grain boundaries, the probable mechanism being a grain boundary shear and migration process. Subgrains formed during deformation at all temperatures, especially near grain boundaries.

ACKNOWLEDGMENTS

I am grateful for the help and support of the faculty, students and staff at Stanford University. The author is especially indebted to his advisor, Professor Oleg D. Sherby, for his continued support, guidance and encouragement in this research program. I also wish to acknowledge the contributions of Professors William Nix and Craig Barrett through helpful discussions and the reading of the thesis.

Most of all, the author thanks his wife, Leanne, and son, Roger, for allowing me to undertake this endeavor. Their continued support during this sometimes trying period is deeply appreciated.

This research was supported by Lawrence Livermore Laboratory under contract number LRL 8424617. The author is grateful for the assistance given by staff members at Lawrence Livermore Laboratory, especially D. H. Wood, N. R. Borch, G. S. Root, L. W. Roberts and S. DiGiallonardo.

TABLE OF CONTENTS

TABLE OF CONTENTS (cont'd)

TABLE OF CONTENTS (cont'd)

LIST OF TABLES

LIST OF FIGURES

LIST OF FIGURES (cont'd)

LIST OF FIGURES (cont'd)

LIST OF FIGURES (cont'd)

LIST OF FIGURES (cont'd)

LIST OF FIGURES (cont'd)

LIST OF FIGURES (cont'd)

LIST OF FIGURES (cont'd)

CHAPTER I

INTRODUCTION

The objective of this investigation was to study the elevated temperature creep properties of a monotectoid-composition uranium-base alloy as a function of microstructure. The alloy used in this study, U-7.5Nb-2.5Zr (wt. pct), exists as a single γ phase above ≈637°C and transforms to a two-phase structure ($\alpha + \gamma_1$) below ≈637°C. Three areas of investigation were undertaken: (1) thermomechanical processing techniques, including deformation-enhanced spheroidization of the $\alpha + \gamma_1$ lamellar structure and special coldwork-anneal treatments, to achieve a fine-grain equiaxed $\alpha + \gamma_1$ microstructure; (2) creep deformation of the fine-grain equiaxed $\alpha + \gamma_1$ structure; (3) creep deformation in the single-phase region above ≈637°C.

During isothermal annealing below 637°C the U-7.5Nb-2.5Zr alloy transforms to a lamellar structure consisting of alternate plates of α and γ_1 phases. This structure will decompose during prolonged annealing to a structure consisting of a continuous γ phase matrix with spherical γ phase particles, the driving force being a reduction of interfacial energy. This spheroidization process is diffusion-controlled.

Recently it has been found that the kinetics of spheroidization can be greatly increased in the eutectoid steel system by concurrent deformation during annealing. In addition, Harrigan and Sherby (1971) showed that the particle spacing was a function of strain rate $\dot{\varepsilon}$ and temperature T of the form $\dot{\varepsilon}$ exp (Q/RT). The activation energy for deformation, Q, was found to be about that for grain boundary diffu-

sion in iron, suggesting that deformation-enhanced spheroidization is controlled by diffusion of iron atoms along grain or subgrain boundaries, dislocations or along interphase boundaries.

In the first part of this dissertation, spheroidization in the U-7.5Nb-2.5Zr alloy is examined as a function of temperature, strain and strain rate and compared to the results in steels. Because spheroidization rates are relatively slow in the uranium alloy, a quench-cold work-anneal treatment was also studied as a technique to use in conjunction with hot working to achieve a spheroidized microstructure.

Fine-grain equiaxed microstructures in two-phase materials are technologically important because they are very weak and ductile at high temperatures and very strong at room temperature. Superplastic deformation, which requires very low stresses for plastic flow, is usually observed in metals when the grain size is very fine ($<10\,\mu m$) and stable during deformation and when the temperature is greater than $0.5T_m$, where T_m is the absolute melting temperature. A two-phase microstructure can prevent grain growth during deformation at high temperatures. Superplastic flow is observed at low strain rates and provides excellent resistance to localized deformation (necking). A superplastic material can be used in intricate forming operations where large tensile strains are required. In addition, during hot forming operations where the strain rate is high, a fine-grain structure is weaker than a coarse-grain structure, thereby reducing the energy required for a forming operation.

Fine spheroidized structures can lead to high strength materials at low temperatures. For example, a pearlitic plain carbon steel has

a yield strength of 55,000 psi, but after rolling at 500°C to produce a spheroidized structure with an interparticle spacing of ≈0.3 μm, the yield strength is 175,000 psi [Sherby et al. (1969)]. Although elongation was only 1 pct, 10 pct elongation with a 125,000 psi yield strength can be achieved with a low temperature annealing treatment [Bly et al. (1973a)]. A spheroidized $\alpha + \gamma_1$ structure could offer improved strength and ductility properties at room temperature for the U-7.5Nb-2.5Zr alloy compared to a normally processed gamma-quenched and aged structure.

In the second and third parts of this dissertation, isothermal creep deformation in the U-7.5Nb-2.5Zr alloy is investigated for two structures: a two-phase equiaxed structure with a 1 μm grain size and a single-phase structure with a 40 μm grain size. The temperature ranges were $0.41T_m$ to $0.56T_m$ ($\alpha + \gamma_1$ structure) and $0.58T_m$ to $0.79T_m$ (γ structure). The objective was to understand the mechanisms by which plastic deformation takes place. Creep data are related to atom diffusion in the ternary system and phenomenological equations are developed to describe the deformation in terms of stress, strain rate, temperature, elastic modulus and grain size. The creep properties are related to microstructural observations and, in the $\alpha + \gamma_1$ region, the influence of fiber texture is discussed. Creep deformation of the U-7.5Nb-2.5Zr alloy is discussed in terms of Rachinger grain boundary sliding and dislocation climb-controlled creep in the $\alpha + \gamma_1$ region and dislocation glide-controlled creep in the γ region.

In terms of applications, U-7.5Nb-2.5Zr alloy was developed as a gamma-stabilized uranium-base alloy with a good combination of room temperature strength, ductility and corrosion resistance characteristics

[Peterson and Vandervoort (1964)]. Binary uranium-base alloys which are gamma-stabilized do not achieve the combination of desired engineering properties found in the U-7.5Nb-2.5Zr ternary alloy: U-Nb alloys have low strengths, U-Zr alloys are brittle and U-Mo alloys are subject to stress-corrosion cracking in oxygen environments. Isotropic physical properties resulting from cubic symmetry in the gamma phase (bcc crystal structure) are desired in nuclear applications. α-U, which has an orthorhombic crystal structure below 662°C, exhibits anisotropic physical properties leading to fabrication problems and dimensional instabilities during thermal cycling. The effect of thermal cycling on creep deformation in the gamma-quenched U-7.5Nb-2.5Zr alloy is complicated by the formation of a metastable γ^{O} phase (tetragonal crystal structure) and precipitation of an α'' phase (monoclinic crystal structure) at temperatures $T \geq 150^{\circ}C$ [Yakel (1969)]. The fine-grain $\alpha + \gamma_1$ structure, which is thermodynamically stable, could offer improved creep resistance during low-temperature thermal cycling compared to the structure prepared by gamma quenching. In non-nuclear applications, the U-7.5Nb-2.5Zr alloy is an excellent candidate for a high density material with high strength and good ductility characteristics.

CHAPTER II

REVIEW OF SUPERPLASTIC DEFORMATION THEORIES

This chapter provides an introduction to isothermal superplastic deformation characteristics and outlines the main theories proposed for superplastic creep. For more information, the reader is referred to the following recent review papers: Geckinli (1973), Nicholson (1972), Davies et al. (1970), Johnson (1970), Burke and Weiss (1970), Bird et al. (1969) and Backofen et al. (1968).

Also included in this chapter is a description of a technique to predict grain boundary diffusion coefficients in metals. This method is used later in the dissertation to estimate grain boundary diffusion coefficients in the U-7.5Nb-2.5Zr alloy, since these data have not been determined experimentally.

Superplastic Deformation Characteristics

The term "superplasticity" refers to large neck-free elongations obtained during low-stress deformation of certain metal structures. The requirements to achieve superplastic flow are a fine equiaxed grain size ($<10\ \mu m$) which is stable during deformation and test temperature T such that $T \geq 0.5T_m$, where T_m is the absolute melting temperature. To prevent rapid grain growth, a two-phase structure is normally required since this structure can only grow in size scale by agglomeration and Ostwald ripening. A fine-grain single-phase structure usually exhibits relatively rapid grain growth during high temperature deformation.

Superplastic creep is characterized by the following phenomenological equation:

$$\dot{\varepsilon} = \frac{A D \sigma^2}{L^2} \qquad (2\text{-}1)$$

where $\dot{\varepsilon}$ is the strain rate, A is a constant, D is the diffusion coefficient, L is the grain size and σ is the flow stress. The diffusion coefficient is usually reported to be that for grain boundary diffusion, although in Ni-Cr-Fe alloys lattice diffusion was found to be controlling deformation at temperatures $T > 0.65T_m$ [Hayden et al. (1972)]. The stress exponent is usually equal to 2, although various investigators have reported values within the range 1.3 to 3. The grain size exponent is most often given as 2, although values of 3 have been reported [Alden (1967) and Packer and Sherby (1967)]. Superplastic deformation following Eq. (2-1) is observed in the approximate stress range $2 \times 10^{-5} < \sigma/E < 2 \times 10^{-3}$, where E is the elastic modulus, although the limits of this range vary with both temperature and grain size [Vaidya et al. (1972)].

The resistance to local deformation in superplastic materials can be readily explained by the low stress exponent n compared to coarse-grain metals where, typically, n = 5. At constant temperature and grain size, steady state creep of metals can be described by the general equation,

$$\dot{\varepsilon} = k\sigma^n$$

where k is a constant and n is the stress exponent. In terms of load P and area A,

$$-\frac{1}{A}\frac{dA}{dt} = k\left(\frac{P}{A}\right)^n$$

or

$$-\frac{dA}{dt} = \frac{k P^n}{A^{n-1}}$$

For a given load and $n > 1$, deformation will be concentrated in the region of smallest cross-sectional area. But as n decreases from 5 to 1, the rate of local deformation as measured by dA/dt becomes less sensitive to the local cross-sectional area. Thus a reduction in n leads to a decrease in the rate of local deformation, which in turn gives greater

total elongations. At n = 1, deformation is Newtonian viscous and no necking occurs. For superplastic deformation where n = 2, total specimen elongations are 500 to 1000 pct engineering strain, depending on specimen geometry [Morrison (1968) and Woodford (1969)].

Microstructures of materials after superplastic deformation reveal that grains remain equiaxed. Grain boundaries are smooth and curved. Few dislocations are observed in the grains and no subgrain boundaries are formed. Slip lines are not seen on polished surfaces. Large amounts of grain boundary sliding and grain rotation are observed indirectly by displacements of surface scratches and directly during deformation in the scanning electron microscope [Dingley (1970) and Geckinli (1973)]. These observations indicate that grain boundary sliding occurs during superplastic flow and that strains produced by dislocation slip are minimal.

Diffusion Creep Mechanisms

In diffusion creep, strain is produced by vacancy diffusion in a stress gradient. In a tensile test, vacancies will flow from boundaries normal to the tensile axis to boundaries parallel to the tensile axis. Atom motion is in the reverse direction, leading to grains elongated in the tensile direction. If diffusion takes place within the grains the creep equation is [Nabarro (1948) and Herring (1950)]:

$$\dot{\varepsilon} = \frac{A \Omega D_L \sigma}{k T L^2}$$

where A is a constant about equal to 10, Ω is the atomic volume and D_L is the lattice diffusion coefficient. If diffusion occurs along grain boundaries, the equation is [Coble (1963)]:

$$\dot{\varepsilon} = \frac{A \Omega \delta D_B \sigma}{k T L^3}$$

where δ is the grain boundary width and $A \cong 75$. Although strain occurs from grain elongation, Stevens (1971) and Cannon (1972) showed that about 50 pct of the axial strain is due to grain boundary sliding which must accompany the grain shape change to prevent void formation.

The diffusion creep mechanism cannot explain superplastic flow because the stress exponent is not correct and grain elongation is not observed. Also, the Nabarro-Herring and Coble equations predict creep rates much lower than observed during superplastic deformation.

Dislocation Slip-Climb Mechanisms

Chaudhari (1967) proposed a model for superplastic creep based on the velocity of jogged screw dislocations as the rate-controlling mechanism. Dislocations are thought to move in an internal stress field governed by the dislocation density.

Packer et al. (1968) proposed a mechanism for superplastic deformation in which crystallographic slip occurs, but grains remain equiaxed by a continuous grain boundary migration or recrystallization process. Their evidence for dislocation slip was that initially textured specimens changed shape during superplastic flow from an originally circular cross section to an elliptical cross section. Only dislocation slip, or, perhaps, anisotropic grain boundary sliding, could account for this shape change.

Lee and Underwood (1970) postulated that a continuous dynamic recovery process operates during superplastic flow. A dislocation network is thought to form with well defined subboundaries acting as sources and sinks for dislocations. Strain is produced by dislocation slip or climb, but, since subboundaries continuously disintegrate and reform, dislocation tangles are not formed.

Hayden et al. (1972) have proposed a dislocation climb-controlled mechanism for superplastic creep. They assume about one dislocation source per grain, the area swept out by a gliding loop to be the cross sectional area of a grain, no dislocation pileups at grain boundaries and a climb height of 10b (b is Burgers vector) necessary to reduce the back stress on the source so that a new loop can be nucleated. At intermediate temperatures ($0.40T_m$ to $0.65T_m$), dislocation pipe diffusion could control dislocation climb rather than lattice diffusion. Hayden et al. suggest that their dislocation slip-climb model may control the accommodation process necessary for grain boundary sliding, and therefore control the overall deformation process.

The difficulty with dislocation models for superplastic creep is that there is little experimental evidence for dislocation activity during deformation that would support their theories. Recent experiments by Nicholson (1972) and Geckinli (1973) where superplastic creep behavior was not altered by the addition of small precipitate particles are strong evidence for the minimal contribution of dislocation slip to superplastic deformation. Nicholson noted that the distribution of inert markers was not disturbed after superplastic flow, except near grain boundaries.

Grain Boundary Sliding

There is no doubt that extensive grain boundary sliding occurs in superplastic creep, but, to prevent void formation, accommodation at grain corners is required. The accommodation mechanism is likely to be the rate-controlling step in the deformation process. Two possible accommodation mechanisms are dislocation slip and diffusional flow.

Grain deformation and recovery models of accommodation where dis-

location pileups are expected, such as that of Ball and Hutchison (1969), are not consistent with observed dislocation structures. One possible mechanism is that involving dislocation climb-glide of a distribution of dislocations along the grain boundary. Alden (1969) and Langdon (1970) have developed models of the form

$$\dot{\varepsilon} \propto \frac{D\,\sigma^2}{L}$$

for this process, with Alden and Langdon associating the diffusion coefficient D with grain boundary and lattice diffusion, respectively.

The diffusional flow accommodation mechanism is supported by Nicholson's (1972) marker experiments where denuded zones at randomly oriented grain boundaries were observed. Models for diffusional flow accommodated grain boundary sliding have been formulated by Gifkins (1967) and Geckinli (1973), but a stress exponent of one is predicted in contrast to n = 2 for superplastic flow.

Summary of Superplastic Deformation Theories

Grain boundary sliding with accommodation at grain corners is the mechanism most consistent with experimental observations for superplastic flow. The accommodation mechanism is probably largely diffusion controlled grain boundary migration, although no theory has been developed for this mechanism which agrees with observed creep behavior. Diffusion creep mechanisms do not predict the observed stress exponent (n = 2) and required grain elongation is not observed. Dislocation slip-climb mechanisms are possible, especially as related to accommodation processes for grain boundary sliding, but there is little experimental evidence of dislocation structures to support these models.

Prediction of Grain Boundary Diffusion Coefficients in Metals

The results of a correlation by Bly et al. (1973b) of all available grain boundary (D_B) and dislocation pipe (D_P) diffusion data for pure metals is shown in Fig. 2.1. The diffusion data are plotted as a function of reciprocal homologous temperature and all data are normalized to a grain boundary width δ of 5 Å. For dislocation pipe diffusion in low angle tilt boundaries, $\delta(\theta)$ was assumed to be 10 Å sin $\theta/2$; for twist boundaries, $\delta(\theta) = 20$ Å sin $\theta/2$. For comparison, bands showing the range of lattice [Sherby and Simnad (1961)] and liquid [Bly et al. (1973b)] diffusion data for pure metals are also shown in Fig. 2.1.

As plotted in Fig. 2.1, data for grain boundary and dislocation pipe diffusion are contained in one general band. Within the band there is no apparent difference between D_B and D_P data, or between bcc and fcc crystal structures. There is appreciable scatter in the D_B and D_P data, especially at low temperature, but this is not unexpected considering the experimental difficulties in measuring these quantities.

The best fit line to the D_B and D_P data is:

$$D_B = 1 \exp(-11T_m/T) \text{ cm}^2/\text{s} \qquad (2\text{-}2)$$

In Eq. (2-1), the pre-exponential coefficient (or frequency factor) is 1 cm^2/s which is essentially the same as for lattice diffusion. In addition, the activation energy for grain boundary diffusion, $Q_B = 11RT_m$, was found to be about 0.65 of that for lattice diffusion, although this ratio probably varies with crystal structure. It is concluded that Eq. (2-2) is the best method available for predicting grain boundary and dislocation pipe diffusion coefficients in metals.

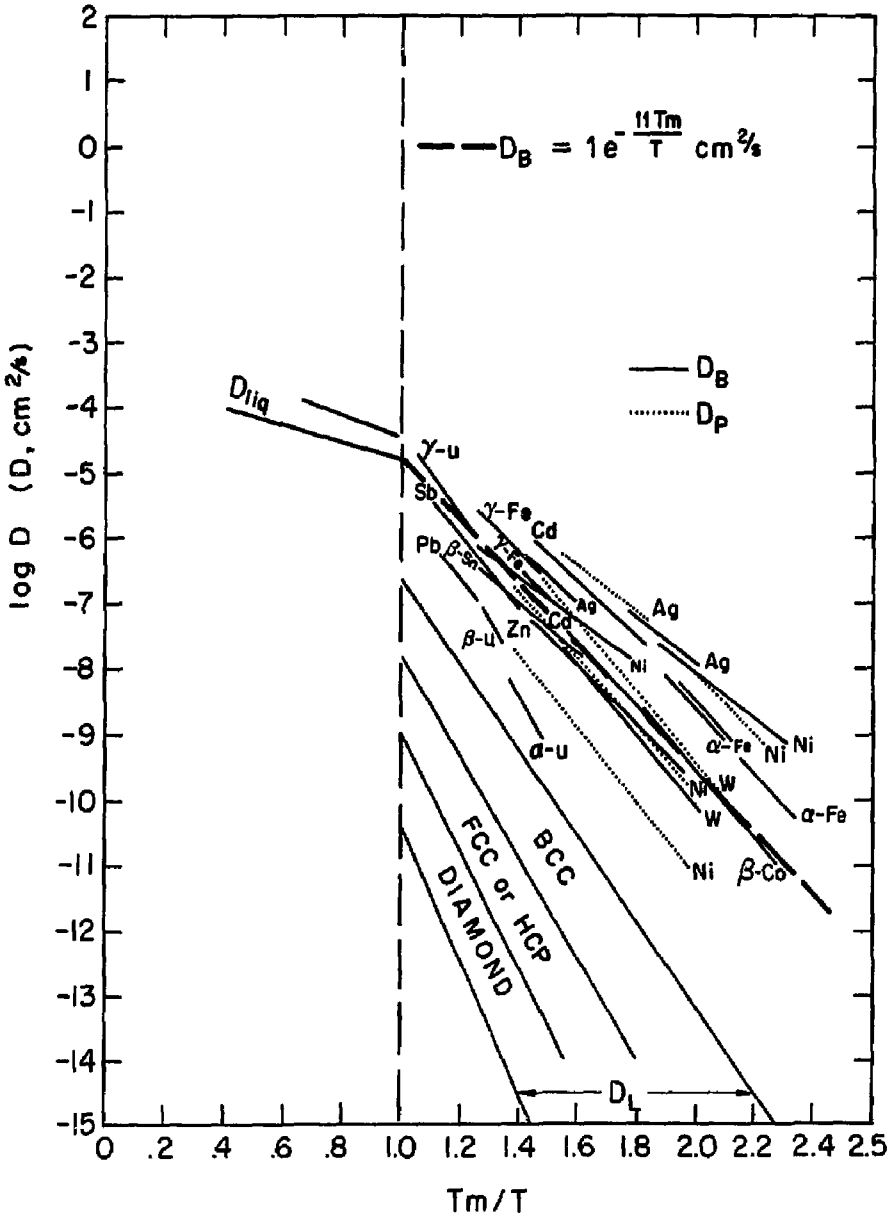

Fig. 2.1. Correlation of grain boundary (D_B) and dislocation pipe (D_p) diffusion data for pure metals. The best-fit line used to predict grain boundary and dislocation pipe diffusion coefficients in metals is shown.

CHAPTER III

EXPERIMENTAL PROCEDURE

In this chapter details of heat treatment, mechanical testing, metallography and fiber texture measurement procedures are presented. Information on the preparation and processing of the uranium alloy to obtain a microduplex structure is found in Chapter IV.

Heat Treatment

The heat treatments for U-7.5Nb-2.5Zr required protection against oxidation and the ability to water quench rapidly. Therefore, all samples to be heat treated were encapsulated in 19mm diameter quartz tubes in a vacuum of $\leq 5 \times 10^{-5}$ mm Hg. Preheated furnaces were employed to minimize the time required to reach the desired temperature, and rapid water quenching was obtained by quickly removing the capsule from the furnace and breaking it underwater.

Mechanical Testing

Two experimental set-ups were used to deform samples at 500 - 1000°C in an inert atmosphere of 99.999 pct argon (<3 ppm O_2+H_2O). The compression apparatus used small samples which maximized the amount of data determined from limited quantities of material and eliminated instability problems caused by necking. The tension apparatus produced several superplastically extended specimens with total elongations in excess of 500 pct, but uniform flow stress and strain data were limited to low values of strain before local necking occurred. Both the compression and the tension apparatus were used on a model TTC-L Instron machine with tall frame and push-button crosshead speed controls. With the variable speed drive attachment, crosshead speeds ranged from 2 to

0.00008 in./min.

Compression Apparatus

With the requirements of rigid platen support under high load conditions, inert atmosphere, and minimal sample insertion and heating times, a "cage" type assembly was constructed. This construction allows the lower platen to be supported below the crosshead by the cage, with the upper platen held by a central push rod which extends through a hole in the crosshead to the load cell mounted on top of the Instron frame. A furnace or temperature bath can then be raised to cover the specimen area. The cage in Fig. 3.1 is a thick-walled tube of In-600 material, 2 1/2 in. O.D. x 14 in. long, and the push rod is 0.975 in. diameter x 23 in. long and of HA-188 material. The bore of the thick-walled tube was increased in diameter along the center 10 in. of length so that the rod was supported by two bearing surfaces about 1/2 in. long at the top and bottom. The diameter clearance at the bearings was about 0.010 in.

O-ring seals were used at the top between the push rod and thick-walled tube and outside the thick-walled tube near the top to seal the atmosphere cover tube (IN-600 material, 3 in. O.D. x 0.065 in. wall).

Allignment of the assembly was achieved by adjusting the four bolts which hold the unit to the bottom of the crosshead. A one-inch section of flat insulation is recommended between the unit and the crosshead. The bolts were tightened with a torque wrench to 12 ft-lb and the base plate of the unit was shimmed if necessary until a minimum friction condition was obtained when a 6 lb or less difference in load appeared between the crosshead going up and down.

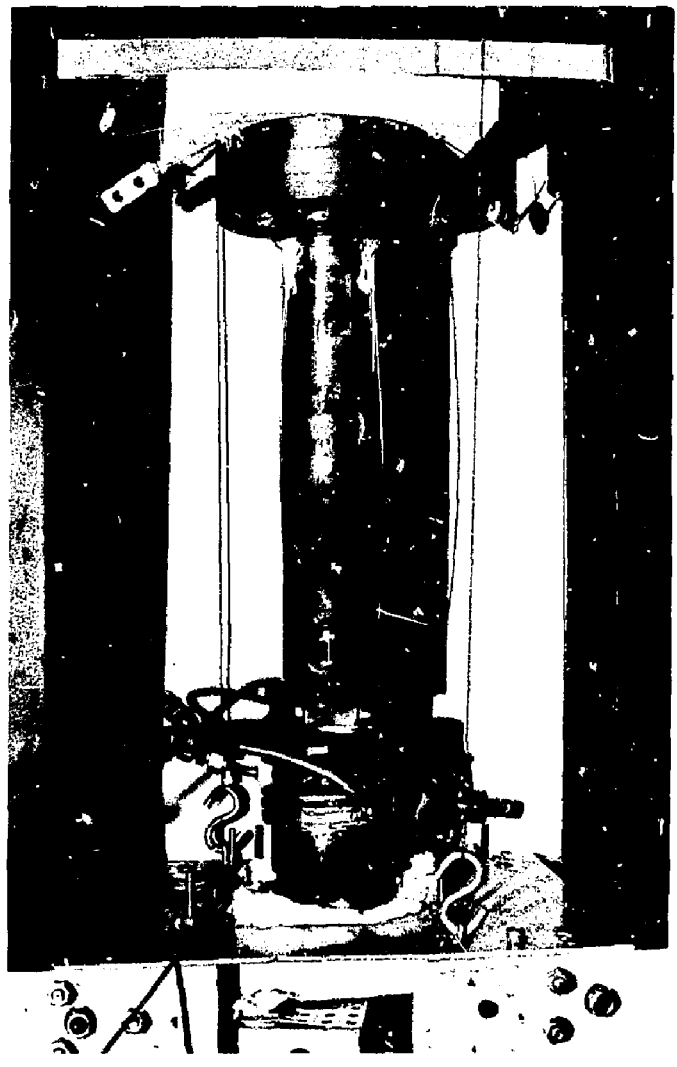

Fig. 3.1. The compression cage assembly is shown bolted to the bottom of the crosshead on an Instron machine. The specimen is inserted through the ports near the bottom and two thermocouples are used to measure temperature at both specimen-platen surfaces. The top of the atmosphere cover tube and furnace are seen below the cage.

Tungsten carbide discs were used for platens. They were approximately 5/8 in. diameter x 1/8 in. thick and ground parallel to ± 0.0001 in. with a 4 RMS microinch finish. Two chromel-alumel thermocouples touched the platens next to the specimen.

A resistance tube furnace, 3 1/2 in. I.D. x 12 in. long, was mounted on tracks on the Instron frame and counterweighted so that it could be preheated at the bottom of the Instron frame and then raised over the cage assembly. Maximum heat-up time was 2 h at 1000°C. For each test, the furnace was raised or lowered slightly to reduce the temperature difference between top and bottom of the specimen to 1°C or less.

Specimen size was 0.300 in. diameter x 0.450 in. long with a length/diameter aspect ratio of 1.5. Some transverse specimens were tested with dimensions 0.200 in. diameter x 0.300 in. long. Other specimens tested early in the program to develop the processing technique to obtain a microduplex structure were 0.250 in. diameter x 0.375 in. long.

Several lubricants were tried in the temperature range 500 - 1000°C, including graphite, MoS_2, BN powder, and Corning glass lubricant codes 8363, 7570 and 8490. In the right temperature range, the glass lubricants gave the best results with no barrelling to true strains $\varepsilon = 0.5$. However, specimens were difficult to remove from the platens and each platen required extensive grinding before reuse. The BN powder lubricant proved the most effective lubricant at all temperatures 500 - 1000°C with little barrelling at $\varepsilon = 0.4$. The flow stress difference between a sample deformed using a glass lubricant and BN lubricant could not

be detected.

In a compression specimen the measured flow stress σ_m will always be greater than the uniaxial stress σ because a finite coefficient of friction μ between the specimen ends and the platens causes a triaxial stress state in the sample. Assuming no barrelling occurs and that sliding between the specimen and platen takes place at all points except the geometric center of the cylinder, σ and σ_m are related to specimen geometry by the following equation [Schroeder and Webster (1949)]:

$$\sigma = \frac{\frac{\sigma_m}{2}\left(\frac{\mu d}{\ell}\right)^2}{\exp\left(\frac{\mu d}{\ell}\right) - \frac{\mu d}{\ell} - 1} \qquad (3\text{-}1)$$

where ℓ and d are the length and diameter of the cylinder. Eq. (3-1) reduces to $\sigma = \sigma_m$ in the limit where $\mu \to 0$. The percentage correction to σ_m to calculate σ is:

$$\text{pct correction} = \frac{\sigma_m - \sigma}{\sigma_m} \times 100 \text{ pct} \qquad (3\text{-}2)$$

Eq. (3-2) is evaluated in Table 3.1 as a function of true strain ε and the coefficient of friction for the case of an aspect ratio of 1.5, i.e., $\ell_o/d_o = 1.5$. The coefficient of friction has been determined experimentally by Cook (1957) and Uvira and Jonas (1968) to be about 0.1 for compression tests in which little or no barrelling is observed. Thus, the triaxiality correction of the measured flow stress at $\varepsilon = 0.5$ is 4.65 pct. For the compression tests in this investigation, no correction was made for the small triaxial stress state. Considering normal data scatter between specimens, it was concluded that measured flow stresses were accurate for $\varepsilon \leq 0.5$.

Tension Apparatus

The tension apparatus was difficult to design because of the con-

TABLE 3.1

CORRECTION FOR TRIAXIAL STRESS STATE*

ε \ μ	0.04	0.06	0.08	0.10	0.12	0.14	0.16	0.18
0.00	0.89	1.33	1.77	2.21	2.65	3.09	3.52	3.96
0.10	1.03	1.54	2.05	2.57	3.07	3.58	4.09	4.59
0.20	1.20	1.79	2.39	2.98	3.57	4.16	4.74	5.33
0.30	1.39	2.08	2.77	3.45	4.14	4.82	5.50	6.17
0.40	1.61	2.41	3.21	4.01	4.80	5.59	6.37	7.15
0.50	1.87	2.80	3.73	4.65	5.56	6.48	7.38	8.29
0.60	2.17	3.25	4.32	5.39	6.45	7.50	8.55	9.59
0.70	2.52	3.77	5.02	6.25	7.47	8.69	9.90	11.10
0.80	2.93	4.38	5.81	7.24	8.65	10.06	11.45	12.83
0.90	3.40	5.08	6.74	8.39	10.02	11.63	13.23	14.82
1.00	3.94	5.89	7.81	9.71	11.59	13.44	15.28	17.10

* Given as pct correction = $\frac{\sigma_m - \sigma}{\sigma_m}$ x 100 pct for the case where $\ell_o/d_o = 1.5$.

flicting requirements of oxidation control and frictionless movement of the crosshead so that low loads could be measured. The final design incorporated a stainless steel bellows whose spring constant was measurable and reproducible, Fig. 3.2. This allowed the crosshead to move about 6 in. High quality vacuum fittings were used and the final system was successfully checked by a helium leak detector sensitive to 10^{-10} atmospheric cc air per second.

Because it was felt that a threaded specimen might bond or stick to threaded grips, a buttonhead tensile specimen was designed, Fig. 3.3. The grip assembly, constructed of IN-600 and HA-188 materials, is shown in Fig. 3.4. Thermocouples coincide with the specimen shoulders at both ends of the specimen. A copper sleeve was used to smooth temperature gradients along a 6 in. length, corresponding to an initial gage length extended 600 pct.

A resistance tube furnace, 2 in. I. D. x 18 in. long, was mounted on tracks and adjusted to be exactly centered on the tensile axis. After extensive shunting of the furnace taps, specimens could be extended 500 pct with temperature along the gage length varying ± 2°C. Typical loads measured with a standard Instron load cell located outside the atmosphere tube were <20 lb.

Data Reduction

The results from the Instron tests were load-time curves at constant crosshead speed. A computer program was developed to reduce the raw data to true stress-true strain curves and calculate true strain rates at each strain. Details of the use of the program are found in Appendix A.

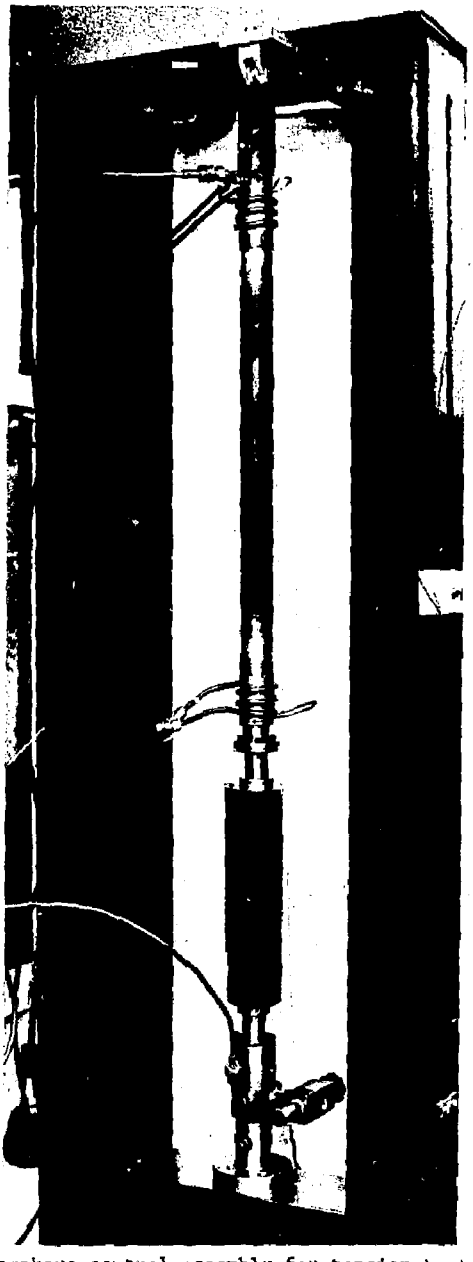

Fig. 3.2. Atmosphere control assembly for tension testing is shown mounted on Instron frame (furnace removed). High vacuum fittings are used exclusively with the stainless steel bellows providing six-inch movement of the crosshead. The plastic sleeve over the bellows prevents the bellows from bowing off axis when it is compressed. High purity argon (< 3 ppm O_2 + H_2O) enters at the bottom and exits at the top. A mechanical vacuum pump is connected to the valve at bottom to evacuate the system prior to argon flow.

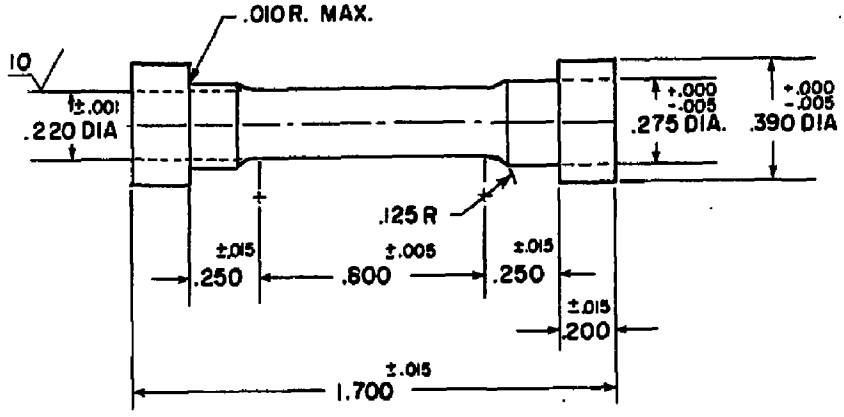

Fig. 3.3. Buttonhead tensile specimen. Dimensions are in inches.

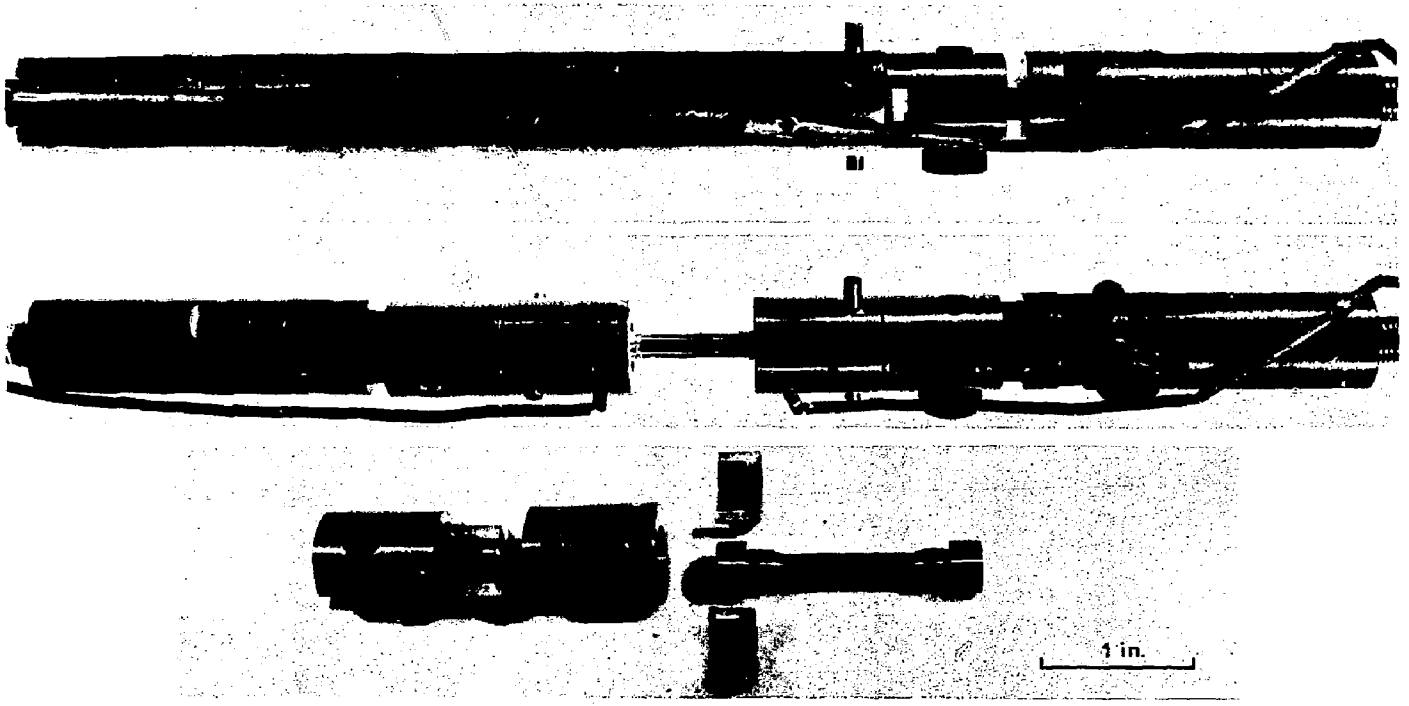

Fig. 3.4. Grip assembly for buttonhead tensile specimens. Top photo shows the actual testing configuration where a loose-fitting copper tube (6 in. long) helps smooth small temperature gradients. Grips and universal joints (center photo) are all machined from IN-600 or HA-188 superalloy material (tungsten is used for the small pins). Thermocouple holes coincide with the outer end of the shoulder near the buttonhead. Details of the specimen, split collar, grip and adapter are shown at the bottom. All photos are actual size.

The main advantage of the computer program is that it accepts points on a machine stiffness curve (e.g. in compression, a load-time curve obtained by "compressing" a platen as a dummy sample) and by interpolation, defines the exact curvilinear stiffness characteristic of the machine and apparatus. Calculated values of true plastic strain are accurate to ± 0.01 even after deformation at several different crosshead speeds on one sample. A correction to the true specimen strain rate due to the rate of contraction or elongation of the machine deflection is also calculated, but this correction is usually < 3 pct unless the load is hardening or softening at a very rapid rate (e.g. during loading or unloading a specimen in the elastic portion of the stress-strain curve).

The program accepts round or rectangular specimen cross-sections, tension or compression configurations, and any single or multiple combinations of crosshead speeds, chart speeds and full load scales. For each strain interval at constant crosshead speed, the flow stress at each point is adjusted to the median true strain rate within the strain interval using a strain rate sensitivity index $m = d \ln \sigma / d \ln \dot{\epsilon}$ inputed by the user.

Metallography

Sections of U-7.5Nb-2.5Zr were mounted in bakelite and wet-ground through no. 600 paper. After polishing on 6 and 1 μm diamond wheels with nylon cloth, a final polish was obtained using 1/20 μm Al_2O_3 in 5 pct chromic acid on microcloth. An electrolytic etch using 2 pct oxalic acid at 1-2 volts for 1-10 seconds was used.

Because the two-phase structure was so fine, electron replication micrographs were needed to resolve the structure. The polished and

etched surface was replicated with acetyl cellulose; the plastic was shadowed with chromium at 35° - 45° and backed with a carbon layer; and the plastic was dissolved in acetone, leaving the replica on a 200 mesh copper grid. A Phillips E.M. 200 electron microscope operating at 80 KV was used for examination. The magnification of most photos (5 x 5 in.) was 5000X.

Grain size was taken as the mean linear intercept of phase boundaries or grain boundaries. Volume fraction measurements used the systematic point count method [Underwood (1970 and Hilliard (1968)] with a 1 cm square grid. For an $\alpha + \gamma$ structure, such as shown in Fig. 3.5, volume fraction of the γ phase, V_γ, was calculated from $V_\gamma = P_\gamma / P_T$, where P_γ is the number of grid points in γ phase regions and P_T is the total number of points. The variance $\sigma(V_\gamma)$ was calculated from:

$$\sigma(V_\gamma) = V_\gamma \left(\frac{1 - V_\gamma}{P_\gamma}\right)^{1/2}$$

Typically, four or five micrographs like in Fig. 3.5 were needed to obtain a large enough point count so that $\sigma(V_\gamma)/V_\gamma$ was 5 pct or less.

Fiber Texture

Quantitative fiber texture measurements were made on swaged U-7.5Nb-2.5Zr rod material using a General Electric XRD-6 x-ray diffraction apparatus. The method used was adapted by McCarthy (1966) from a technique used by Lapata and Kula (1965) and described in detail by Edwards (1971). A brief description will be given here.

The rod material was spark-cut at 45° to the rod axis and electropolished for 5 min in a stirred solution of 15 ml perchloric acid, 150 ml methanol and 90 ml butylcellosolve at -20°C and 16 volts. The sample was

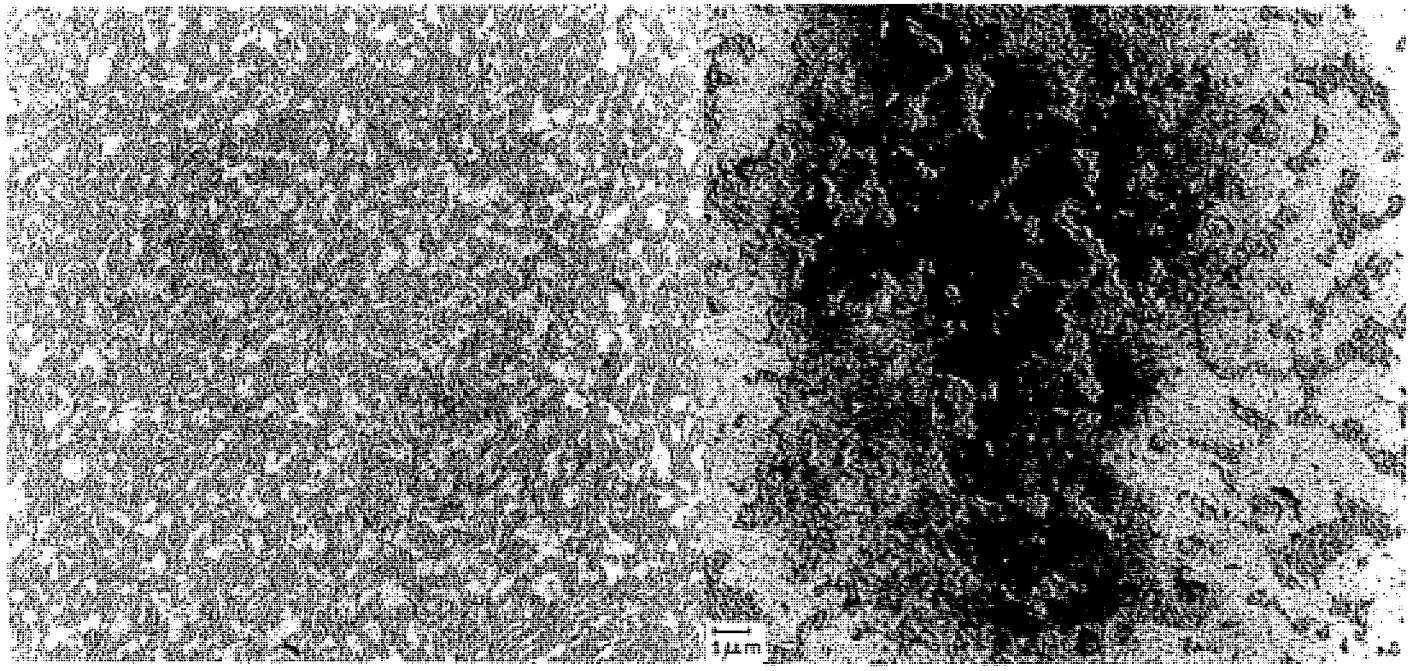

Fig. 3.5. Typical electron replica micrographs used for volume fraction analysis of the $\alpha + \gamma_1$ structure. The gamma phase is the light-colored phase with a smooth surface. The left photo shows the equilibrium structure at 500°C where $V_\gamma = 0.40$ and the right photo shows the structure at 625°C where $V_\gamma = 0.78$.

mounted on a goniometer with the cut surface inclined 45° to the diffraction plane. With the diffractometer set at the desired Bragg angle, the sample was rotated about an axis normal to the cut surface. The angle ψ of sample rotation is related to the angle ϕ between the diffraction vector and the rod axis:

$$\sin \frac{\psi}{2} = \sqrt{2} \sin \frac{\phi}{2}$$

From geometrical considerations, the number of poles of a given crystallographic plane at angle ϕ from the rod axis is proportional to $I(\phi) \sin \phi$, where $I(\phi)$ is the measured intensity minus background intensity. For a randomly textured sample, the number of poles at angle ϕ is proportional to $I_R \sin \phi$, where I_R is a constant. The total number of poles N for $\phi = 0$ to $\phi = \pi/2$ is given by

$$N = k \int_0^{\pi/2} I(\phi) \sin \phi \, d\phi,$$

where k is a proportionality constant. Equating the number of poles for the measured sample and the hypothetical random sample, we then can calculate the constant I_R:

$$I_R = \int_0^{\pi/2} I(\phi) \sin \phi \, d\phi.$$

The fiber texture can then be quantitatively described by plotting $I(\phi)/I_R$ vs. ϕ. The ratio $I(\phi)/I_R$ gives the relative number of poles of the specified crystallographic plane at angle ϕ compared to a randomly-textured sample. Because the normalizing function, $\sin \phi$, used to calculate I_R converges to zero at $\phi = 0$, this method of texture analysis provides only limited accuracy at small values of ϕ [Edwards (1971)].

CHAPTER IV

DEVELOPMENT OF A SUPERPLASTIC STRUCTURE

In this chapter the effect of thermomechanical processing techniques to produce a fine, equiaxed two-phase structure in the U-7.5Nb-2.5Zr alloy is examined. An introduction to the phase transformations in the uranium alloy is given followed by an analysis of the effect of deformation-enhanced spheroidization and quench-cold work-anneal treatments on the resultant microstructures and elevated-temperature mechanical properties. An optimum processing schedule was developed for the attainment of the finest equiaxed two-phase structure.

Results and Discussion

Phase Transformation in the U-7.5Nb-2.5Zr Alloy

The U-rich region of the U-Nb-Zr ternary diagram has been studied by Dwight and Mueller (1957) and time-temperature-transformation characteristics for the U-7.5Nb-2.5Zr alloy have been studied by Dean (1969). The ternary diagram as related to the U-7.5Nb-2.5Zr alloy is summarized in Fig. 4.1 from Dwight and Mueller (1957). Both the U-Nb and U-Zr binary systems are of the monotectoid type, and each monotectoid point (three-phase equilibrium) in the binary system becomes a line along a monotectoid valley in the ternary diagram, shown in Fig. 4.1. In the ternary system at temperatures above the monotectoid temperature (≈637°C), the single γ phase, a bcc solid solution stable at high temperatures, separates into γ_1 (U-rich) and γ_2 (Zr-rich) at the U-Zr monotectoid system and γ_1 (U-rich) and γ_3 (Nb-rich) at the U-Nb monotectoid system. For the U-7.5Nb-2.5Zr alloy the γ_2 phase is never present because the U-Zr monotectoid system is eliminated with the addition of $\geq$ 0.8 wt. pct Nb [Dwight and Mueller (1957)]. Also eliminated in the β phase (nearly

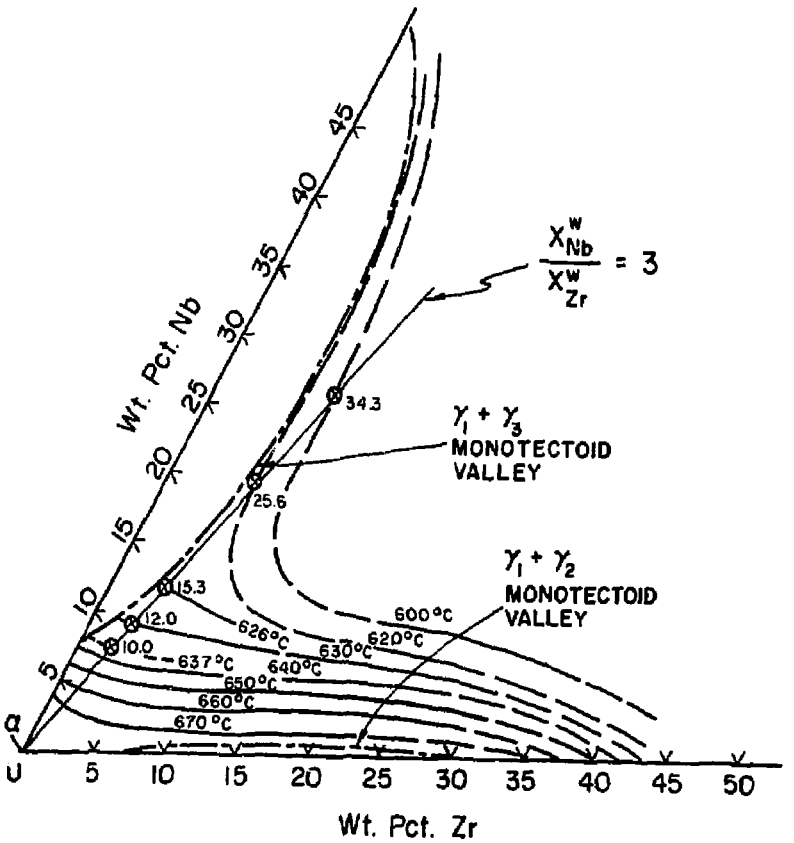

Fig. 4.1. A ternary diagram [Dwight and Mueller (1957)] shows projections of monotectoid valleys and isothermal lines. The intersection of the line for the weight fraction ratio $X^w_{Nb}/X^w_{Zr} = 3$ with an isothermal line determines the composition of the γ_1 phase in the two phase region $\alpha + \gamma_1$. At the circled data points, wt. pct Nb + Zr is given. Since the line from the U corner tangent to the projection of the monotectoid valley is $X^w_{Nb}/X^w_{Zr} = 3.3$, the diagram predicts a three phase region $\alpha + \gamma_1 + \gamma_3$ only for alloy compositions where $X^w_{Nb}/X^w_{Zr} > 3.3$.

pure β-U) with the addition of $\geq$ 4 wt. pct Nb [Dwight and Mueller (1957)]. The $\gamma_1 + \gamma_3$ monotectoid valley reaches a critical point at ≈622°C, below which temperature the $\gamma_1 + \gamma_3$ miscibility gap is closed.

According to Fig. 4.1 the U-7.5Nb-2.5Zr alloy composition is near-monotectoid composition and lies just outside the $\gamma_1 + \gamma_3$ monotectoid valley. Since the solubility of Nb or Zr in the α phase is < 0.5 wt. pct for either element [Elliott (1965) and Shunk (1969)], the composition of the gamma phase in the two-phase region $\alpha + \gamma_1$ can be determined by constructing a tie-line from the U corner of the diagram (α phase) through the U-7.5Nb-2.5Zr alloy composition point. Some γ_1 phase compositions at different temperatures from 600 - 637°C are circled in Fig. 4.1 with wt. pct Nb + Zr given at each point.

It is our convention to write the transformation as $\gamma \rightarrow \alpha + \gamma_1$ for the U-7.5Nb-2.5Zr alloy. In the two-phase region the gamma phase is termed "γ_1" because the composition is closer to the U-rich end of the $\gamma_1 + \gamma_3$ monotectoid valley. Dwight and Mueller (1957) used the terms "$\gamma_{1,3}$" or "γ" below the $\gamma_1 + \gamma_3$ critical point (≈622°C) and Dean (1969) used "γ_3". In our notation, the symbol "γ" is retained for the single-phase region. Thus, in this investigation, the γ phase has the composition U-7.5Nb-2.5Zr.

It can be seen in Fig. 4.1 that the $\alpha + \gamma_1$ tie-line does not intersect the $\gamma_1 + \gamma_3$ monotectoid valley; therefore, a three phase region $\alpha + \gamma_1 + \gamma_3$, such as shown in Fig. 4.2, is not predicted for the U-7.5Nb-2.5Zr alloy. The high temperature phases in the U-7.5Nb-2.5Zr alloy can be summarized simply by one phase transformation, $\gamma \rightarrow \alpha + \gamma_1$ at 637°C. The features of the U-Nb-Zr ternary diagram below 637°C relevant to

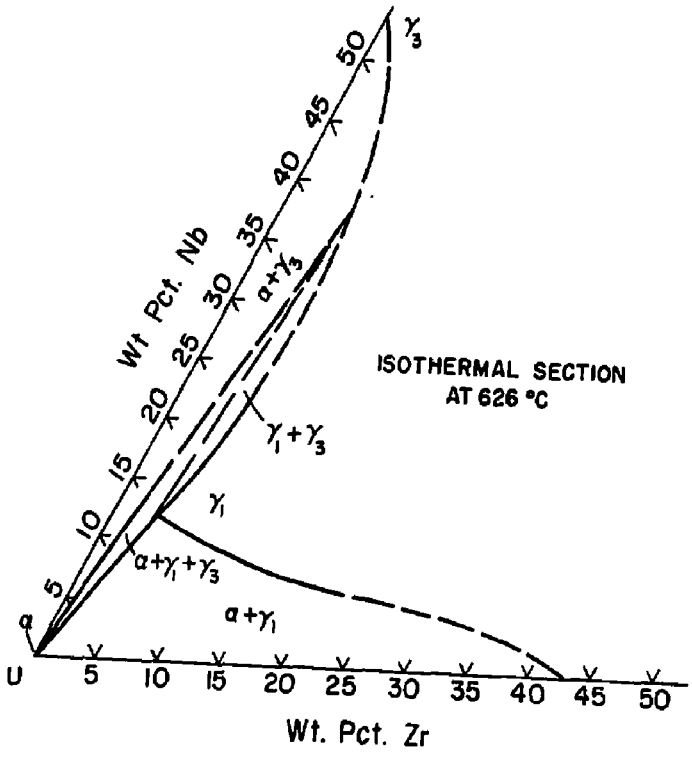

Fig. 4.2. A typical isothermal section showing a three-phase region $\alpha + \gamma_1 + \gamma_3$ [Dwight and Mueller (1957)].

the U-7.5Nb-2.5Zr alloy are a line separating the $\alpha + \gamma_1$ and γ regions and a line at the U corner separating the α and $\alpha + \gamma_1$ regions. An example is shown in Fig. 4.3 for the 621°C isotherm. The α phase is nearly pure α-U with a base-centered orthorhombic crystal structure and the γ_1 phase is a Nb-rich bcc solid solution with a composition which is strongly temperature-dependent. Dwight and Mueller (1957) did not investigate regions of the ternary diagram which would describe γ_1 phase compositions for the U-7.5Nb-2.5Zr alloy at temperatures below 600°C.

A time-temperature-transformation diagram from Dean (1969) is shown in Fig. 4.4. From 400 - 637°C a normal "C" curve describes the $\gamma \rightarrow \alpha + \gamma_1$ transformation kinetics. During isothermal transformation, the product has a lamellar morphology, Fig. 4.5. To insure complete transformation we found that 120 h were necessary at 608°C and 24 h were necessary at 550°C.

Some additional low-temperature metastable phases are also shown in Fig. 4.4. The γ^s phase is the high temperature γ phase retained at room temperature by rapid water quenching. Yakel (1969) reported the γ^s phase to be bcc with the body-centered atoms shifted slightly in correlated <100> directions. The γ^o phase, with a tetragonal crystal structure, is produced by ageing the γ^s phase. Two transition alpha phases are observed [Dean (1969)]: α' has a tetragonal structure and α'' has a monoclinic structure. These metastable structures are not important in our investigation, except in relation to special heat treatments. Our objective is to study the mechanical properties in the $\alpha + \gamma_1$ region, stable at elevated temperature.

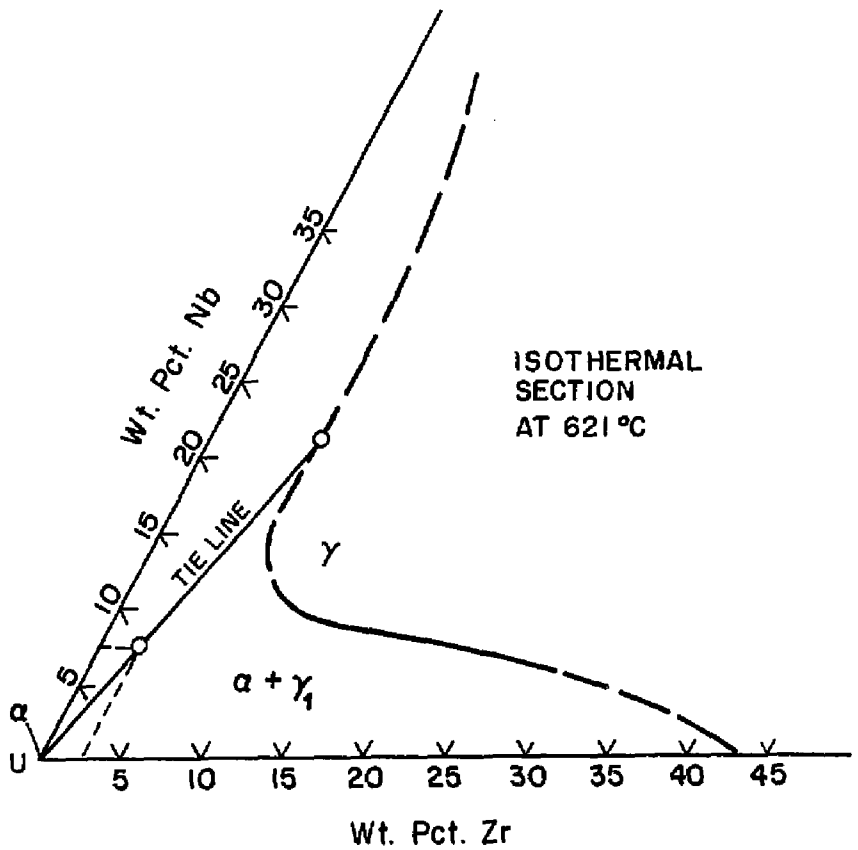

Fig. 4.3. The ternary diagram below the critical temperature (~622°C) does not contain a three-phase region [Dwight and Mueller (1957)]. The composition of the γ_1 phase is determined by the tie line extending from the U corner (α phase) through the alloy composition point (U-7.5Nb-2.5Zr).

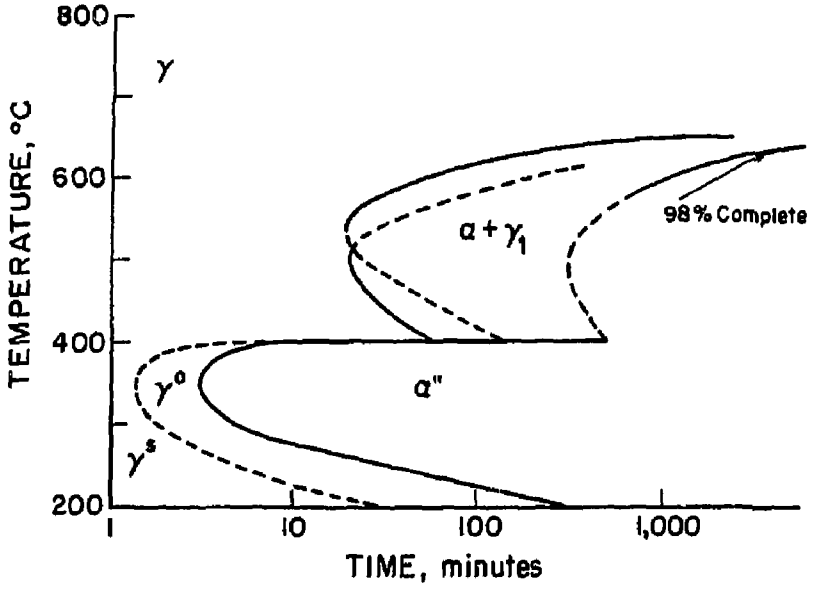

Fig. 4.4. Time-temperature-transformation diagram for U-7.5Nb-2.5Zr as determined by Dean (1969).

Methods Used by Other Investigators

Fine-grain equiaxed microstructures are commonly produced in eutectic and eutectoid systems by heavily hot working in the two-phase field [see the review papers of Johnson (1970) and Davies et al. (1970)]. During hot working at temperatures $\geq 0.5T_m$ the lamellar structure is spheroidized into fine equiaxed phase regions. Typically, the working temperature is reduced if coarsening of the microstructure occurs, but few details of the mechanism of structural refinement are reported. The effect of deformation on the enhancement of the spheroidization of lamellar structures will be considered in the next section.

Other methods reported for preparing superplastic microstructures are packrolling [Avery and Backofen (1965)], electroplating [Martin and Backofen (1967)], extruding alloy powders [Freche et al. (1970), Reichman et al. (1970) and Watts and Stowell (1971)], splat cooling [Beghi et al. (1970)], and special heat treatments. The heat treatment procedures include a simple water quench from the single-phase field for the Zn-Al eutectoid alloy, alternate rapid austenitize-quench cycles for commercial steels [Schadler (1968)], and a quench-cold work-anneal treatment for Cu-Ni-Zn alloys [Ansuini and Badia (1973)]. Our approach for the U-7.5Nb-2.5Zr alloy was to first study deformation-enhanced spheroidization and later explore possible special thermal-mechanical treatment methods.

Review of Deformation-enhanced Spheroidization Studies

The mechanism of deformation-enhanced spheroidization has been studied extensively for steels, but only reported as the method used to obtain microduplex structures in many superplastic alloys. One other relevant observation was made by Butcher et al. (1969) who reported

spheroidization due to deformation in a unidirectionally-grown Al-$CuAl_2$ eutectic at a temperature where the structure is normally thermally stable.

Deformation-enhanced spheroidization of pearlite has been reported by Robbins et al. (1964), Irani and Taylor (1968), Chojnowski and Tegart (1968), Sherby et al. (1969), Harrigan and Sherby (1971), and Paqueton and Pineau (1971). Transmission electron micrographs revealed a fine ferritic subgrain structure produced during deformation [Irani and Taylor (1968), Paqueton and Pineau (1971), and Bly et al. (1973a)]. The dislocation substructure provides greatly increased numbers of grain boundary diffusion paths to accelerate the spheroidization. Harrigan and Sherby (1971) determined that grain boundary diffusion of iron atoms was the rate controlling process for both static and dynamic spheroidization. At high strain rates, where $\dot{\varepsilon}/D > 10^9$ cm^{-2} with D being the lattice diffusion coefficient for iron atoms, excess vacancies generated during deformation would be expected to further enhance the spheroidization rate [Armstrong et al. (1973a)].

Another mechanism which could account for high diffusion coefficients is strain-enhanced diffusion due to moving dislocations. Cohen (1970) empirically expressed the enhancement as

$$D'/D_L = 1 + \dot{\varepsilon} \times 6 \times 10^{-3} \exp(11.3\ T_m/T) \qquad (4\text{-}1)$$

where D' is the strain-enhanced diffusion coefficient, D_L is the lattice self-diffusion coefficient, $\dot{\varepsilon}$ is strain rate (1/s) and T_m is the absolute melting temperature. Harrigan and Sherby (1971) found that strain-enhanced diffusion coefficients predicted a greater spheroidization enhancement than that observed at $\dot{\varepsilon} = 3 \times 10^{-4}/s$ and T = 700°C. Using

Eq. (4-1), a calculation at $\dot{\varepsilon} = 1/s$ and $T = 0.5T_m$ (632°C for Fe), typical values used in the production of very fine spheroidized microstructures [Sherby et al. (1969) and Bly et al. (1973a)], predicts the enhancement to be 10^8, which is unrealistically high. It should be noted that the experimental data used by Cohen (1970) gave a maximum enhancement of 10^3, so considerable extrapolation was needed for our calculation.

Better agreement with experiment at low strain rates was obtained by Harrigan and Sherby using the Hart (1957) equation in the form

$$D_{eff} = D_L f_L + D_B f_B$$

where the effective diffusion coefficient D_{eff} is determined from the relative contribution of lattice and boundary diffusion weighted by the atom fraction for each mechanism. The fraction f_B was calculated from subgrain size, assuming boundary width to be 5 Å. The relative agreement of calculated diffusion enhancements D_{eff}/D_L and observed spheroidization enhancements indicate that subgrain structure is important in the rapid spheroidization process.

Paqueton and Pineau (1971) observed that spheroidization takes place preferentially at ferrite subgrain boundary intersections with cementite lamellae. Also, dislocations or subgrain boundaries were observed in the cementite phase and these locations were associated with rapid morphological changes. Baranov (1969) also observed spheroidization beginning at intersections of ferrite subboundaries and cementite lamellae. These observations are direct evidence that diffusion along subboundaries enhances the spheroidization rate. In contrast, static spheroidization begins at growth faults or lamellae tips [Baranov (1969)].

Deformation-enhanced Spheroidization in U-7.5Nb-2.5Zr

The initial investigation of deformation-enhanced spheroidization in the U-7.5Nb-2.5Zr alloy consisted of a series of compression tests in which the lamellar structure, Fig. 4.5, was deformed at 475 - 625°C and $\dot{\varepsilon} = 3 \times 10^{-4}$/s to $\dot{\varepsilon} = 3 \times 10^{-2}$/s. Specimens were deformed to a true strain $\varepsilon = 1.0$ and the strain rates are average values for this strain interval for the constant crosshead speed tests. The stress-strain curves are shown in Fig. 4.6 for the coarse lamellar structure (~0.5 μm interlamellar spacing). In all curves the flow stress decreases with strain to about $\varepsilon = 0.6$, although softening probably continues at larger strains but is masked by significant barrelling of the specimens and a large triaxial stress state. The greatest relative decrease in the flow stress occurs at the highest temperature (625°C) and lowest strain rate (3×10^{-4}/s), where at $\varepsilon = 0.6$ the flow stress has softened by a factor of one-third.

Photomicrographs show that the reduction in the flow stress is accompanied by spheroidization of lamellae and coalescence or growth into larger globular regions. Morphological changes occurring during deformation of the fine pearlitic structure (~0.1 μm interlamellar spacing) for the conditions of maximum observed strain softening (625°C and $\dot{\varepsilon} = 3 \times 10^{-4}$/s, Fig. 4.7) are seen in Fig. 4.8. At $\varepsilon = 0.95$ the equiaxed regions are about 80 pct of the total. Under the same deformation conditions the coarse lamellar structure had a smaller fraction of spheroidized regions and the equiaxed regions were coarser, Fig. 4.9. This observation is consistent with the greater diffusion distances in the coarse lamellar structure compared to the fine lamellar structure.

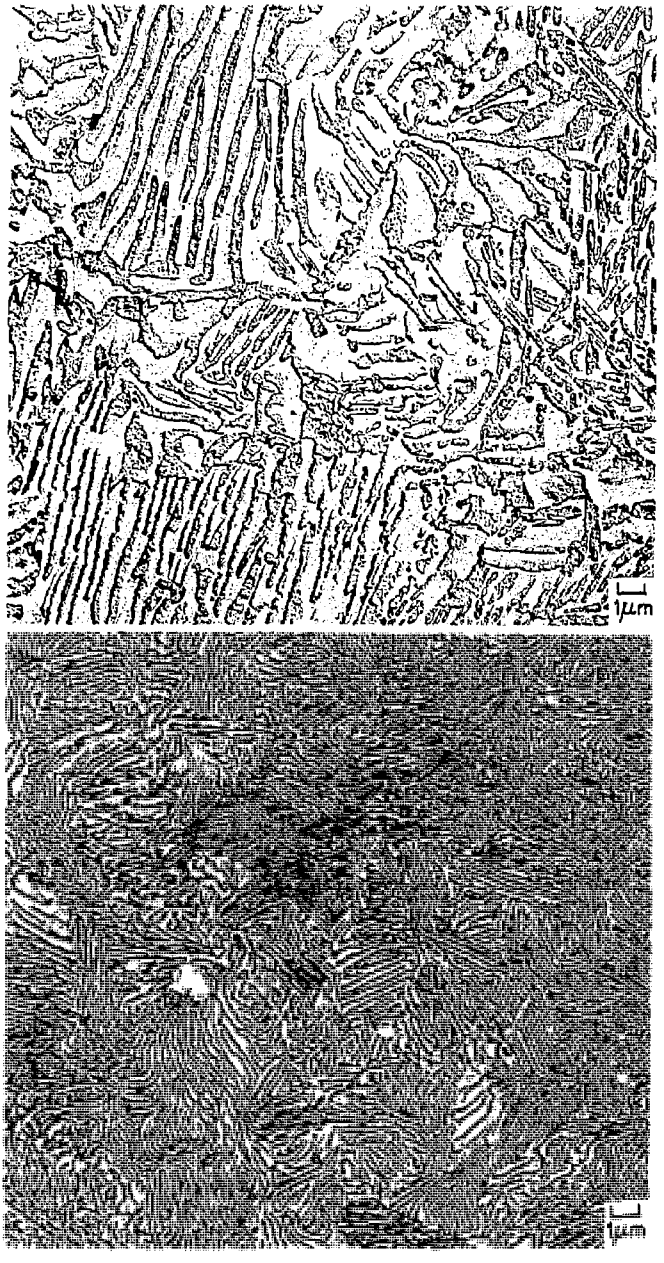

Fig. 4.5. Lamellar structures formed by isothermal transformation. The dark phase (with a rough surface is the α phase. The coarse structure (top, ≈0.5 μm interlamellar spacing) was obtained after annealing at 608°C for 120 h and the fine structure (bottom, ≈0.1 μm interlamellar spacing) was obtained after 8 h at 550°C.

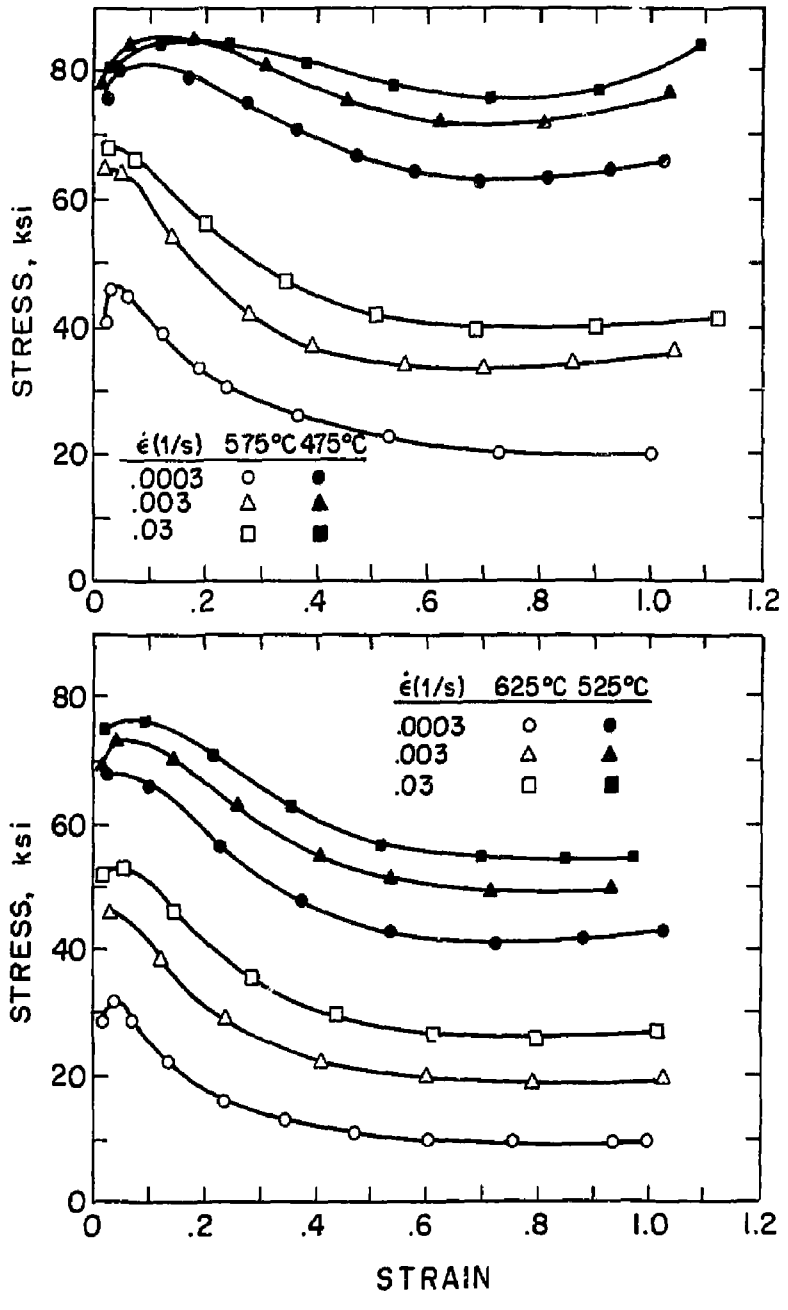

Fig. 4.6. Compression stress-strain curves for the coarse lamellar structure. Strain softening is associated with spheroidization.

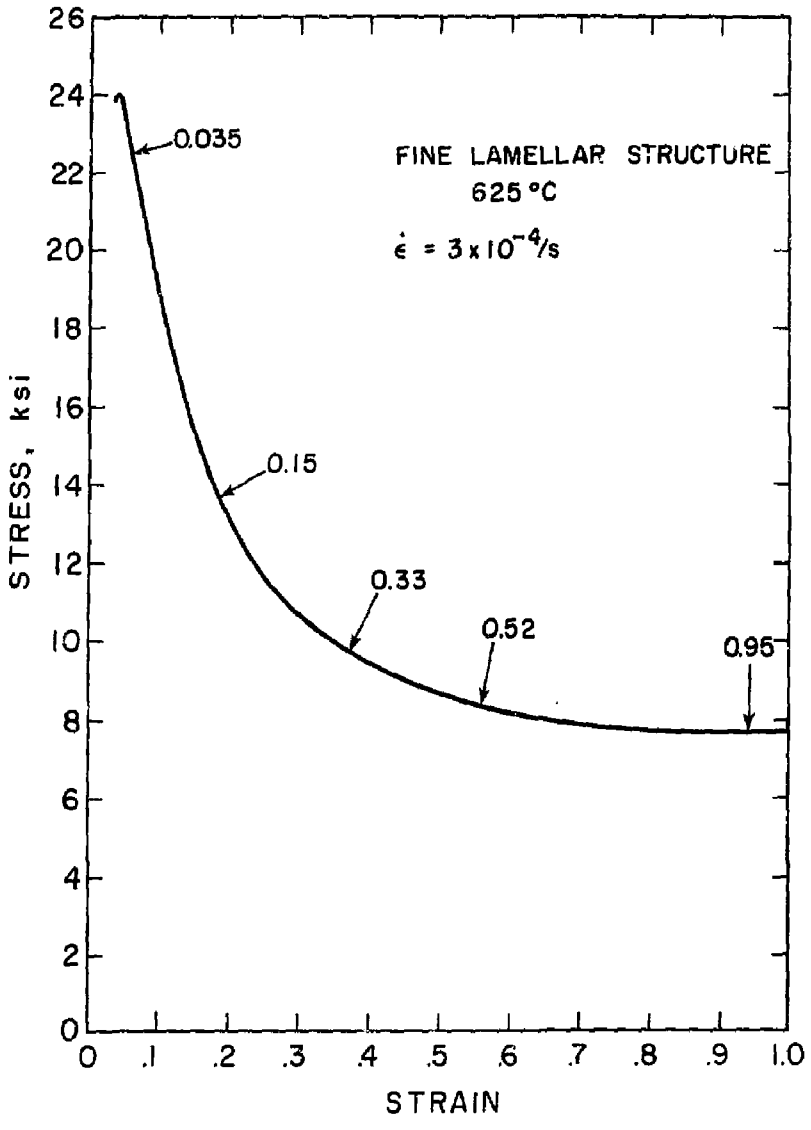

Fig. 4.7. Compression stress-strain curve for the fine lamellar structure tested at 625°C and $\dot{\varepsilon}$ = 3 x 10^{-4}/s. The arrows indicate the strain at which deformation on five different specimens was terminated. Microstructures of these specimens are shown in Fig. 4.8.

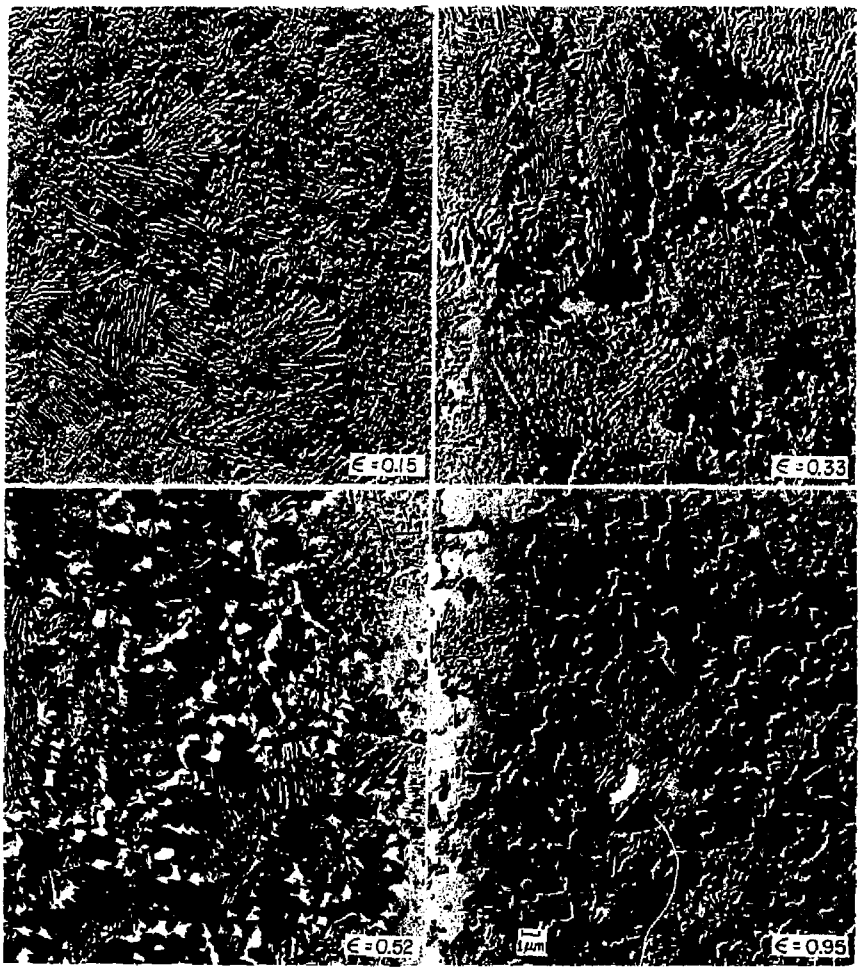

Fig. 4.8. Microstructures after deformation of the fine lamellar structure at 625°C and $\dot{\varepsilon} = 3 \times 10^{-4}$/s to strains indicated. Spheroidization increases with strain from <10 pct spheroidized at $\varepsilon = 0.15$ to about 80 pct spheroidized at $\varepsilon = 0.95$.

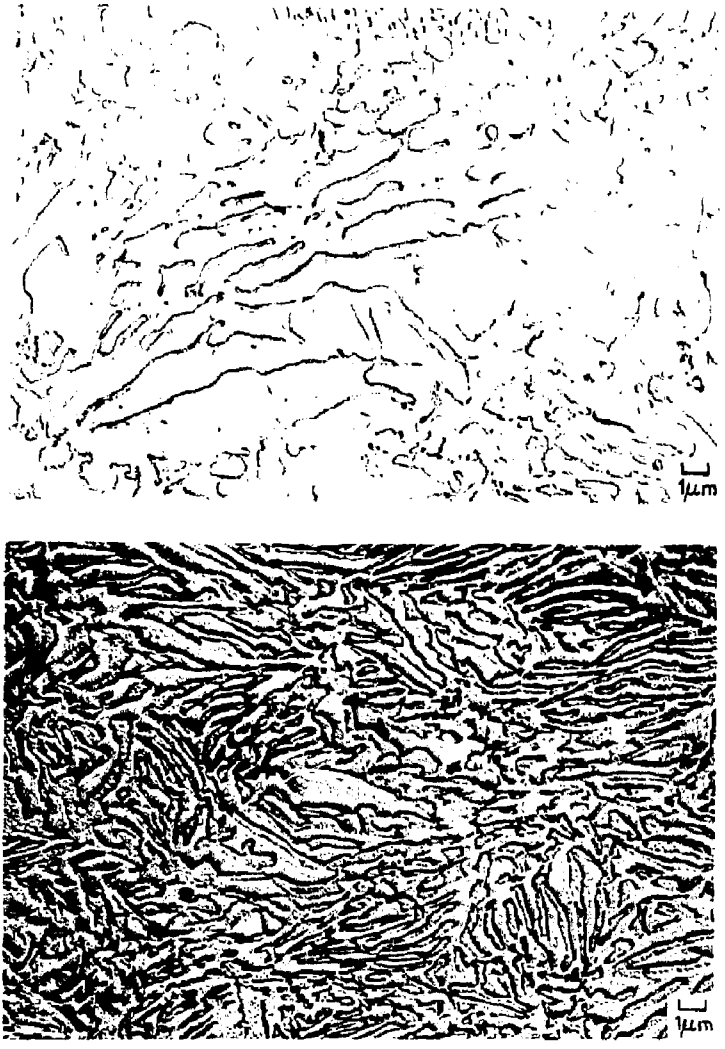

Fig. 4.9. Microstructures after deformation of the coarse lamellar structure to $\varepsilon = 1.0$ for the conditions: 625°C and $\dot{\varepsilon} = 3 \times 10^{-4}$/s, top photo; and 475°C and $\dot{\varepsilon} = 0.03$/s, bottom photo.

Similar results were observed by Paqueton and Pineau (1971) for steels. Also shown in Fig. 4.9 is a micrograph after deformation of the coarse lamellar structure at the lowest temperature (475°C) and highest strain rate (3×10^{-2}/s), conditions corresponding to the smallest observed strain softening. There is some spheroidization near plate edges, but the structure is primarily lamellar. Spheroidization in Figs. 4.8 and 4.9 is totally a result of enhancement by concurrent straining. Both coarse and fine lamellar structures statically annealed at 625°C for 90 min, equivalent to the time at temperature for specimens deformed at $\dot{\varepsilon} = 3 \times 10^{-4}$/s to $\varepsilon = 1.0$, showed no signs of spheroidization.

Some minor effects on spheroidization were observed for different treatments used to obtain the initial lamellar structure at 550°C. Most specimens were up-quenched from the room temperature gamma-quenched state for the annealing treatment; however, specimens down-quenched from 700°C to 550°C were about 10 pct weaker during deformation at 625°C and $\dot{\varepsilon} = 3 \times 10^{-4}$/s than up-quenched specimens, Fig. 4.10. It is believed that partial precipitation of metastable phases during the initial gamma-quenching or during the heat-up to the annealing temperature slightly affected the transformed lamellar structure. Fig. 4.10 also shows that a 24 h anneal at 550°C leads to more rapid softening during deformation than an 8 h anneal. The 8 h anneal probably does not insure 100 pct transformation. In another treatment, a specimen was held at 350°C for 15 min before annealing at 550°C for 8 h. According to Dean's (1969) time-temperature-transformation diagram, Fig. 4.3, precipitation of metastable phases at 350°C should be complete in 15 min; however, no difference in structure or stress-strain curves at 625°C and $\dot{\varepsilon} = 3 \times 10^{-4}$/s

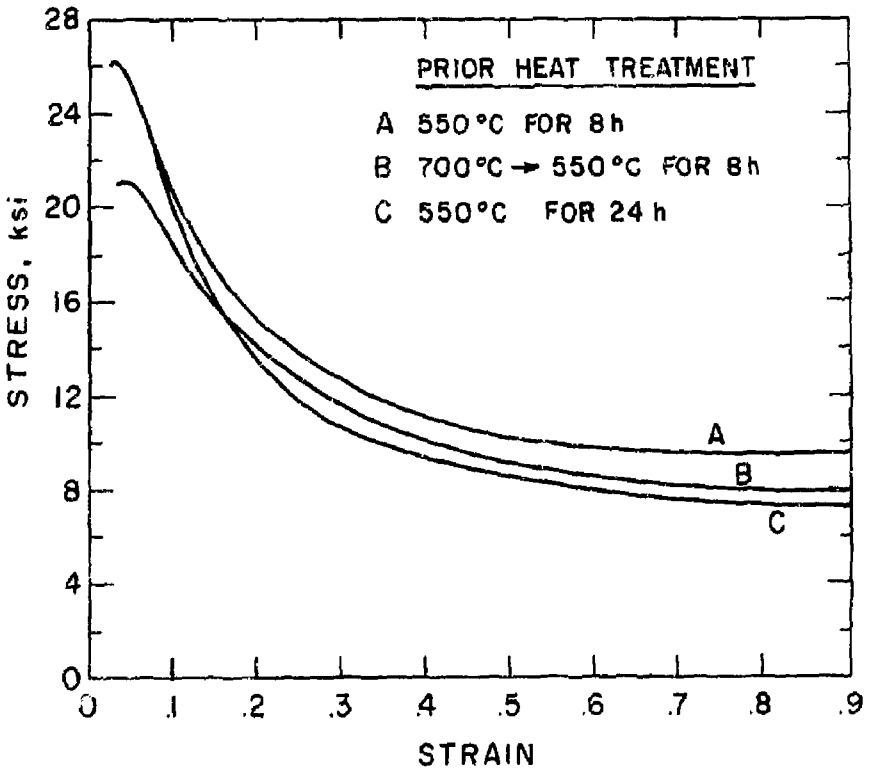

Fig. 4.10. Effect of minor heat treatment variables on the stress-strain curve at 625°C and $\dot{\epsilon} = 3 \times 10^{-3}/s$ for the fine lamellar structure.

were detected compared to specimens normally annealed at 550°C for 8 h.

Activation energies for deformation during spheroidization of the coarse lamellar structure were calculated from stress-strain data at 575 and 625°C, assuming the relation

$$\dot{\varepsilon} = A \exp(-Q/RT) \ (\sigma/E)^n \qquad (4\text{-}2)$$

In Eq. (4-2), Q is the creep activation energy, E is the elastic modulus and A is a constant. Values of Q were calculated at constant σ/E using data at $\varepsilon \cong 0.03$ (maximum stress) and at $\varepsilon = 0.6$ (after strain softening), Fig. 4.11 [modulus data were taken from Bugrov et al. (1972); see Fig. 5.6, Chapter V]. The activation energy for data at $\varepsilon \cong 0.03$ and $\varepsilon = 0.6$ were found to be 58 kcal/mole and 62 kcal/mole, respectively. The apparent activation energies for grain boundary and lattice diffusion were estimated in Chapter V as 72 kcal/mole and 130 kcal/mole, respectively. Thus, spheroidization probably occurs by diffusion along grain or subgrain boundaries rather than by lattice diffusion. Activation energies calculated using data at 475 and 525°C were considered inaccurate due to the large slope of the log $\dot{\varepsilon}$ vs. log σ curve (large n value in Eq. 4-1) and data scatter.

Deformation-enhanced spheroidization was also investigated at high strain rates with rolling experiments. A plate with a coarse lamellar structure was rolled at 620°C at $\varepsilon \cong 0.25$ per pass to a true strain $\varepsilon = 1.92$. The rolling was performed at Lawrence Livermore Laboratory in March 1970 with the assistance of N. R. Borch. The uranium alloy was jacketted in copper for oxidation protection and the plate was reheated to 620°C before each pass. The rolls were heated to 315°C. The average strain rate was about 20/s, calculated by the method given by Dieter (1961) for 6 in. diameter rolls operated at 11 rpm. The structure after rolling

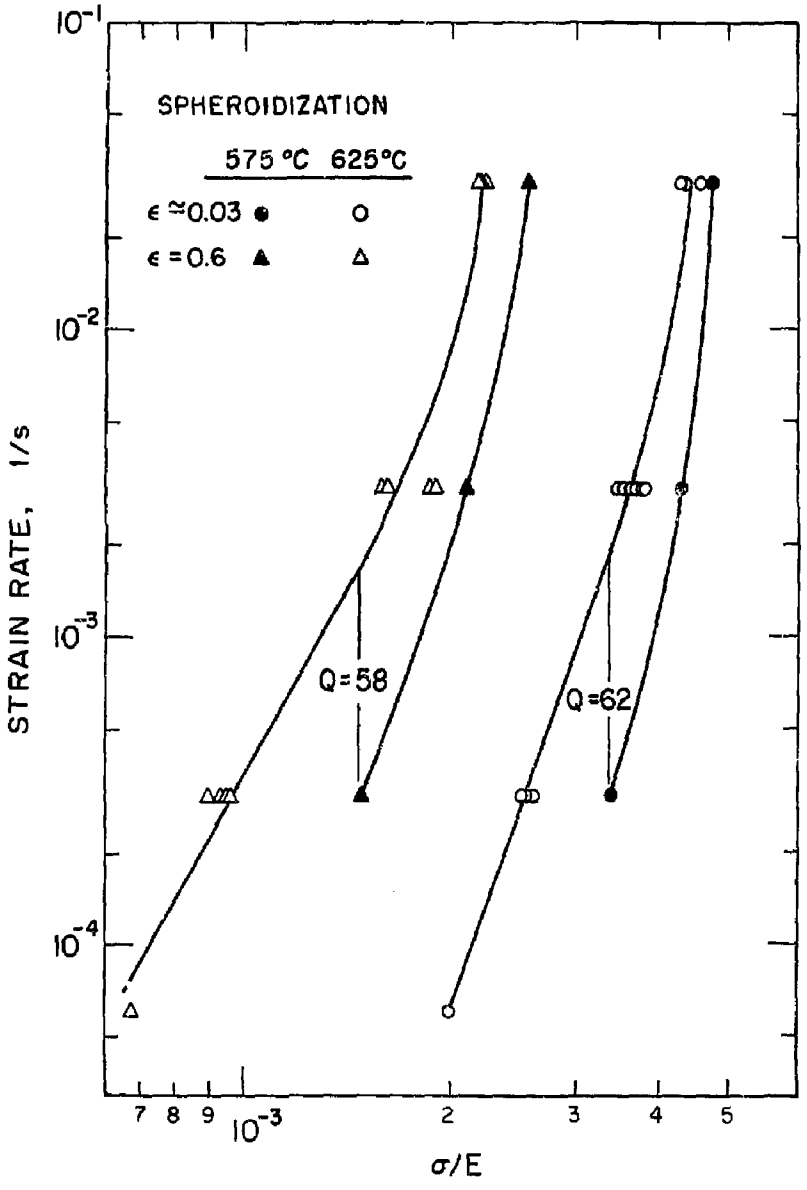

Fig. 4.11. Activation energies (in kcal/mole) calculated between 575 and 625°C for deformation during spheroidization are shown on a log $\dot{\varepsilon}$ vs. log σ/E diagram. The data points are for a coarse lamellar structure deformed to strains $\varepsilon \cong 0.03$ (maximum stress) and $\varepsilon = 0.6$.

was not completely spheroidized, but the spheroidized regions showed a finer spheroidite size than for the coarse lamellar structure deformed at 625°C and $\dot{\varepsilon} = 3 \times 10^{-4}$/s, Figs. 4.12 and 4.13. This observation is consistent with results for Fe-C [Chojnowski and Tegart (1968), Sherby et al. (1969), Harrigan and Sherby (1971) and Paqueton and Pineau (1971)] in which deformation at a high strain rate and/or a low temperature (a high flow stress condition) produces large numbers of dislocation short circuit diffusion paths associated with a fine subgrain size and a resultant fine spheroidized structure. In contrast, a coarse spheroidite size is produced during deformation at a high temperature and/or a low strain rate (a low flow stress condition) where the dislocation cell size is large.

The primary difference between deformation-enhanced spheroidization in the U-7.5Nb-2.5Zr alloy and in the Fe-C system is that the rate of spheroidization in the uranium alloy is much slower than in steels. For example, at $0.54T_m$ (625°C for U-7.5Nb-2.5Zr and 707°C for Fe-C), spheroidization in Fe-C is complete at $\varepsilon = 1.0$ for deformation rates 3×10^{-4} to 3×10^{-2}/s [Harrigan and Sherby (1971)]. Complete spheroidization was not achieved in the U-7.5Nb-2.5Zr alloy, even after deforming to $\varepsilon = 1.92$ and $\dot{\varepsilon} \cong 20$/s. This difference in spheroidization rates may be due to a difference in grain boundary diffusion coefficients for the two alloys at the same homologous temperature. In the grain boundary diffusion data correlation in Chapter II,

$$D_B = 1 \exp (-11T_m/T) \text{ cm}^2/\text{s}, \qquad (4\text{-}3)$$

the actual range of data at $0.54T_m$ is about plus or minus one order of magnitude from the best-fit line. Since the grain boundary

Fig. 4.12. Microstructures obtained by deforming the coarse lamellar structure at 625°C: (1) at $\dot{\epsilon} = 3 \times 10^{-4}/s$ to $\epsilon = 1.0$, top, and (2) at $\dot{\epsilon} \cong 20/s$ during rolling to $\epsilon = 1.92$, bottom. Within regions which have spheroidized, a finer structure is obtained after deformation at a high strain rate (high flow stress condition).

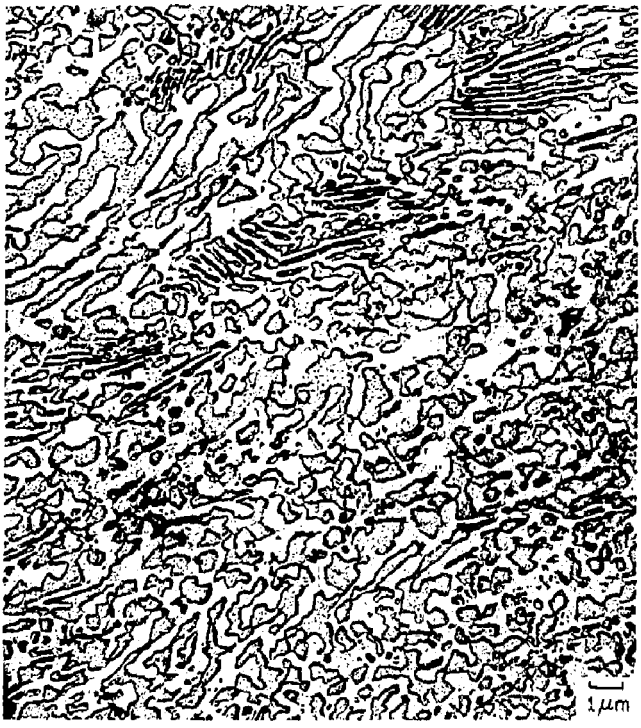

Fig. 4.13. Detail of a spheroidized region obtained after rolling the coarse lamellar structure at 620°C to $\varepsilon = 1.92$. This spheroidite size is finer than that obtained after deformation at a low strain rate at 625°C (see Fig. 4.9, top photograph).

diffusion coefficient for α-Fe at $0.54T_m$ is about one order of magnitude greater than the correlation predicts, it is quite possible that the grain boundary diffusion coefficient for the γ_1 phase in the U-7.5Nb-2.5Zr alloy is less than that in α-Fe. A difference in the surface energy of the phase boundaries could lead to a difference in spheroidization rates in the two systems, since the driving force for spheroidization is a reduction in interfacial energy.

The difference in spheroidization rates in the uranium alloy and steels is probably not due to a difference in the number of high diffusivity paths available. Subgrain size λ is usually inversely related to the stress [Sherby and Young (1972)],

$$\lambda = 4\ b\left(\frac{\sigma}{E}\right)^{-1}$$

where b is Burgers vector. Dislocation density ρ is related to stress by [Bird et al. (1969)]:

$$\sigma/E = \alpha\ b\sqrt{\rho}$$

where α is a constant about equal to 0.6. If the high diffusivity paths are along dislocations or subgrain boundaries, σ/E is a measure of the relative number of enhanced diffusion paths present during deformation. Comparing σ/E values for U-7.5Nb-2.5Zr (fine lamellar structure) and Fe-C [Harrigan and Sherby (1971)] at $0.54T_m$, $\dot{\varepsilon} = 3 \times 10^{-4}$/s and $\varepsilon = 0.6$, we find values of 7×10^{-4} and 4×10^{-4}, respectively. Thus the number of possible high diffusivity paths is not expected to be less for the U-7.5Nb-2.5Zr alloy than for Fe-C.

The lack of spheroidization at the lowest temperature, 475°C, can be explained qualitatively by noting that because the equilibrium composition of the γ_1 phase changes with temperature (causing the melting temperature of the γ_1 phase to vary with test temperature), the homologous

temperature decreases rapidly with temperature from $0.54T_m$ at 625°C to $0.39T_m$ at 475°C (see Fig. 5.18, Chapter V). Thus, from Eq. (4-3), the grain boundary diffusion coefficient also decreases rapidly with decreasing temperature. Even though the number of high diffusivity dislocation or subgrain boundary diffusion paths is large at the high stress condition at 475°C, the diffusion coefficient is evidently not great enough to produce high spheroidization rates.

Effect of Cold Work before the Phase Transformation

Deforming the lamellar structure at 475 - 625°C did not prove to be a very efficient method to produce a fine equiaxed microstructure in the U-7.5Nb-2.5Zr alloy. The spheroidization rate was too slow with incomplete spheroidization resulting even after deformation at 620°C and $\dot{\varepsilon} \cong 20/s$ to $\varepsilon = 1.92$. A quench-coldwork-anneal treatment was then conducted to try to produce a spheroidized structure with a minimum of deformation strain. Since the γ phase can be retained at room temperature by water quenching, cold work could alter the transformation product formed during annealing at 400 - 637°C.

Fig. 4.14 shows the structure produced after gamma-quenching, room temperature deformation to $\varepsilon = 0.283$, and annealing at 550°C for 24 h. The deformation was introduced by compression of a standard specimen cylinder at a strain rate of $3 \times 10^{-3}/s$ on an Instron machine, using teflon tape as a lubricant. The structure is partially spheroidized with little evidence of long lamellae. Concurrent precipitation and recrystallization could account for this microstructure as discussed by Ansuini and Badia (1973) for Cu-Ni-Zn alloys. However, if recrystallization occurred before precipitation, the effect of cold work would be lost. Another possibility is that the nucleation rate of the α phase is in-

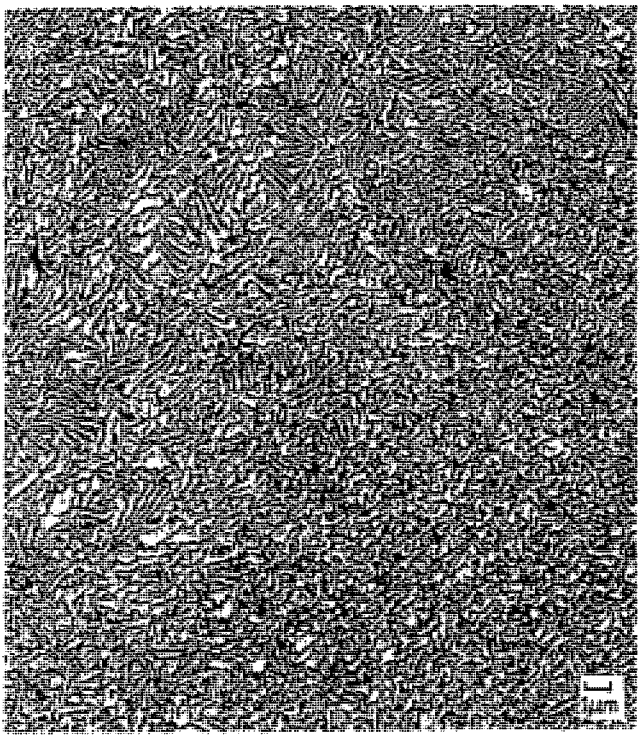

Fig. 4.14. Microstructure obtained after gamma-quenching, deforming at room temperature to $\varepsilon = 0.283$, and annealing at 550°C for 24 h.

creased by the introduction of many new favorable nucleation sites at dislocation tangles. The transformation product could then consist of very short platelets which would be readily spheroidized during annealing or hot working. A third possibility is that α or metastable α phases are nucleated as a fine precipitate distribution during cold working, which upon annealing forms a fine spheroidized structure. This process is unlikely, however, because samples aged at 350°C to form an α" precipitate (monoclinic crystal structure) transformed to a lamellar structure during annealing at 550°C. A structure with precipitates formed during cold working would also be expected to transform at 550°C to a lamellar structure.

The effect of the amount of cold work before annealing in shown in Fig. 4.15, after deformation at 625°C and $\dot{\varepsilon} = 4 \times 10^{-4}$/s to $\varepsilon \cong 0.7$. Cold deformation to $\varepsilon = 0.4$ is sufficient for complete spheroidization under these conditions.

Optimum Processing

Using the optimum parameters defined by laboratory heat treatments and compression and rolling tests, the U-7.5Nb-2.5Zr alloy was prepared from raw materials and processed to a fine-grain equiaxed microstructure using swaging operations at the Albany Metallurgy Research Center, U.S. Bureau of Mines, Albany, Oregon. The processing was directed by L. E. Armantrout and completed in August 1971. The basic processing steps performed are outlined below:

1. An ingot was prepared by double arc melting and then homogenized for 22 h at 900°C, yielding a cast rod 3 in. in diameter by 7 9/16 in. long. All heat treatments were performed in a vacuum of 10 - 20 μm Hg. Alloy

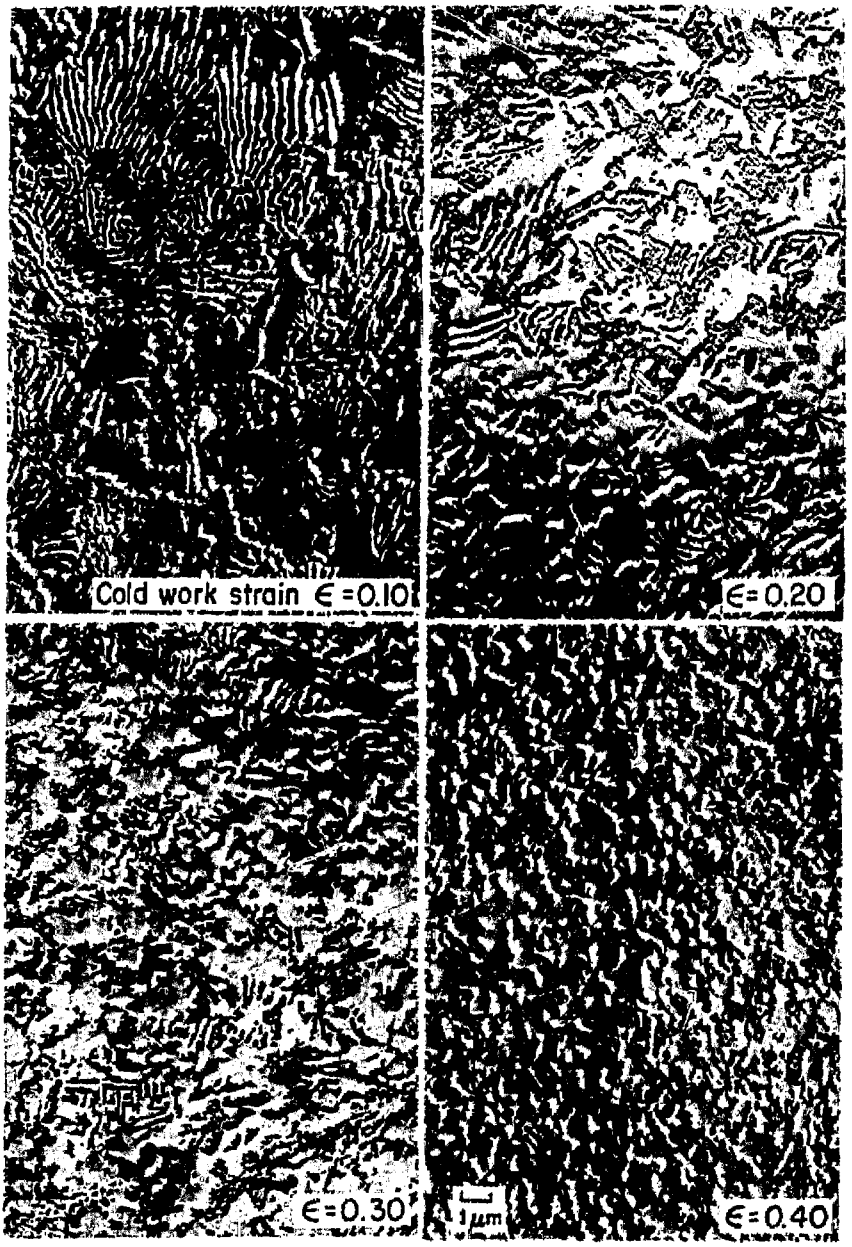

Fig. 4.15. The amount of cold work before transformation to the two-phase structure (550°C for 24 h) affects the size and degree of spheroidization of the structure after deformation at 625°C and $\dot{\epsilon} = 3 \times 10^{-4}/s$.

composition and impurity analysis for the top, sidewall and bottom of the ingot are given in Table 4.1

TABLE 4.1

ALLOY COMPOSITION AND IMPURITY CONTENT

	Composition, wt. pct		Impurity content,* ppm			
	Nb	Zr	C	Cu	Ni	Fe
Top	7.6	2.4	145	5	10	3
Middle	7.4	2.3	100	5	10	10
Bottom	7.3	2.5	81	5	10	3

* Other impurities were below detection limits of the spectrographic method used.

2. The rod was heated to 860°C, press-forged to a 1 3/4 in. hexagonal and machined to a 1.44 in. diameter round.

3. Two 6 in. rods were hot swaged at 900°C to rods of 0.860 in. diameter, held at 850°C for 2 h, furnace-cooled to 700°C in 3 h and water quenched.

4. The rods were swaged at room temperature to 0.663 - 0.669 in. diameter (true strain $\varepsilon = 0.50$).

5. Each rod was cut into thirds, inserted into a furnace preheated to 550 ± 5°C and annealed for 24 h to transform to a fine two-phase structure.

6. Furnace temperature was increased to 600 ± 2°C and the rods were hot-swaged to 0.40 in. diameter (true strain $\varepsilon = 1.0$, total strain $\varepsilon = 1.5$). Dies preheated to about 200°C were used. The surface temperature immediately after swaging was 400 - 510°C. The 600°C swaging temperature was selected to insure that material would not be heated above the transformation temperature, ≈637°C.

Swaging operations were used instead of plate rolling because round

cross-section compression and tensile specimens were desired. Thin, flat tensile specimens are difficult to test because of the oxidation problem. If round samples are needed, it is more efficient to process a round bar than a flat plate because for a given ratio of rod diameters or plate thicknesses the true deformation strain for the rod is twice that for the plate.

The purpose of the final hot-swaging operation was to insure a homogeneous, completely equiaxed microstructure which would be stable during elevated temperature deformation. This objective was achieved as shown in the microstructure after optimum processing, Fig. 4.16 and in a comparison with other structures for stress-strain curves obtained at 625°C and $\dot{\varepsilon} = 3 \times 10^{-4}$/s, Fig. 4.17. The swaged material has a finer grain size (≈0.5 μm) and is more spheroidized than structures obtained previously. At 625°C, this structure is stable with strain (no strain softening is observed) and considerable weaker than other structures, Fig. 4.17. The flow stresses of the individual phases, if tested as coarse-grain single-phase structures at 625°C and $\dot{\varepsilon} = 3 \times 10^{-4}$/s, are also shown in Fig. 4.17. The flow stress for α-U was taken from the data of Robinson and Sherby (1973). The flow stress for the γ_1 phase was estimated by extrapolating creep data for the γ phase (from Chapter VI) from 670°C to 625°C and then correcting for the difference in diffusion coefficients at 625°C for the γ and γ_1 phases (see Fig. 5.16, Chapter V). It is interesting to note that the initial flow stress of the lamellar $\alpha + \gamma_1$ structure is about equal to that for the γ_1 phase alone; however, when processed in fine-grain equiaxed form, the $\alpha + \gamma_1$ structure has a flow stress equal to about one-half that of the α phase

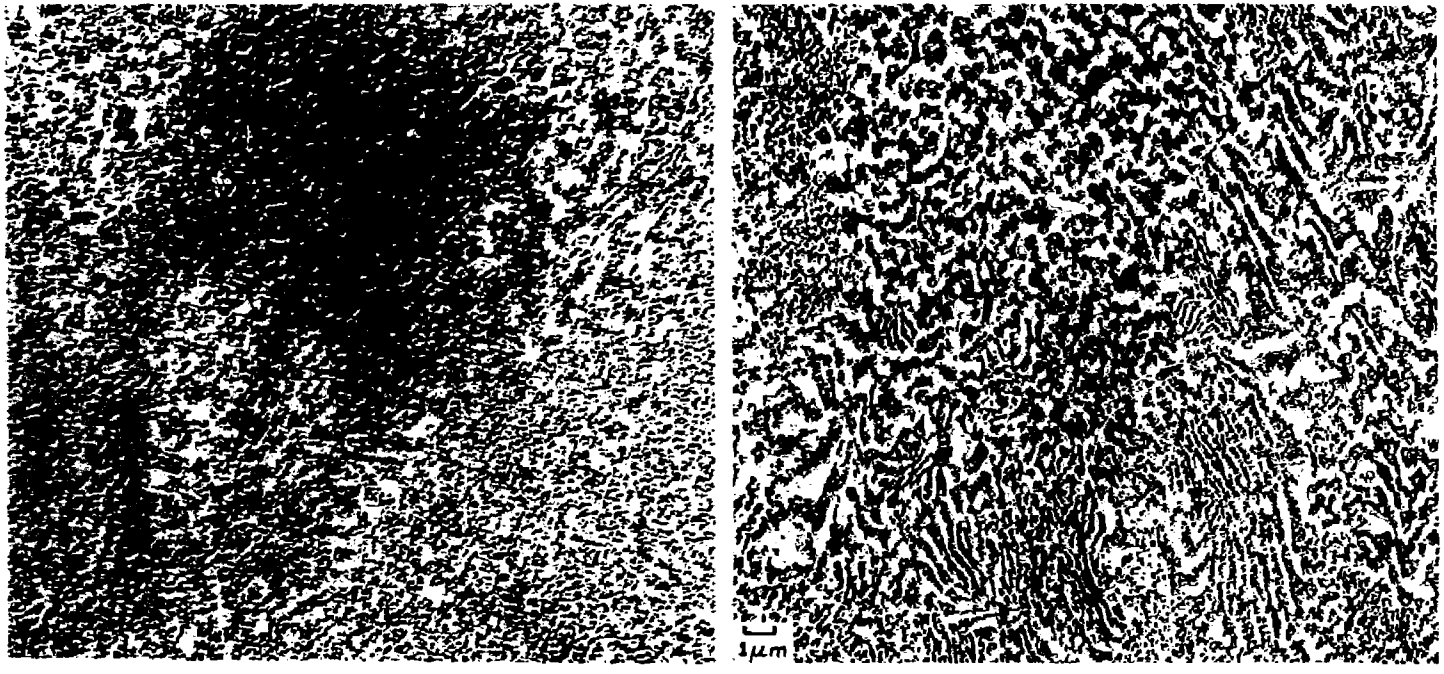

Fig. 4.16. Microstructure of U-7.5Nb-2.5Zr alloy rod processed at the Albany Metallurgy Research Center for attainment of a fine spheroidized structure. The typical spheroidized structure (left) is contrasted with the most atypical structure (right) showing a region of incomplete spheroidization. The average structure is more than 90 pct equiaxed.

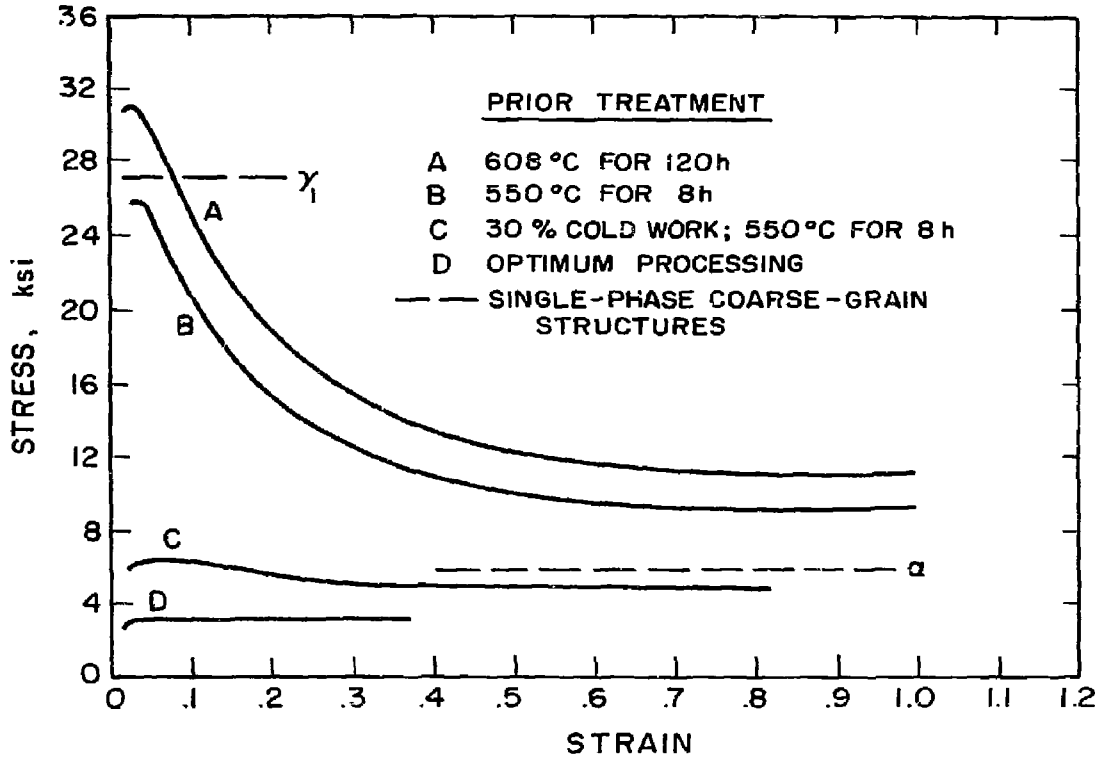

Fig. 4.17. Compression stress-strain curves showing the effect of microstructure on deformation at 625°C and $\dot{\varepsilon} = 3 \times 10^{-4}$/s.

alone. This comparison shows that a large decrease in strength can be obtained at high temperatures by production of a stable fine-grain equiaxed structure.

Fig. 4.18 is a comparison of flow stresses at different strain rates for five microstructures deformed at 625°C. In structures where strain softening was observed, the maximum flow stress was used in Fig. 4.18. Both Figs. 4.17 and 4.18 indicate that the coldwork-anneal treatment is important for efficiently processing a fine equiaxed microstructure, although hot working alone is sufficient if deformation is taken to very large strains ($\varepsilon > 2$).

The effect of two minor process parameters has not been discussed. One parameter is the quenching rate before cold working. Some compression specimens were water quenched from 700°C and others machined from a 1/2 in. thick plate water quenched from 850°C; the hardness values after quenching were DPH = 210 and DPH = 265, respectively. After cold working the specimens to $\varepsilon = 0.3$ and annealing at 550°C for 24 h, the more rapidly quenched specimens (low hardness value) had a flow stress about 5 pct less than the other specimens during deformation at 625°C and $\dot{\varepsilon} = 3 \times 10^{-4}/s$. The primary advantage of a rapid water quench is a reduction in the flow stress necessary to cold deform the material. The flow stress at room temperature at $\varepsilon = 0.4$ for material water quenched to a hardness DPH = 210 is 171,000 psi.

Other minor parameters are the anneal time and temperature. The 550°C temperature, at the nose of the "C" curve, was selected to minimize the transformation time. Lower transformation temperatures could lead to a finer structure with longer annealing times required for complete

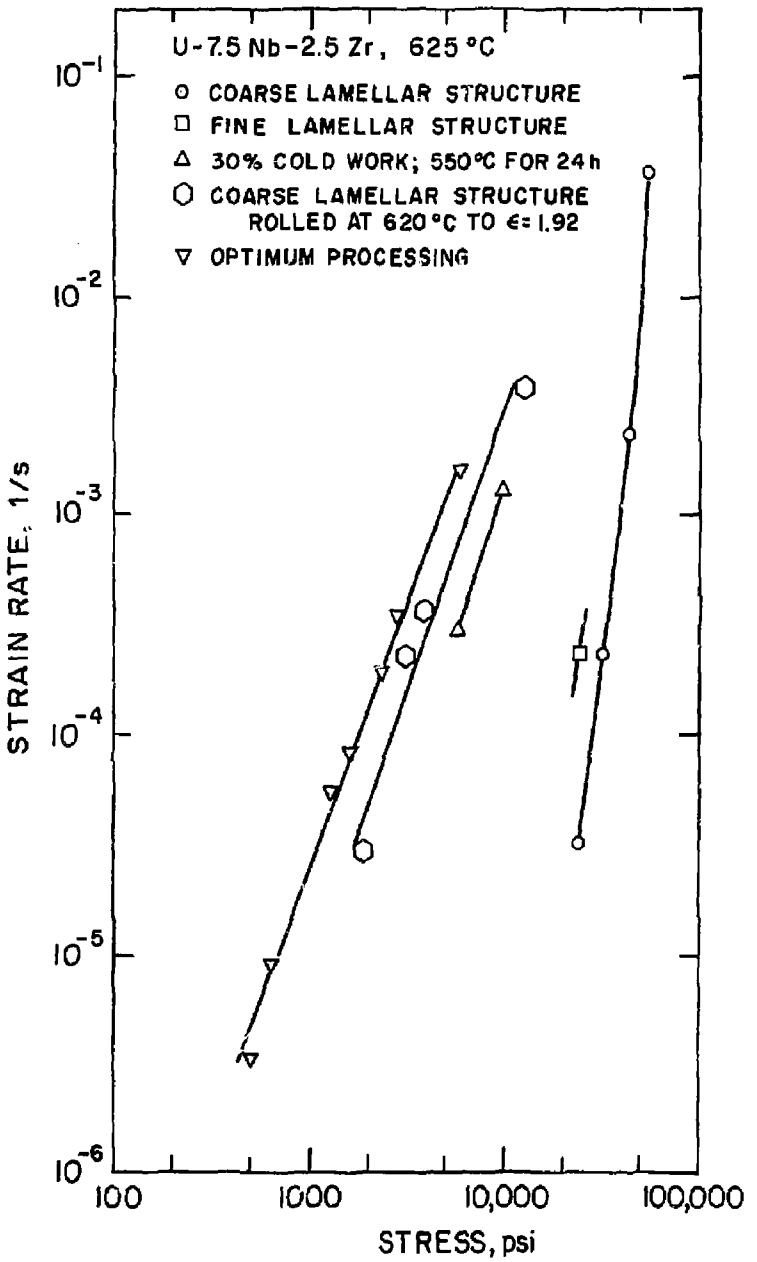

Fig. 4.18. The effect of microstructure is shown on a log $\dot{\varepsilon}$ vs. log σ diagram for deformation at 625°C. In structures where strain softening was observed, the maximum flow stress is shown.

transformation, but this method was not investigated. After cold work to $\varepsilon = 0.3$, it was found that 24 h annealing times at 550°C produced about a 5 pct reduction in flow stress during deformation at 625°C and $\dot{\varepsilon} = 3 \times 10^{-4}$/s compared to an 8 h anneal.

Conclusions

The lamellar $\alpha + \gamma_1$ structure (0.1 - 0.5 μm interlamellar spacing) formed by isothermal transformation is stable for at least 24 h during annealing at temperatures just below the monotectoid temperature (≈637°C or $0.56T_m$). Concurrent deformation during annealing greatly enhances the rate of spheroidization, but the spheroidization kinetics are slower than observed in a eutectoid-composition Fe-C alloy at the same homologous temperature and strain rate. This difference is probably due to a difference in grain boundary diffusion coefficients or a difference in the surface energy of the phase boundaries for the two materials. Although incomplete shperoidization was observed after strains as large as $\varepsilon = 1.9$, the results are in qualtitative agreement with spheroidization mechanisms proposed for steels. The activation energy for spheroidization was found to be about that estimated for grain boundary diffusion in the γ_1 phase. A high stress deformation condition led to a finer spheroidite size than a low stress condition, consistent with a model for deformation-enhanced spheroidization where subgrain boundaries act as high diffusivity paths and spheroidite spacing is related to the subgrain size.

A fine-grain equiaxed $\alpha + \gamma_1$ structure can be most efficiently produced by employing a quench-cold work-anneal treatment before hot working. An equiaxed structure with a 0.5 μm grain size was produced by gamma

quenching, cold working to $\varepsilon = 0.5$, annealing at 550°C for 24 h and hot working at 600°C to $\varepsilon = 1.5$ (total strain).

CHAPTER V

DEFORMATION OF THE FINE-GRAIN TWO-PHASE STRUCTURE FROM 500 TO 636°C

In this chapter the results of tension and compression tests for elevated temperature deformation of the fine-grain equiaxed structure in the two-phase region are reported. The creep data, and microstructural and fiber texture observations, are analyzed in terms of deformation mechanisms. Specifically, creep activation energies, stress exponents and the transition from a superplastic to a dislocation climb-controlled mechanism of creep are discussed.

Results

Tension and Compression Tests

Tension and compression tests on the U-7.5Nb-2.5Zr alloy processed in the $\alpha + \gamma_1$ region to a fine-grain equiaxed microstructure were conducted in the temperature range 500 - 636°C. Prior to testing, samples from the swaged rod material were annealed at 625°C for 1 h to achieve a stable grain size L of 1.0 μm. The tests were performed at constant crosshead speed with the data within each strain interval at a given crosshead speed adjusted to a constant true strain rate using an appropriate strain rate sensitivity exponent. In all cases, true stress vs. true strain data exhibited a constant flow stress with strain, with only a slight tendency for the flow stress to decrease with strain. This slight softening was not greater than 5 pct in any strain interval and probably occurred because the initial structure was not quite 100 pct equiaxed. The constant flow stress with strain is evidence that a steady state deformation mechanism exists. The exceptions to the constant flow

stress condition were tests at 636°C which were accidentally overheated (to, say, 640°C) and tests at 650 and 670°C. Once the phase transformation temperature (about 637°C) is exceeded, the transformation $\alpha + \gamma_I \rightarrow \gamma$ causes an increase in flow stress.

All of the tension and compression data for temperatures 500 - 636°C are shown in Fig. 5.1 on a log $\dot{\varepsilon}$ vs. log σ plot. These data are also listed in Table 5.1. For comparison, similar data for the coarse lamellar structure are shown in Fig. 5.2. In Fig. 5.2 the maximum flow stress is plotted. Tensile tests were also performed at 650 and 670°C; these data, Fig. 5.3, show an increase in strength with the $\alpha + \gamma_I \rightarrow \gamma$ transformation. The $\alpha + \gamma_I \rightarrow \gamma$ transformation was apparently more complete in the 670°C test, making the material stronger at 670°C than at 650°C.

Using a simple creep expression,

$$\dot{\varepsilon} = k \exp(-Q/RT) \ (\sigma/E)^n \qquad (5\text{-}1)$$

the data can be analyzed for the creep activation energy Q and the stress exponent n. In Eq. (5-1) stress is modulus-compensated, where E is the elastic modulus. As shown in Fig. 5.1, the stress exponent (measured at low stress) decreases from 5.5 at 500°C to 2.0 at 636°C. The stress exponent n = 5.5 is typical for metals whose deformation is controlled by dislocation climb [Cf. Bird et al. (1969)] and n = 2 is the value normally reported for superplastic flow [Cf. Davies et al. (1970 and Johnson (1970)]. The stress exponent n = 2 was also observed at 650 and 670°C, Fig. 5.3, but the data were taken at low strain values before necking and are probably not representative of a constant structure (grain growth is expected to occur in the single-phase region).

Several investigators [Avery and Backofen (1965), Avery and Stuart

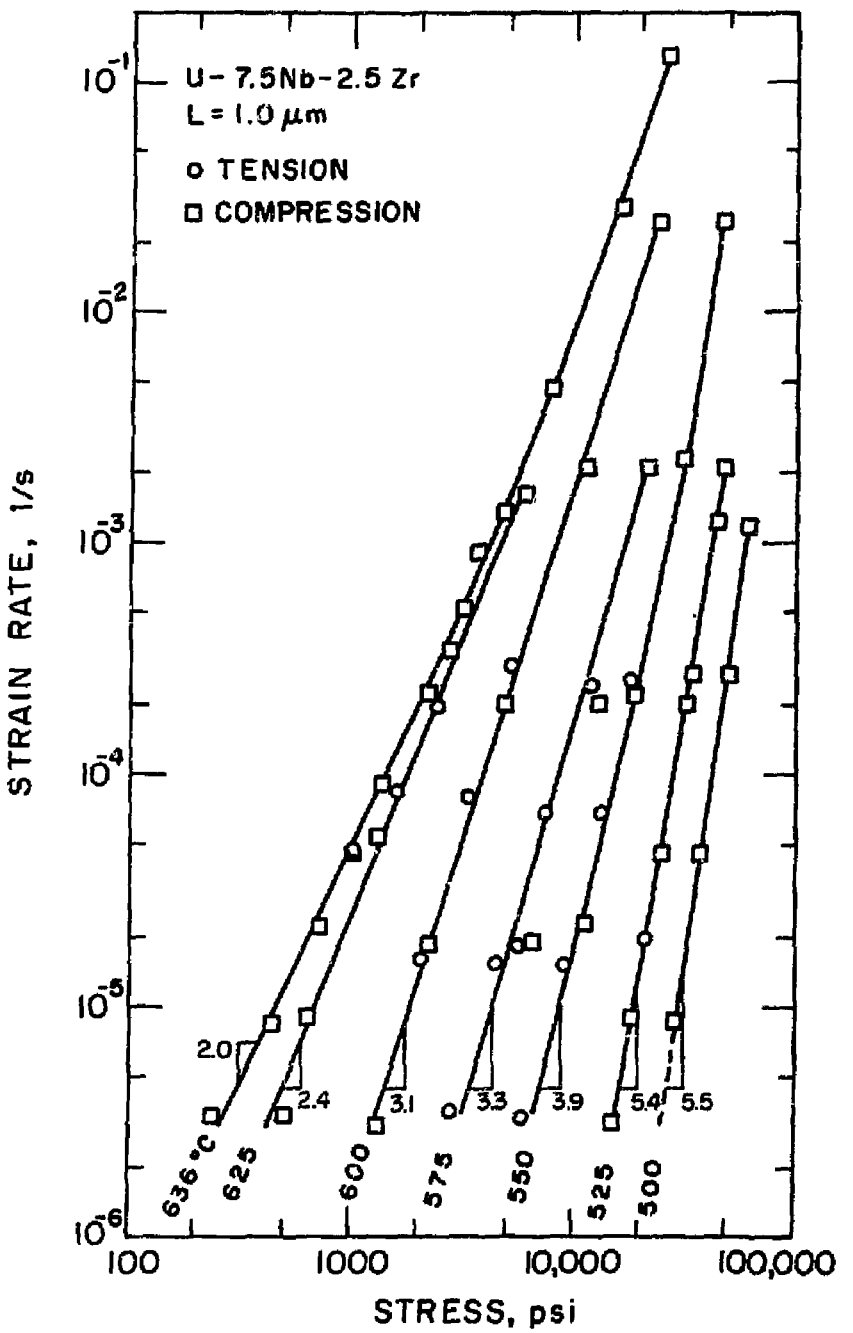

Fig. 5.1. Creep data for the equiaxed $\alpha + \gamma_1$ structure with a 1.0 μm grain size. The stress exponent decreases from 5.5 at 500°C to 2.0 at 636°C.

TABLE 5.1

CREEP DATA FOR THE FINE-GRAIN EQUIAXED $\alpha + \gamma_1$ STRUCTURE

T, °C	Test no.	σ, psi	$\dot{\epsilon}$, 1/s	T, °C	Test no.	σ, psi	$\dot{\epsilon}$, 1/s
500	108	28900	8.7E-6*	600	T15	2060	1.6E-5
		37700	4.6E-5			3280	8.0E-5
		49500	2.7E-4			5170	2.9E-4
		61500	1.20E-3		119	1330	3.1E-6
						2260	1.88E-5
525	107	18100	8.9E-6			4850	2.0E-4
		24800	4.7E-5			11200	2.1E-3
		33600	2.7E-4			23700	2.4E-2
		43600	1.23E-3				
	124	15200	3.2E-6	625	T10	2400	1.95E-4
		21500	2.0E-5		T11	1610	8.4E-5
		32000	2.0E-4		101	640	9.1E-6
		46900	2.1E-3			1280	5.4E-5
						2740	3.4E-4
550	T18	6020	3.3E-6			5860	1.51E-3
		9000	1.50E-5		126	500	3.4E-6
		13300	6.8E-5				
		18000	2.5E-4	636	T12	1020	4.6E-5
	124	6770	3.4E-6		102	1370	9.2E-5
		11200	2.3E-5			2160	2.2E-4
		18700	2.2E-4			3120	5.4E-4
		30000	2.3E-3			4800	1.37E-3
		46300	2.5E-2		105	3670	9.0E-4
						7790	4.7E-3
575	T16	2830	3.5E-6			16000	2.8E-2
		4480	1.53E-5			26000	1.29E-1
		7470	6.7E-5		126	240	3.4E-6
		11900	2.4E-4			450	8.6E-6
	126	6500	1.91E-5			730	2.2E-5
		12800	1.97E-4			1020	4.6E-5
		21300	2.1E-3				
	T13	5650	1.81E-5				

* 8.7E-6 is a compact notation for 8.7×10^{-6}.

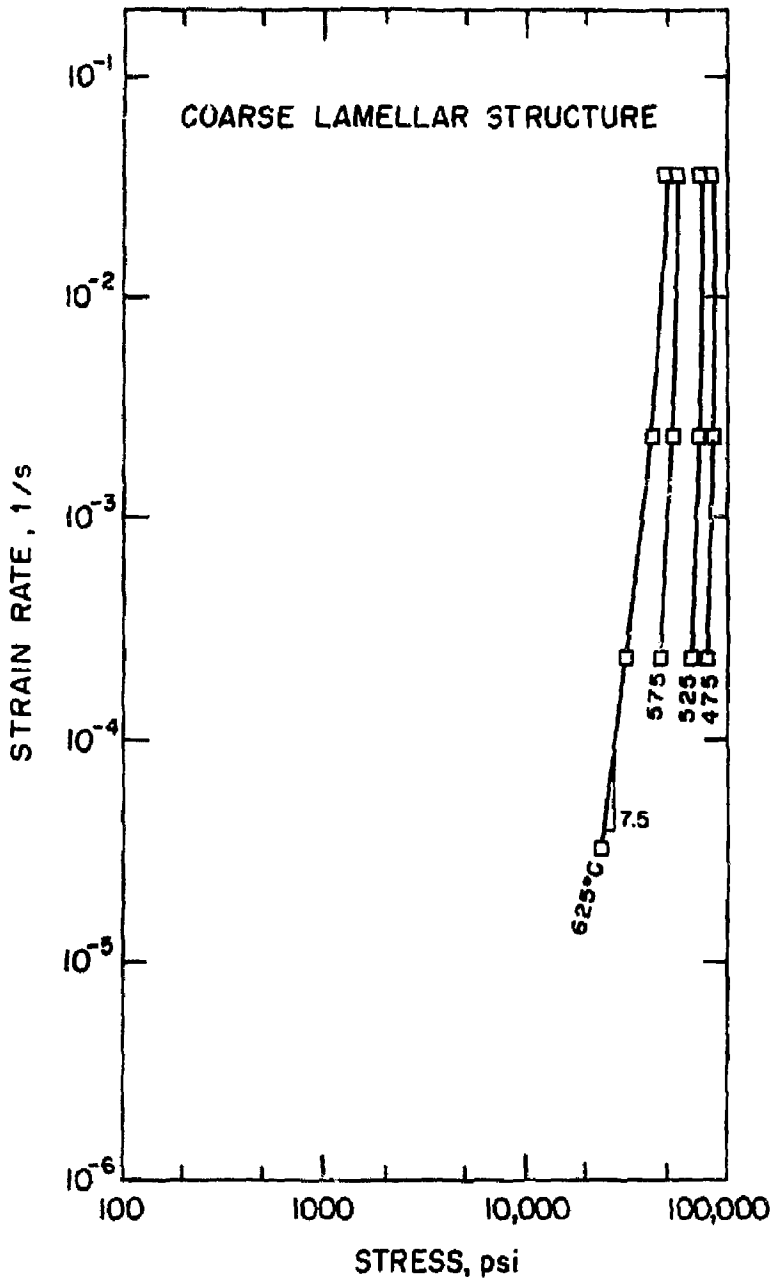

Fig. 5.2. The coarse lamellar structure is much stronger and has a higher stress exponent than the fine-grain equiaxed structure.

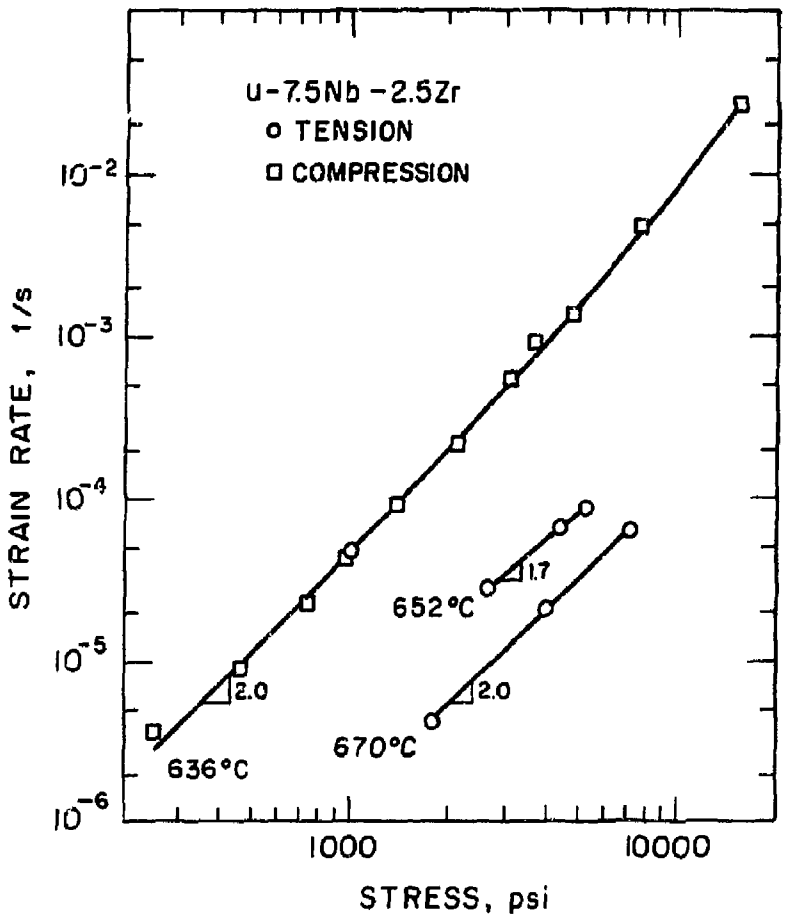

Fig. 5.3. Data taken during initial straining at temperatures above the transformation temperature (≈636°C) show a stress exponent of about two. The increase in strength with temperature is probably due to an increase in grain size with temperature in the single-phase region.

(1968), Morrison (1968) and Woodford (1969)] have shown that the total tensile elongation during elevated temperature deformation varies monotonically with the strain rate sensitivity exponent $m = 1/n$. Necking resistance increases with increasing m; for example, total elongations at $m = 0.5$ ($n = 2$) are much greater than at $m = 0.2$ ($n = 5$). Total tensile elongations for the U-7.5Nb-2.5Zr alloy are shown in Fig. 5.4. As expected, elongations increase from 120 pct (engineering strain) at 550°C where $n = 3.9$ to about 550 pct at 636°C where $n = 2.0$. A specimen deformed 560 pct at 634°C with an initial strain rate of 1×10^{-4}/s is shown in Fig. 5.5.

The temperature range 630 - 650°C produced the greatest elongations, 400 - 600 pct. At 650°C the phase transformation $\alpha + \gamma_1 \rightarrow \gamma$ during deformation may offer an additional form of neck resistance. Regions of the gage length which are hotter or have a higher flow stress (due to initial necking) than other regions could accelerate the $\alpha + \gamma_1 \rightarrow \gamma$ transformation and thereby increase the flow stress and retard localized deformation. At 670°C, total elongation dropped to 270 pct. Transformation to γ probably occurred more rapidly at this temperature and grain growth in the single-phase structure led to a transition from superplastic flow to normal coarse-grain behavior.

Activation energies were calculated for the creep data in Fig. 5.1. Since the stress exponent varies with temperature, activation energies calculated using Eq. (5-1) vary with stress. Therefore, a range of values for activation energy can be calculated between different temperatures. The method used was to calculate the range of activation energy between each pair of adjacent lines. If the mechanism of deformation changes

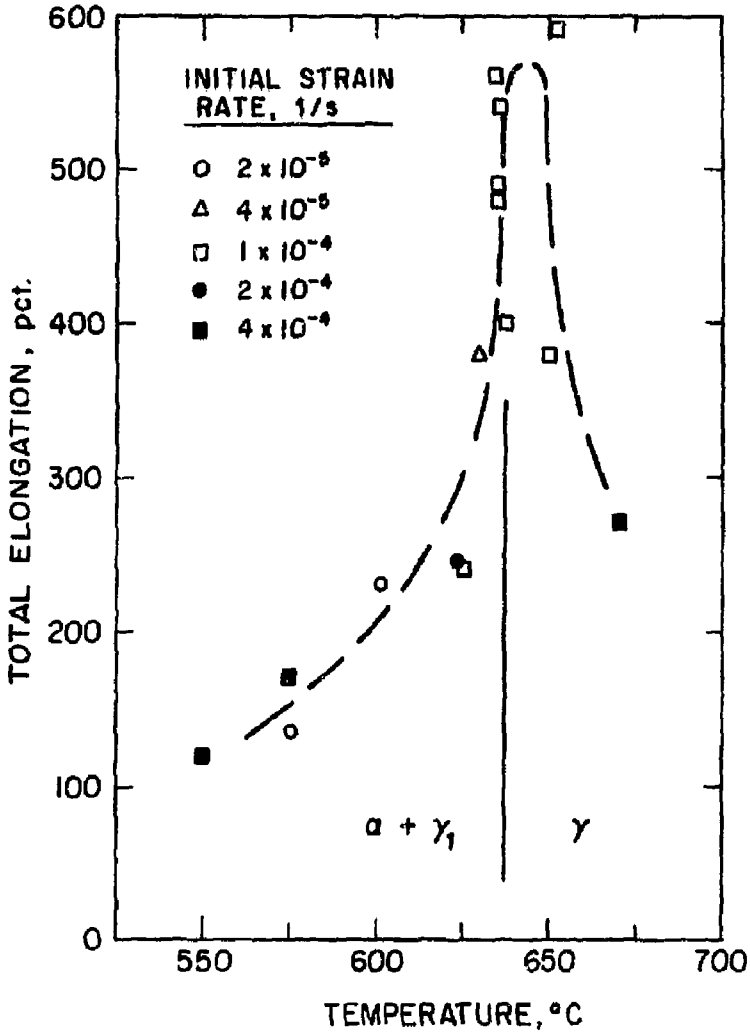

Fig. 5.4. Maximum elongations were obtained at 630 - 650°C, which corresponds to the region where the lowest stress exponents were observed.

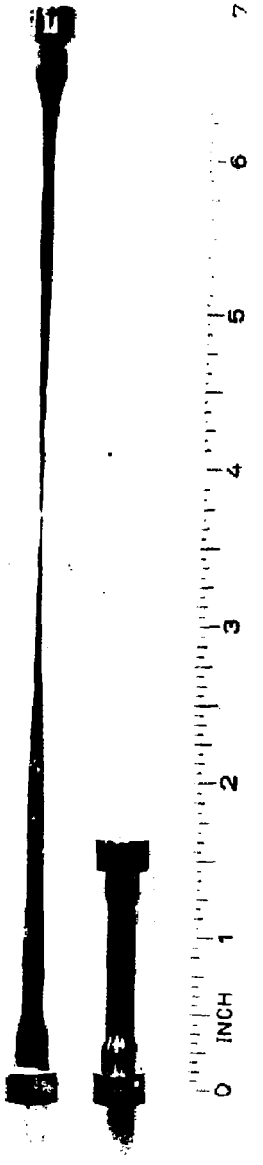

Fig. 5.5. A tensile specimen deformed 560 pct at 634°C at an initial strain rate of 1 x 10^{-4}/s. Deformation was not uniform as four individual necks can be seen.

with temperature (as indicated by the variation of n with temperature), the activation energy calculation at constant n can be approximated by using two adjacent curves with near-equal stress exponents. To be consistent, in the activation energy calculation the range of stress was chosen by using data in the 10^{-5} to 10^{-3}/s strain rate range. Activation energies were calculated from the expression

$$Q = -R \frac{d \ln \dot{\varepsilon}}{d\ 1/T} \Big|_{\sigma,E} - nR \frac{d \ln E}{d\ 1/T} \Big|_{\sigma,\dot{\varepsilon}} \qquad (5\text{-}2)$$

where the second term is a correction for modulus temperature variation. Dynamic modulus data were taken from Bugrov et al. (1972) who measured E as a function of temperature for a two-phase alloy of composition close to that studied in this investigation (U-6.80Nb-3.33Zr), Fig. 5.6. Thermal treatment of the material studied by Bugrov et al. included a final anneal at 550°C for 24 h which insures a fully transformed two-phase structure. The room temperature modulus value obtained by Bugrov et al., 20.49 x 10^6 psi, agrees well with the 21.7 x 10^6 psi value obtained by Wood (1972) for the U-7.5Nb-2.5Zr alloy. The difference is probably due to the higher Nb content in the U-7.5Nb-2.5Zr alloy. In addition, the rate of decrease of modulus with temperature, Fig. 5.6, is not as great as for α-U [in which the modulus decreases very rapidly with temperature, Armstrong et al. (1973)]. This behavior is reasonable, considering that the U-7.5Nb-2.5Zr alloy has an $\alpha + \gamma_1$ structure. The modulus correction term in Eq. (5-2) ranged from -9 kcal/mole at 513°C to -6 kcal/mole at 631°C.

Calculated activation energies for creep are given in Table 5.2. The mean activation energy calculated in the temperature range 513 - 613°C is 123 kcal/mole. This value is much greater than the 60 - 80 kcal/mole

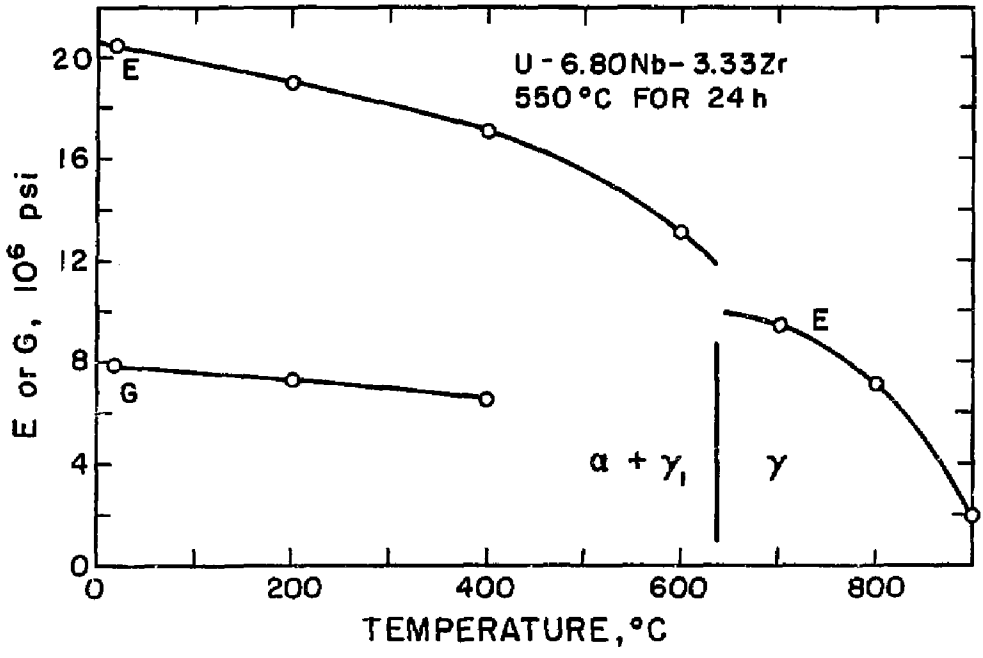

Fig. 5.6. Dynamic modulus data of Bugrov et al. (1972) for the U-6.80Nb-3.33Zr alloy.

Table 5.2

CALCULATED CREEP ACTIVATION ENERGIES

Temperature, °C	Q, kcal/mole
513	109 - 116
538	125 - 145
563	96 - 115
588	134 - 143
613	100 - 143
631	44 - 73

values reported by Fedorov et al. (1972) for Nb tracer diffusion in the γ_1 phase for a range of γ_1 compositions (Nb is the slowest diffusing species in the γ_1 phase). At 631°C, where superplastic deformation is observed, the activation energy for creep is much less than at lower temperatures.

Microstructure

Typical microstructures are shown in Fig. 5.7 for a tensile specimen deformed at 624°C and an initial strain rate of 2×10^{-4}/s. Annealing the processed material (0.5 μm grain size) at 624°C produces a 1.0 μm grain size which is stable during deformation. After extreme local strain (2100 pct), the grain size increased to 1.5 μm. The structure remains equiaxed after deformation and the grain boundaries (phase boundaries) are curved, not straight. No evidence of cavitation or void formation near the point of failure was found.

Fig. 5.8 shows the microstructure of a compression specimen deformed at 500°C at 10^{-5} to 10^{-3}/s to $\varepsilon = 0.34$. The structure is equiaxed but grain boundaries are more jagged than the gently-curved bulbous-like

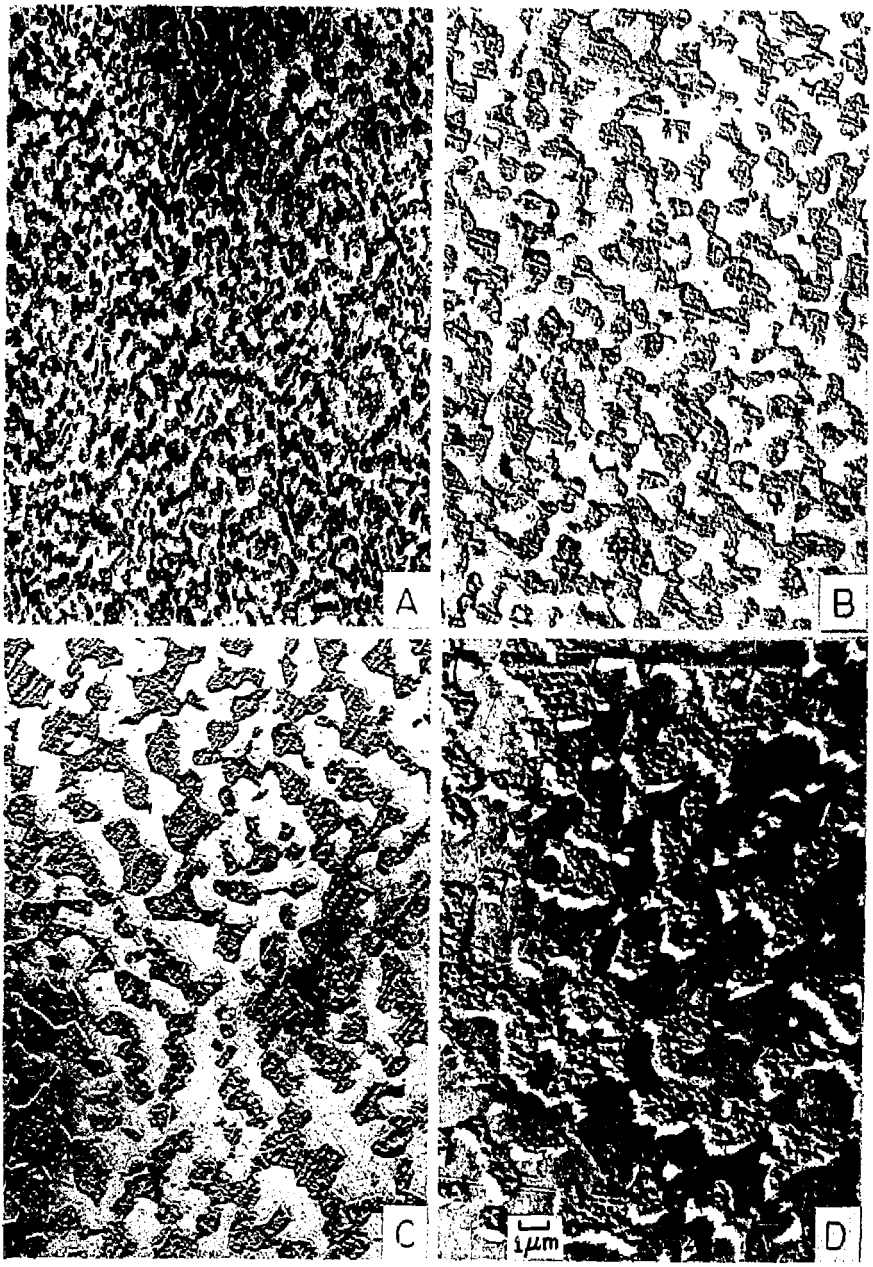

Fig. 5.7. The equiaxed $\alpha + \gamma_1$ structure is shown: (A) as processed (L = 0.5 μm); (B) after annealing at 624°C during a test (grip region, L = 0.9 μm); (C) after deformation at 624°C at an initial strain rate of 2 x 10^{-4}/s to ε = 0.5 (L = 1.0 μm); (D) after deformation as in (C) to >2000 pct local strain near the point of failure (L = 1.5 μm).

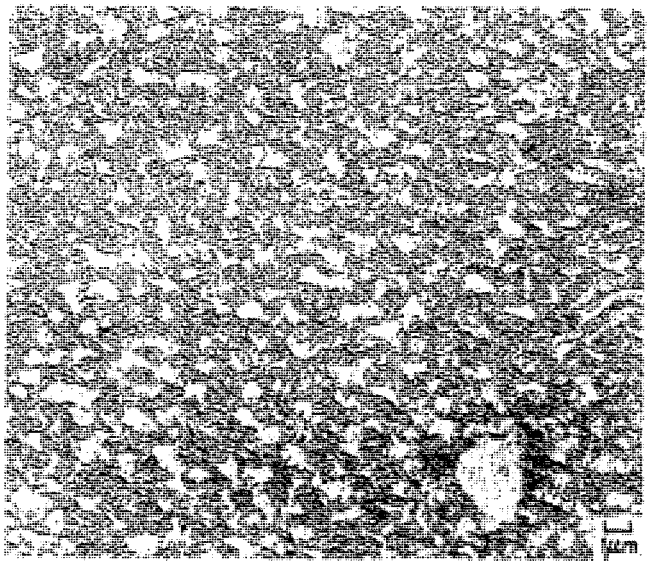

Fig. 5.8. Microstructure of a compression specimen after deformation to $\varepsilon = 0.34$ at 500°C at strain rates of 10^{-3} to 10^{-3}/s.

Fig. 5.9. Microstructure of a tensile specimen near the point of failure after deformation at 652°C at an initial strain rate of 1×10^{-4}/s. The structure is a single γ phase with a 5 - 10 μm grain size. Some $\alpha + \gamma_1$ lamellar colonies formed during the furnace cool after the test.

boundaries in Fig. 5.7.

A tensile specimen deformed to failure at 590 pct elongation at 652°C and an initial strain rate of 1×10^{-4}/s was examined near the region of failure. The structure, Fig. 5.9, is a single γ phase with a 5 - 10 μm grain size. The specimen was furnace-cooled and some lamellar colonies formed during partial transformation to $\alpha + \gamma_1$. The γ grain boundaries are only seen when delineated by the transformed product.

Effect of Texture

Transverse compression specimens machined from the swaged rod material exhibited slightly different behavior than the longitudinal specimens. Fig. 5.10 shows a shape change during deformation where the originally circular cross-section became elliptical. No shape change was observed for longitudinal specimens. The greatest shape change for transverse specimens occurred at 500°C, with no shape change occurring at 636°C.

Transverse specimens were slightly weaker than longitudinal specimens, Figure 5.11, with a trend for the difference between longitudinal and transverse creep rates at a given stress to decrease with increasing temperature. At 636°C the transverse specimen was stronger than longitudinal specimens. The reason is that, probably due to overheating, the transverse specimen was more transformed to the γ phase than longitudinal specimens. Fig. 5.12 shows that the structure of the 636°C transverse specimen is nearly a single γ phase.

Fiber texture plots were determined for the rod material as-swaged and after deformation. Relative numbers (compared to a random sample) of (110) plane poles in the γ_1 phase and (111) plane poles in the α phase are shown in Fig. 5.13 as a function of the angle ϕ from the rod

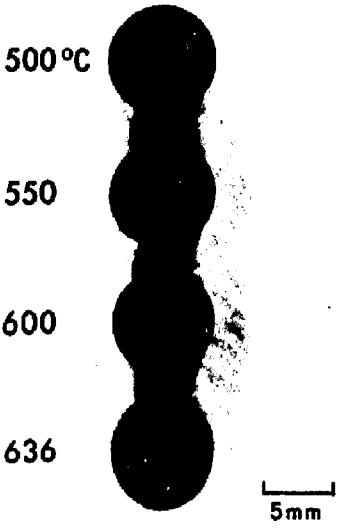

Fig. 5.10. Macrophotograph of transverse compression specimens viewed end-on after deformation to $\varepsilon = 0.6$ at strain rates of 3×10^{-6} to 4×10^{-2}/s. The shape change to an elliptical cross section is most prominent at 500°C; no shape change occurred at 636°C.

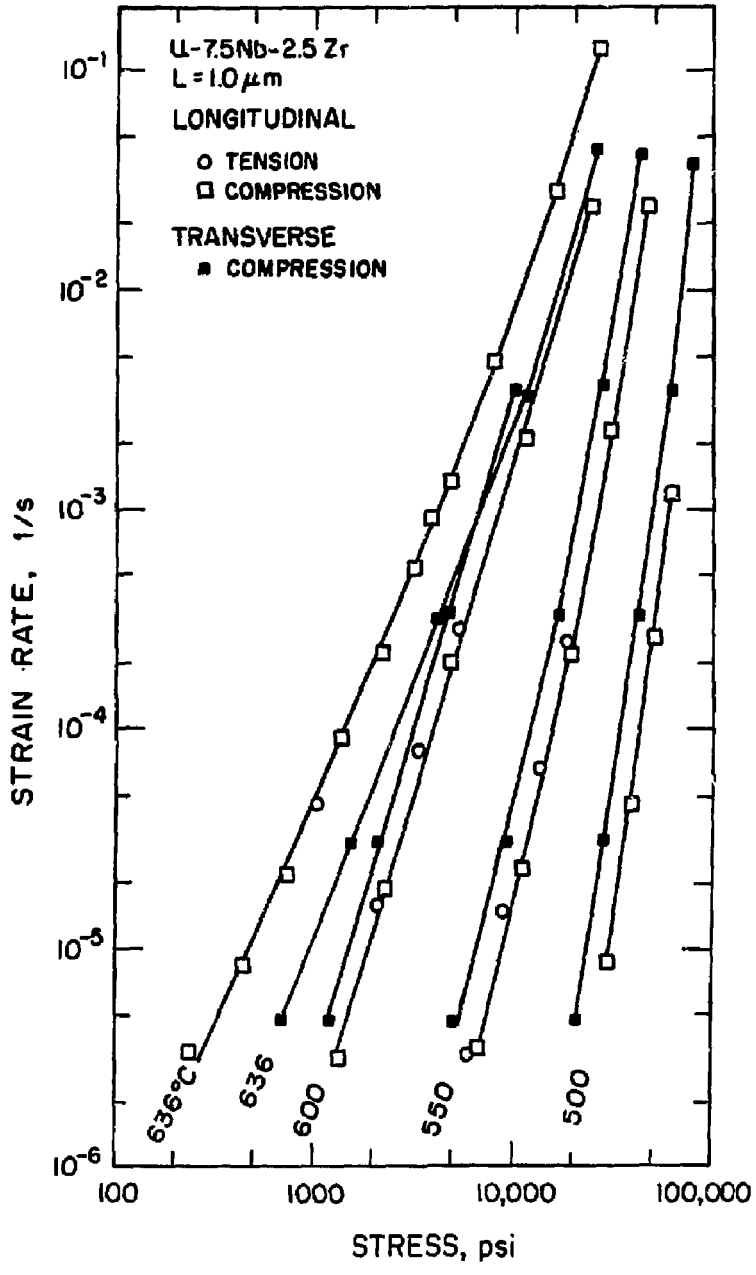

Fig. 5.11. Transverse specimens were slightly weaker than longitudinal specimens. The 636°C transverse specimen was probably overheated, causing an increase in strength due to grain growth in the single-phase region.

Fig. 5.12. Microstructure of the 636°C transverse specimen after deformation showing almost complete transformation to the γ phase.

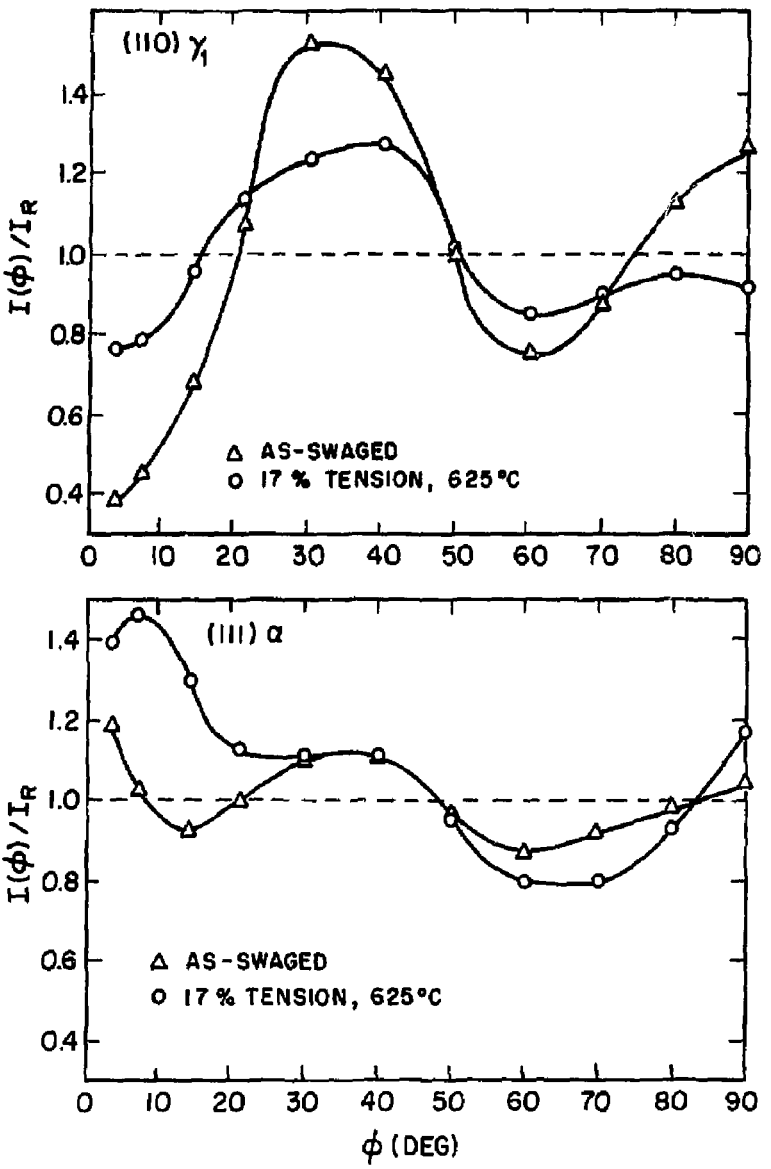

Fig. 5.13. Fiber texture plots showing a decrease in preferred orientation in the γ_1 phase after superplastic deformation. The indicated increase in preferred orientation in the α phase after deformation at 625°C is probably not significant because the fiber texture measurement technique is not accurate at low values of the angle ϕ.

axis. Preferred orientation decreased in the γ_1 phase after 17 pct strain at 625°C. The (111) plot for the α phase is less accurate than the fiber texture plot for the γ_1 phase because of a lower diffraction peak intensity. Diffraction peaks for other crystallographic planes in the α phase were not used because of overlap with γ_1 peaks or because of lower peak intensity. For the as-swaged structure, the α phase is less textured than the γ_1 phase. An indicated increase in preferred orientation in the α phase after deformation at 625°C is probably not significant, especially at low values of the angle ϕ where the fiber texture measurement technique used is not accurate [Edwards (1971].

Discussion

Activation Energy for Creep

In order to relate creep activation energies to atom diffusion, diffusion coefficients in the alpha and gamma phases were calculated from data in the literature. The lattice diffusion coefficient D_L in the α phase, taken as pure α-U, was reported by Adda and Kirianenko (1962) from 580 to 650°C:

$$\alpha\text{-U} \quad D_L = 2 \times 10^{-3} \exp(-40000/RT) \ cm^2/s$$

Grain boundary diffusion in α-U has been reported by Fedorov et al. (1966) in the range 835 - 906 K:

$$\alpha\text{-U} \quad D_B = 320 \exp(-44300/RT) \ cm^2/s$$

As discussed by Bly et al. (1973b), the accuracy of this grain boundary diffusion data is questioned because, in relation to other metals, both the D_o and Q values appear too high.

In the gamma phase of the U-Nb-Zr system, diffusion coefficients are strong functions of composition [Fedorov et al. (1969,1972)]. Tracer diffusion coefficients for U, Nb and Zr sharply decrease with increasing

Nb additions to γ-U. Zr additions increase the diffusion coefficients. Both γ-U and β-Zr are known to have anomolously high diffusion coefficients characterized by low values of both D_o and Q [Le Claire (1965)].

The only available diffusion data in the ternary system U-Nb-Zr is that of Fedorov et al. (1969, 1972). The Fedorov et al. (1972) data in the U-Nb binary system are in general agreement with that reported by Peterson and Ogilvie (1963), so we assume that the one data source used is reasonably accurate. The temperature range studied by Fedorov et al. was 800 - 1900°C, with the low end of the temperature range presumably used in the U-rich region of the ternary diagram which is of interest in the present work. Therefore, considerable extrapolations are needed to calculate diffusion coefficients at temperatures as low as 500°C.

The diffusion data of Fedorov et al. (1969, 1972) for the U-Nb-Zr system can be summarized by plots of constant activation energy lines on the ternary diagram, Fig. 5.14, and by the relation

$$D_o = 10^{-9} \exp(Q/3500) \text{ cm}^2/\text{s} \qquad (5\text{-}3)$$

where Q is expressed in kcal/mole. For a given composition and temperature, the tracer diffusion coefficient for, say, Nb is calculated from

$$D_{Nb} = (D_o)_{Nb} \exp(-Q_{Nb}/RT)$$

where Q_{Nb} is determined from Fig. 5.14 and $(D_o)_{Nb}$ is calculated from Eq. (5-3) using Q_{Nb}. A relation between D_o and Q, in the same form as Eq. (5-3), was also empirically derived by Fedorov (1967) for diffusion in austenitic iron base alloys.

Because diffusion in the γ_1 phase is strongly a function of composition, compositions of the γ_1 phase must be known with some accuracy. As discussed in Chapter IV, the ternary phase diagram available in the

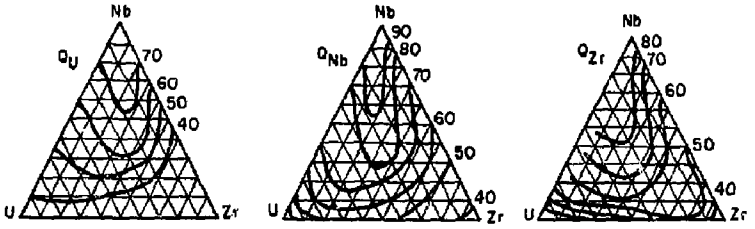

Fig. 5.14. Activation energies (in kcal/mole) for lattice diffusion in the U-Nb-Zr system as determined by Fedorov (1972). The diagrams are drawn on an atom-fraction basis.

literature is not accurately defined for γ_1 compositions below 600°C. One method used to determine γ_1 compositions was electron microprobe analysis. This method, however, proved ineffective as the beam could not be focused small enough to sample only the γ_1 phase region in the $\alpha + \gamma_1$ structure. Although some lattice parameter data are available for the U-Nb-Zr system [Dwight and Mueller (1957)], the data do not specifically cover the composition range of interest.

The method adopted for measuring γ_1 compositions was volume fraction analysis using quantitative metallography. Using density data directly measured and calculated from estimated lattice parameter data, γ_1 phase compositions were calculated from the volume fraction measurements at 500 and 625°C. The calculation was relatively insensitive to density; thus, the accuracy of the calculated γ_1 phase compositions is greater than the accuracy of the density values used. Density data for the γ_1 phase, ρ_γ, are summarized in Fig. 5.15 and density of the α phase was taken as 19.07 gm/cm^3.

Samples were water-quenched from 500 and 625°C after annealing and deforming at temperature to coarsen the microstructure. Volume fraction of the γ_1 phase, V_γ, was measured using electron replica micrographs. Calculations are summarized in Table 5.3 with calculated compositions given in both wt. fraction (X^w) and at. fraction (X).

Table 5.3

CALCULATED γ_1 PHASE EQUILIBRIUM COMPOSITIONS

T, °C	V_γ	ρ_γ, gm/cm^3	X^w_{Nb}	X^w_{Zr}	X_{Nb}	X_{Zr}
500	0.40 ± .02	13.1	0.239	0.080	0.410	0.139
625	0.78 ± .02	15.8	0.1005	0.0335	0.213	0.0722

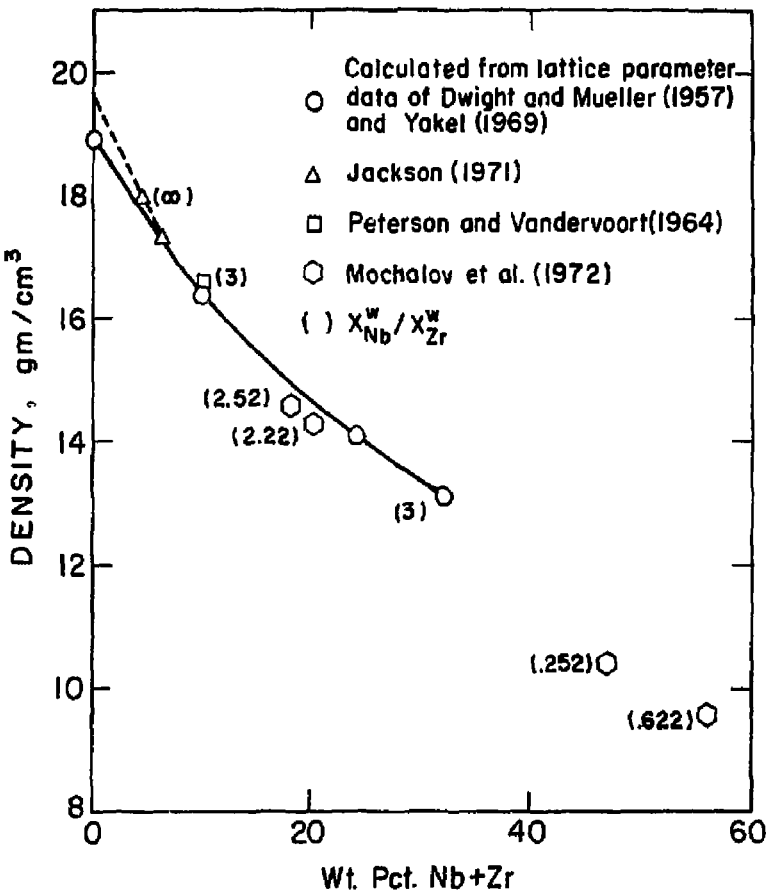

Fig. 5.15. Density of the gamma phase for U-Nb-Zr alloys as a function of composition. The curve calculated from lattice parameter data was used in the calculation of γ_1 compositions from volume fraction measurements for the U-7.5Nb-2.5Zr alloy.

To calculate an average diffusion coefficiert in the gamma phase which could be related to creep deformation, an averaging equation from Weertman's 1968 paper was used:

$$D_W = \prod_i D_i \left\{\sum_i \left(X_i \prod_{j \neq i} D_j\right)\right\}^{-1} \qquad (5\text{-}4)$$

where D_i is the diffusion coefficient for the i th atom species and X_i is the atom fraction. In Eq. (5-4) the off-diagonal terms in the diffusion coefficient matrix are assumed negligible. For a ternary system the average diffusion coefficient D_W can be calculated from

$$\frac{1}{D_W} = \frac{X_1}{D_1} + \frac{X_2}{D_2} + \frac{X_3}{D_3}$$

Lattice diffusion in the U-7.5Nb-2.5Zr alloy is summarized in Fig. 5.16 with D_W plotted for three different gamma compositions and D_L plotted for self-diffusion in α-U. The gamma-phase diffusion data are normal in the sense that D_o values at constant composition are in the range 0.02 to 17 cm^2/s. In terms of activation energies, the values in Fig. 5.16 at constant composition are higher than for pure bcc metals with $K \cong 20$ in the relation

$$Q = K R T_m \qquad (5\text{-}5)$$

Melting temperatures for the three gamma compositions used in Fig. 5.16 were determined as the average of solidus and liquidus temperatures reported by Badayera and Kuznetson (1971). Most bcc metals have activation energies for self-diffusion such that the parameter K in Eq. (5-5) has a value of about 17 [Sherby and Simnad (1961)].

Fig. 5.16 shows that the diffusion coefficient in the gamma phase decreases rapidly as the Nb and Zr content increases. Because the equilibrium γ_1 composition, indicated by solid symbols in Fig. 5.16, changes significantly as a function of temperature in the range 500 -

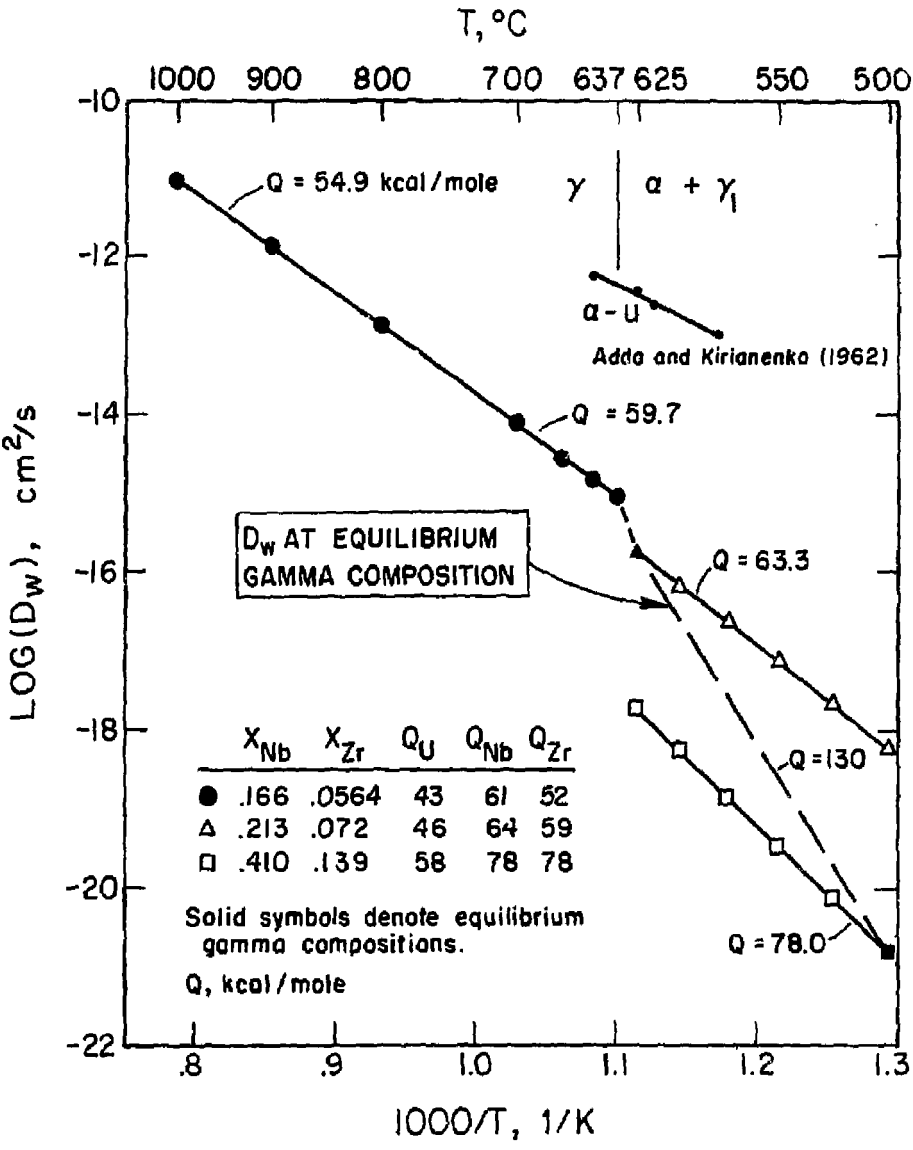

Fig. 5.16. Weertman's (1968) average lattice diffusion coefficient for three gamma-phase compositions in the U-7.5Nb-2.5Zr (U-16.60Nb-5.64Zr, at. pct) alloy as a function of reciprocal temperature. Equilibrium gamma compositions are denoted by solid symbols. In the two-phase region $\alpha + \gamma_1$, the apparent activation energy at equilibrium composition between 500 and 625°C is 130 kcal/mole. Lattice diffusion data for α-U are also plotted.

625°C, the apparent or calculated activation energy at equilibrium composition is very high. For equilibrium composition, the average activation energy calculated between 500 and 625°C is 130 kcal/mole. This value is compared to activation energies determined from creep data (Table 5.2) in Fig. 5.17. In the temperature range 510 - 610°C there is general agreement between activation energies calculated from creep and lattice diffusion data. This correlation suggests that the rate-controlling mechanism during creep at 510 - 610°C is probably the rate of dislocation climb which is governed by lattice diffusion. It should be noted that the high calculated activation energy of about 130 kcal/mole is an apparent value due to a change in structure (composition) with temperature. For the gamma-phase compositions shown in Fig. 5.16, at constant structure the activation energies for lattice diffusion are in the range 60 - 80 kcal/mole.

The diffusion coefficients at equilibrium composition between 500 and 625°C were estimated in Fig. 5.16 as a straight-line interpolation between the calculated diffusion coefficients at 500 and 625°C (dashed line in Fig. 5.16). Considering the uncertainty in the composition measurements and in the calculated average diffusion coefficients in the ternary system, this linear interpolation between 500 and 625°C is considered as good an estimate as the data warrants. One calculation was made in which Weertman's (1968) average diffusion coefficient was determined as a function of temperature for a composition half-way (on an atom fraction basis) between the equilibrium compositions at 500 and 625°C. This calculation showed that the straight-line interpolation in Fig. 5.16 implies that there is a linear variation in equilibrium

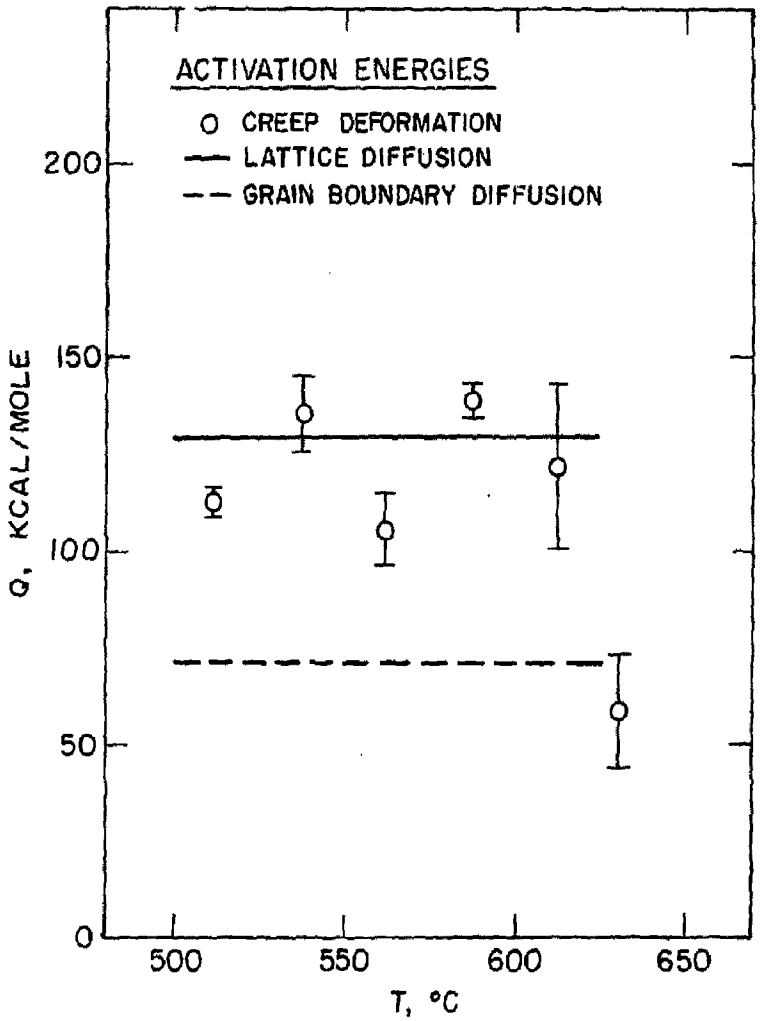

Fig. 5.17. Comparison of activation energies for creep and diffusion. The creep activation energy is about equal to that for lattice diffusion at 513 - 613°C and about equal to that for grain boundary diffusion at 631°C.

composition of the γ_1 phase with temperature between 500 and 625°C. Although the temperature versus equilibrium composition curve on the phase diagram is expected to be curved, the curvature is probably very slight for the γ_1 phase in the U-7.5Nb-2.5Zr alloy because there is a large composition change in a relatively small range in temperature. The data of Dwight and Mueller (1957) are consistent with this analysis in that they reported vertical sections of the U-Nb-Zr ternary phase diagram (i.e., temperature versus composition for constant values of X^w_{Nb}, X^w_{Zr} or X^w_{Nb}/X^w_{Zr}) which showed an essentially linear variation in the composition of the γ_1 phase with temperature. Their data, however, were limited to temperatures $\geq$600°C. Thus, although the dashed line in Fig. 5.16 could be slightly curved, the straight-line interpolation is considered a realistic estimate of diffusion coefficients at equilibrium concentration between 500 and 625°C.

Since the activation energy for superplastic deformation is often associated with that for grain boundary diffusion [Cf. Davies et al. (1970) and Johnson (1970)], it would be desirable to estimate the activation energy for grain boundary diffusion in the U-7.5Nb-2.5Zr alloy. From the correlation of grain boundary diffusion data for pure metals in Chapter II, most metals fit the relation

$$D_B = 1 \exp(-11\ T_m/T)\ cm^2/s$$

where $D_o = 1\ cm^2/s$ and $K = 11$ in Eq. (5-5). Even data for γ-U, which has anomolously low lattice diffusion coefficients, fits Eq. (5-6). Using the melting temperatures of the equilibrium γ_1 phase compositions at 500 and 625°C, Eq. (5-6) gives values of D_B of $3.1 \times 10^{-12}\ cm^2/s$ at 500°C and $1.6 \times 10^{-9}\ cm^2/s$ at 625°C. For equilibrium γ_1 composition,

the average activation energy for grain boundary diffusion between 500 and 625°C is calculated to be 72 kcal/mole. This value is also shown in Fig. 5.17 and compares favorably with the activation energies determined from creep data between 625 and 636°C where superplastic flow is observed.

It is apparent that creep of the two-phase structure is not controlled by diffusion in the α phase. The observed activation energies are too high to relate to diffusion in the α phase and, as shown in Fig. 5.16, for a given temperature the lattice diffusion coefficient in the α phase is several orders of magnitude greater than that in the γ_1 phase. Thus, creep deformation is not expected to be limited by atom diffusion in the α phase. Because of the difference in melting temperatures between the α and γ_1 phases, grain boundary diffusion is also expected to be much more rapid in the α phase than the γ_1 phase for a given temperature. Homologous temperatures are shown in Fig. 5.18 for the α and γ phases and for equilibrium concentrations at 500 and 625°C for the γ_1 phase. The melting temperature for the α phase, 1239K, was calculated by Ardell (1963) using thermodynamic data. For example, at 625°C the α phase is at $0.73T_m$ and the γ_1 phase is at $0.54T_m$. From Eq. (5-6) the corresponding D_B values are 3×10^{-7} cm^2/s and 2×10^{-9} cm^2/s for α and γ_1, respectively.

In Fig. 5.18, homologous temperatures of the γ_1 phase at equilibrium composition between 500 and 625°C were estimated assuming that the melting temperature of the γ_1 phase at equilibrium composition varies linearly with temperature. This assumption is reasonable because, as discussed previously, the composition of the γ_1 phase varies approx-

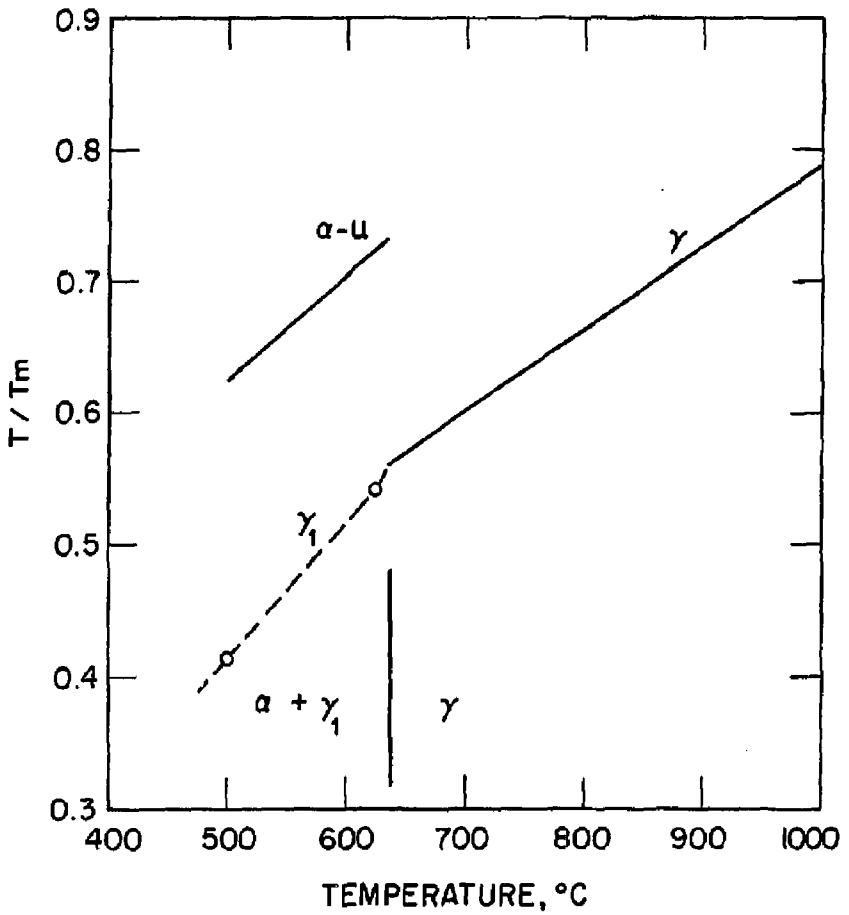

Fig. 5.18. Homologous temperatures for the α,γ and γ_1 phases in the U-7.5Nb-2.5Zr alloy as a function of temperature. The homologous temperature of the γ_1 phase decreases rapidly with decreasing temperature because the composition (and, therefore, the melting temperature) changes with temperature.

imately linearly with temperature and because the melting temperature variation with composition is also essentially linear [Badayera and Kuznetson (1971)]. It should be pointed out that, assuming Eq. (5-6), a constant apparent activation energy for grain boundary diffusion for equilibrium composition between 500 and 625°C implies that T_m varies linearly with T.

Superplastic Creep Theories

Creep data for different materials can best be compared using a diffusion-compensated strain rate and a modulus-compensated stress [Cf. Sherby and Burke (1968)]. In this case creep deformation over a range of temperature, stress and strain rate for materials deforming with the same creep mechanism operative can be described by a single equation. Other parameters such as grain size [Cf. Garofalo (1965)], subgrain size [Cf. Robinson (1972)] and stacking fault energy [Cf. Barrett and Sherby (1965)] may also be important, but all data to date for superplastic deformation suggest that only grain size is important as an additional parameter. Subgrain size is not important because subgrains are not observed in very fine-grain specimens deformed superplastically at a low stress. Sherby and Young (1972) relate subgrain size λ to σ/E by the equation

$$\lambda = 4\ b\ (\sigma/E)^{-1}$$

where b is Burgers vector. If superplastic deformation is observed at a maximum σ/E value of 10^{-3} [Bird et al. (1969) and Vaidya et al. (1972)], then the finest subgrain size expected is about 1.2 μm. This value is about the same as the finest grain size for superplastic structures; thus, the implication is that subgrains will not form during superplastic

deformation.

The stacking fault energy parameter primarily affects the rate of dislocation climb. This parameter probably has little significance in superplastic deformation because there is little evidence for dislocation motion during deformation. Small inert precipitate particles introduced in superplastic structures did not alter the creep behavior [Nicholson (1972) and Geckinli (1973)]. If dislocation motion were active in superplastic deformation, the precipitate dispersion should affect the creep deformation.

The most complete correlation of superplastic creep data to date is expressed by the phenomenological equation:

$$\frac{\dot{\gamma}\, k\, T}{D_B\, G\, b} = A \left(\frac{b}{d}\right)^2 \left(\frac{\tau}{G}\right)^2 \qquad (5\text{-}7)$$

[Bird et al. (1969) and Vaidya et al. (1972)]. The lefthand term in Eq. (5-7) is essentially a diffusion-compensated strain rate with other factors added to obtain a dimensionless quantity. In Eq. (5-7), $\dot{\gamma}$ is the shear strain rate ($\dot{\gamma} = 2\dot{\varepsilon}$), τ is the shear stress ($\tau = \sigma / \sqrt{3}$), G is the shear modulus (G = 0.4 E), b is Burgers vector (taken as 3×10^{-8} cm), d is the grain diameter, D_B is the grain boundary diffusion coefficient, k is Boltzmann's constant, T is absolute temperature and A is a constant. The characteristic parameters of superplastic creep are a stress exponent of about 2, a grain size power dependence of about -2 and a value of about 200 for A.

The change in stress exponent from $n \cong 2$ at 625 - 636°C to $n \cong 5$ at 500 - 525°C suggests that the deformation mechanism changes from a superplastic mechanism to a dislocation climb-controlled mechanism as the stress increases or the temperature decreases. The change in creep

activation energy from about that for grain boundary diffusion at ≈631°C to about that for lattice diffusion at lower temperatures is consistent with this interpretation.

The creep data in Table 5.1 were analyzed in terms of two mechanisms operating independently so that the strain rates at a given stress for the two mechanisms are additive. The superplastic mechanism was described by Eq. (5-7) and the dislocation climb controlled mechanism was described by:

$$\frac{\dot{\gamma}\, k\, T}{D_L\, G\, b} = B \left(\frac{\tau}{G}\right)^5 \qquad (5\text{-}8)$$

where B is a constant and the proper diffusion coefficient is that for lattice diffusion. The creep rate for the sum of both mechanisms is then given as:

$$\frac{\dot{\gamma}\, k\, T}{G\, b} = A' D_B \left(\frac{\tau}{G}\right)^2 + B D_L \left(\frac{\tau}{G}\right)^5 \qquad (5\text{-}9)$$

where

$$A' = A \left(\frac{b}{d}\right)^2$$

The constants A' and B in Eq. (5-9) were evaluated by a method in which the least squares error E was minimized:

$$E = \sum_i \left\{\log \left(\frac{\dot{\gamma}\, k\, T}{G\, b}\right) - \log \left[A' D_B \left(\frac{\tau}{G}\right)^2 + B D_L \left(\frac{\tau}{G}\right)^5\right]\right\}^2 \qquad (5\text{-}10)$$

where i is an index for each data point in Table 5.1. Creep parameters used to evaluate Eq. (5-10) are summarized in Table 5.4. Successive iterations of Eq. (5-10) were performed with various values of A' and B, and it was found that the function E converged to a minimum at the following constant values:

$$A' = 1.51 \times 10^{-5}$$
$$B = 1.93 \times 10^{11}$$

Table 5.4

SUMMARY OF CREEP PARAMETERS

T, °C	T_m, K	T/T_m	D_B, cm^2/s	D_L, cm^2/s	E, 10^6 psi
500	1863	0.415	3.1E-12*	1.53E-21	15.5
525	1822	0.438	1.2E-11	2.1E-20	15.0
550	1780	0.462	4.6E-11	2.6E-19	14.4
575	1739	0.488	1.62E-10	2.8E-18	13.8
600	1697	0.514	5.1E-10	2.5E-17	13.1
625	1656	0.542	1.55E-9	1.96E-16	12.15
636	1616	0.563	3.2E-9	9.0E-16	11.9

* 3.1E-12 is a compact notation for 3.1×10^{-12}

Thus, the constant A in the superplastic creep expression, Eq. (5-7), has the value 485.

With the constants A' and B determined, Eqs. (5-7) and (5-8) are plotted in Fig. 5.19 and compared to the creep data. Since the ordinate scale in Fig. 5.19 uses the grain boundary diffusion coefficient, Eq. (5-8) was plotted in the form:

$$\frac{\dot{\gamma}\, k\, T}{D_B\, G\, b} = \left(B \frac{D_L}{D_B}\right) \left(\frac{\tau}{G}\right)^5$$

Because D_L/D_B varies with temperature, Eq. (5-8) is described by a different line at each temperature in Fig. 5.19.

For comparison, data of Vaidya et al. (1972) for Zn-22Al and data of Avery and Backofen (1965) for Sn-38Pb [analyzed by Bird et al. (1969)] are shown as dashed lines in Fig. 5.19. To be consistent, grain size was taken as the average grain diameter d, related to the mean linear intercept L by d = 1.7 L [Gifkins (1970)]. Data for Zn-22Al (d = 1.2 μm) and Sn-38Pb (d = 4.2 μm) alloys were chosen for the grain diameter

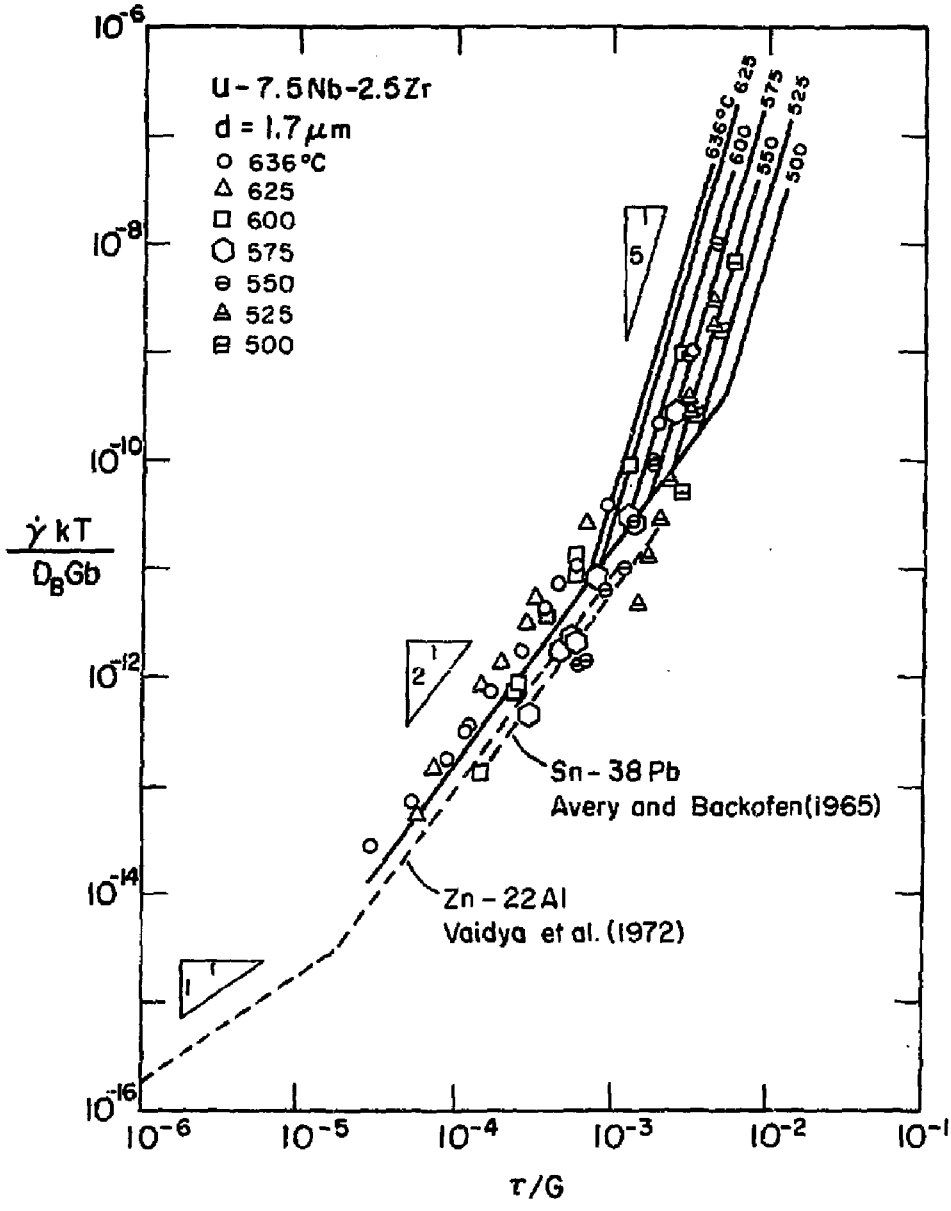

Fig. 5.19. Creep data for the fine-grain equiaxed $\alpha + \gamma_1$ structure are plotted in terms of diffusion-compensated strain rate and modulus-compensated stress. The solid lines represent the best-fit of the data for the case where superplastic and dislocation climb-controlled mechanisms operate independently. The creep data for Zn-22Al and Sn-38Pb have been adjusted slightly to a grain diameter of 1.7 μm for comparison with the U-7.5Nb-2.5Zr alloy.

nearest the 1.7 μm value used in the U-7.5Nb-2.5Zr alloy and the creep rates for the Zn-22Al and Sn-38Pb alloys were adjusted slightly (assuming a d^{-2} grain size dependence) to that expected for a 1.7 μm grain diameter.

The U-7.5Nb-2.5Zr data in the n = 2 region in Fig. 5.19 (especially data at 625 and 636°C) are in general agreement with the data for Zn-22Al and Sn-38Pb. The constant A = 485 in Eq. (5-7) is reasonable close to values of A calculated for other superplastic systems: A = 115 for a Sn-38Pb alloy [Avery and Backofen (1965)]; A = 53 for a Zn-22Al alloy [Ball and Hutchinson (1969] and A = 302 for a Zn-22Al alloy [Vaidya et al. (1972)]. Values of A were calculated for the data of Avery and Backofen (1965) and Ball and Hutchison (1969) by Bird et al. (1969). Since a stress exponent of ≈2 is directly apparent in the superplastic region for the U-7.5Nb-2.5Zr alloy, agreement of the constant A in Eq. (5-7) with data for other superplastic materials is indirect evidence that the grain size dependence is probably -2 power.

In Fig. 5.19, a transition from the n = 2 region to the n = 5 region occurs at a τ/G value of 10^{-3} to 2×10^{-3}. Very little data for other materials are available for stresses high enough to show a transition from n = 2 to n = 5 behavior for a structure with a 1.7 μm grain diameter. The data of Vaidya et al. (1972) for Zn-22Al suggest that the transition occurs at τ/G values of 10^{-3} to 2×10^{-3} for temperatures $0.5T_m$ to $0.6T_m$, which is consistent with our data.

In terms of the combined superplastic and dislocation climb-controlled creep mechanisms, the creep data for U-7.5Nb-2.5Zr are in general agreement with the n = 2 equation [Eq. (5-7)] at 625 - 636°C and in

general agreement with the n = 5 equation [Eq. (5-8)] at 500 - 525°C. Creep data at 550 - 600°C fall in the transition region centered at $\tau/G \cong 10^{-3}$. Appreciable deviation of the data from the best-fit creep equation, Eq. (5-9), indicates that the two creep mechanisms are perhaps not completely independent. Eq. (5-9) predicts a much sharper transition from n = 2 to n = 5 behavior than the data show.

Another region of creep was reported by Vaidya et al. (1972) at $\tau/G < 2 \times 10^{-5}$ where n = 1 behavior was observed. In this region the authors found general agreement with the Coble (1963) creep mechanism. In our investigation with the U-7.5Nb-2.5Zr alloy, stress levels were too high to observe n = 1 behavior.

There is a large amount of evidence in the literature that the dominant mechanism of superplastic deformation is grain boundary sliding and that at higher stresses a transition to a dislocation slip and climb mechanism occurs. Grain boundary sliding, so called Rachinger sliding [Cannon (1972) and Cannon and Nix (1973)] where grains remain equiaxed and change neighbors during deformation, has been observed directly during superplastic flow in the scanning electron microscope by Dingley (1970) and Geckinli (1973). No dislocation cell structure or dislocation pile-ups are observed after superplastic deformation [Hayden et al. (1967), Alden (1968), Lee (1969), Ball and Hutchison (1969) and Lee and Underwood (1970)]. In addition, few dislocations are observed, even when the specimen has been quenched under load [Lee (1969)]. This evidence, plus the fact that fine precipitate particles introduced within grains do not change the superplastic creep behavior, indicates that dislocation slip does not play an important role in superplastic deformation. Nicholson (1972) noted that the distribution of inert

markers was not disturbed after superplastic flow, except near grain boundaries.

Grain boundary sliding requires accommodation at grain corners to prevent void formation during deformation. The accommodation mechanism is likely to be the rate-controlling step in determining the specimen strain rate. Two possible accommodation mechanisms are dislocation slip and diffusional flow. Grain deformation and recovery models where dislocation pile-ups are expected, such as that of Ball and Hutchison (1969), are not consistent with experimental observations of the absence of dislocation activity. However, as discussed by Lee (1969), pile-ups at grain boundaries could be largely eliminated because of the dislocation attraction and efficient sink characteristics of a sliding boundary. Dislocation are probably attracted to a sliding boundary as they are to a free surface. Slip generated due to stress concentrations at triple points during grain boundary sliding is possible, but, as pointed out by Gifkins (1967), boundary migration should rapidly blunt the sharp corner and the stress concentration would be greatly reduced. Microstructural observations do not show sharp triple points in superplastic grains; grain boundaries are curved with rounded corners. In addition, the dispersion particles introduced by Nicholson (1972) and Geckinli (1973) suggest that slip accommodation, if operative, should be affected, but no difference in creep behavior was observed. Also, slip lines are not observed during superplastic flow [Ball and Hutchison (1969), Dingley (1970) and Geckinli (1973)].

One possible sliding mechanism involving crystallographic slip is that due to combined slip and climb of grain boundary dislocations

[Ishida and Brown (1967), Ashby (1969), Alden (1969), Langdon (1970) and McLean (1971)]. These dislocations could be generated within grain boundaries or, perhaps more likely, enter the boundary region by slip [Lin and McLean (1968)]. This mechanism does not require dislocation pile-ups. Alden (1969) and Langdon (1970) have developed models of the form

$$\dot{\varepsilon} \propto \frac{D\,\sigma^2}{d}$$

for climb-glide of a distribution of dislocations along the boundary. Alden and Langdon associated the diffusion coefficient D with grain boundary diffusion and lattice diffusion, respectively. This equation is quite close to the phenomenological equation for superplastic flow, Eq. (5-7).

Accommodation due to grain boundary migration by a diffusional flow mechanism and grain rotation is consistent with the experimental observations of the absence of dislocation activity within grains and the curved, bulbous grain boundary morphology. Several theories of grain boundary shear [Alden (1969) and Raj and Ashby (1971)] suggest that the mechanism is controlled by the rate of diffusion around bumps or rumples in the boundary. For a three-dimensional polycrystal, as pointed out by Gifkins (1967) and Geckinli (1973), diffusion across grain corners is expected to be the limiting step in the rate of grain boundary sliding accommodated by diffusional flow. The models of Gifkins and Geckinli, however, predict a one-power stress exponent in contrast to $n = 2$ observed for superplastic flow. Nicholson's (1972) marker experiments, where evidence for undeformed grain "cores" and denuded zones at randomly oriented boundaries is reported, support the grain boundary

sliding accommodated by diffusional flow model.

Evidence for a stress exponent of 2 has been reported by Ahlquist and Menezes (1971) for sliding in bicrystals and Matlock (1972) estimated the stress exponent for grain boundary sliding n_{gbs} as $n_c - 1$ where n_c is the stress exponent for creep. These results are not directly applicable to fine-grain superplastic structures deforming by Rachinger sliding; however, it is conceivable that local stress concentrations during grain boundary sliding in superplastic materials could lead to the observed stress exponent ($n = 2$).

Experimental evidence that a transition from a grain boundary sliding mechanism (stress exponent $n = 2$) to a slip-recovery mechanism ($n = 5$) occurs at high stresses is based on microstructural and texture observations. This transition was correlated with dislocation cell formation and increased dislocation density by Ball and Hutchison (1969), Lee (1969), Alden (1968) and Lee and Underwood (1970). A decrease in grain boundary sliding and rotation and elongation of grains was also observed [Alden (1967), Holt (1968), Lee (1969, 1970) and Ball and Hutchison (1969)]. In addition, sharp boundary contours are observed, Fig. 5.8, in contrast to smooth curved boundaries, Fig. 5.7.

The results of Chaudhari (1967), Packer et al. (1968), Johnson et al. (1968), Naziri and Pearce (1970), Lee (1971), Dunlop and Taplin (1971) and Cutler and Edington (1971) agree with the results of the present investigation where initially textured material becomes less textured (or originally random grain orientations do not become textured) during superplastic flow. Grain rotation and minimal slip deformation in the superplastic region most likely led to this observation. Lee

(1971), Dunlop and Taplin (1971) and Nuttall (1972) also noted that preferred orientation developed after deforming at high stresses in the non-superplastic region. Packer et al. (1968) and Johnson et al. (1968), however, observed a specimen shape change from circular to elliptical cross sections during superplastic flow of Zn-22Al and Zn-5Al alloys prepared by hot working (initially textured material). In agreement with Lee (1971), structures with randomly oriented grains prepared by quenching to 0°C showed no shape change during superplastic flow. This evidence would suggest that dislocation slip does play a role in superplastic deformation. Another possibility is that grain boundary sliding is highly anisotropic in the Zn-Al system. Anisotropic sliding rates were observed in Zn bicrystals by Horton and Beevers (1968). Grain boundary sliding anisotropy has also been reported recently by Raj and Ashby (1972) and predicted by McLean (1971) using a sliding model whereby dislocations travel along grain boundaries.

Conclusions

The U-7.5Nb-2.5Zr alloy, prepared as an equiaxed two-phase structure with stable grain diameter of 1.7 μm, was superplastic only at temperatures immediately below the monotectoid temperature (≈637°C or $0.56T_m$). Specimen elongations to about 550 pct were achieved at 635°C and strain rates of about 1×10^{-4}/s. Superplastic creep (625 - 636°C) was described by the phenomenological equation,

$$\frac{\dot{\gamma}\, k\, T}{D_B\, G\, b} = 485 \left(\frac{b}{d}\right)^2 \left(\frac{\tau}{G}\right)^2$$

for which general agreement with data of other superplastic materials is reported.

At high stresses where $\tau/G > 10^{-3}$ there was a transition from superplastic creep to dislocation climb-controlled creep where the stress exponent is 5. Creep data at 550 - 600°C were in this transition range centered at $\tau/G \cong 10^{-3}$, while data at 500 - 525°C exhibited only five-power creep.

Because the composition of the γ_1 phase changed significantly in the range 500 - 636°C and because the diffusion coefficient is sensitive to the Nb and Zr content, the diffusion coefficient in the γ_1 phase was strongly temperature-sensitive. An apparent activation energy for lattice diffusion at equilibrium γ_1 composition was calculated to be 130 kcal/mole between 625 and 500°C. This value compares favorably with an average value of 123 kcal/mole calculated from creep data at 513 - 613°C. Therefore, in the dislocation climb region and the transition region, creep is believed to be controlled by lattice diffusion. The creep activation energy at 631°C was about 60 kcal/mole, which was related to grain boundary diffusion and is consistent with superplastic creep behavior.

Grain boundary sliding with accommodation at grain corners is the mechanism most consistent with experimental observations for superplastic flow. An observed decrease in fiber texture during superplastic flow is most likely due to grain rotation and the relatively minor contribution of dislocation slip compared to the slip-recovery or dislocation climb-controlled creep mechanism. The accommodation mechanism is probably largely diffusion-controlled grain boundary migration, although no theory has been developed for this mechanism which agrees with observed creep behavior.

CHAPTER VI

DEFORMATION IN THE SINGLE-PHASE REGION FROM 670 TO 1000°C

Samples annealed to achieve a 40 μm grain size in the γ phase were deformed in compression within the temperature range 670 - 1000°C. Creep properties were analyzed at two strains: $\varepsilon = 0.01$ and $\varepsilon = 0.20$. The creep results are correlated with microstructures and discussed in terms of the viscous glide creep mechanism, grain boundary sliding and recrystallization during creep.

Results

Compression Tests

Prior to testing, each specimen was annealed at 1000°C for 1 h, producing an equiaxed grain structure with a 40 μm mean linear intercept between boundaries. Stress-strain curves showed a decrease in flow stress with strain, except at flow stresses below approximately 1600 psi. The results for samples deformed at $\dot{\varepsilon} \cong 10^{-5}$/s are shown in Fig. 6.1. Strain softening is evident at 670 and 800°C whereas at 900°C the flow stress is constant with strain and at 1000°C hardening is observed. At higher strain rates ($\dot{\varepsilon} \geq 10^{-4}$/s) specimens at all temperatures showed strain softening, but the softening rate was never greater than a 20 pct reduction in flow stress in a strain interval $\Delta\varepsilon = 0.10$. The softening rate decreased with increasing strain rate. The maximum strain softening effect was at 670°C and $\dot{\varepsilon} \cong 10^{-5}$/s, where the flow stress decreased by a factor of one-half in the first 20 pct strain.

To obtain more information on the nature of the large strain softening observed at 670°C and $\dot{\varepsilon} \cong 10^{-5}$/s, a test was performed in which

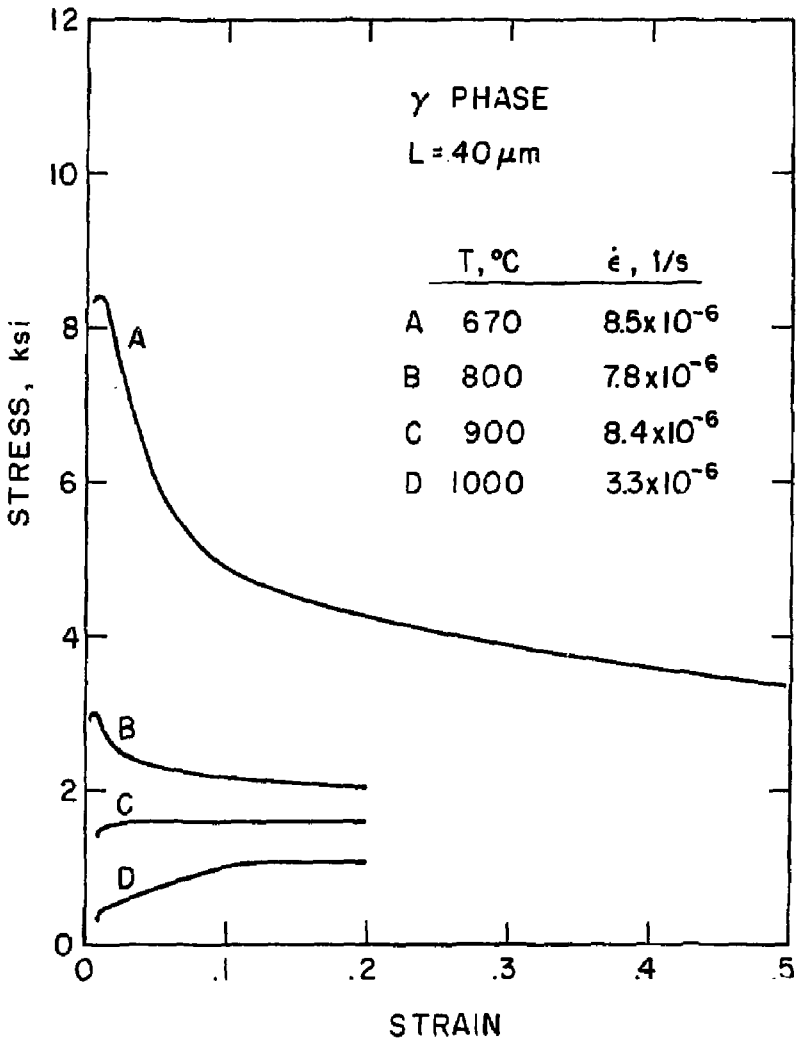

Fig. 6.1. Stress-strain curves obtained in compression for the U-7.5Nb-2.5Zr alloy previously annealed at 1000°C for 1 h to obtain a 40 μm grain size.

a sample was strained about 20 pct, unloaded and reannealed at 1000°C for 1 h and retested. It was found, Fig. 6.2, that the initial maximum stress after reannealing was about the same as that observed in the first strain interval and that strain softening occurred again. The flow stress did not decrease as much in the second strain interval as the first. This difference could be related to the presence of a triaxial stress state in the compression specimen at large strains ($\varepsilon > 0.5$) which would increase the flow stress. A macrophotograph of a longitudinal section of a compression cylinder deformed to $\varepsilon = 0.66$ at 670°C, Fig. 6.3, shows an inhomogeneous structure with what appears as thick and dark grain boundaries evident in most of the section except in the "dead" zones near the top and bottom of the specimen. Structural changes during deformation (discussed in the next section) probably accentuate the triaxial stress state. After deformation shown in Fig. 6.2, the specimen showed a variable grain size ranging from 50 μm at the center to 79 μm at the corners of a longitudinal section.

Because non-steady state deformation behavior was observed, creep properties were measured at constant strain for the two values: $\varepsilon = 0.01$ and $\varepsilon = 0.20$. These tests consisted of rapid changes in crosshead speed at essentially constant strain, starting at $\dot{\varepsilon} \cong 10^{-5}$/s and increasing strain rate by a factor of about 10 each time. The maximum stress at each strain rate was recorded and the crosshead speed was changed before strain softening occurred. For the data at $\varepsilon = 0.20$, the initial 20 pct strain was introduced at the lowest rate ($\dot{\varepsilon} \cong 10^{-5}$/s).

Because of difficulties in exactly compensating for machine deflection, strain measurements using the Instron machine without an extensometer

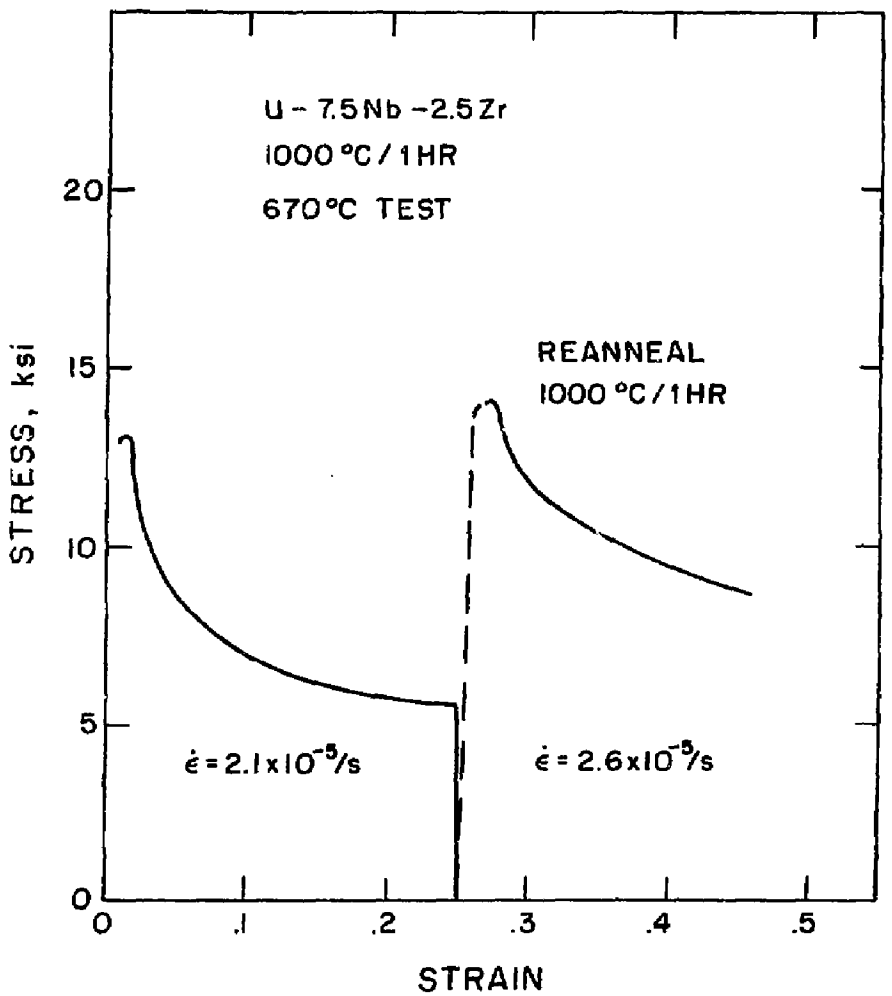

Fig. 6.2. A second anneal at 1000°C for 1 h after the first strain interval produces the initial maximum stress and strain softening in the second strain interval.

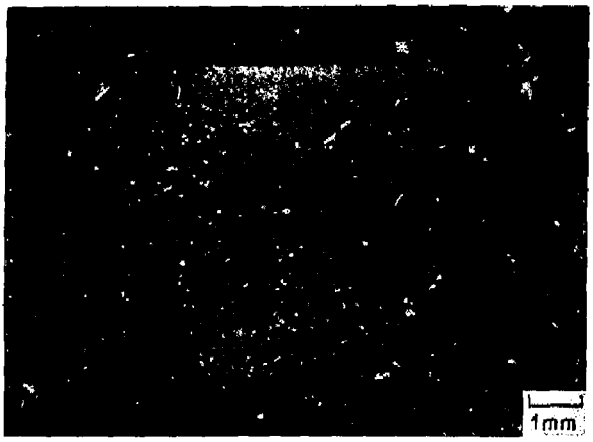

Fig. 6.3. Macrophotograph of sectioned compression specimen (the compression axis is vertical) deformed to $\varepsilon = 0.66$ at 670°C. Inhomogeneous structure is apparent with most of the observed structural changes which occurred during deformation contained in the dark region. The "dead zones" are the light regions at the top and bottom of the section.

were only accurate to ± 0.01. For creep data obtained during initial straining, the maximum strain at each crosshead speed was determined to be less than $\varepsilon = 0.013$. This value was obtained by measuring the length of a specimen deformed at 670°C and $\dot{\varepsilon} \cong 10^{-5}$/s to a strain slightly greater than that at which softening could be detected. Therefore, it is estimated that the plastic strain was about $\varepsilon = 0.01$ for the creep data obtained under initial loading. Since no strain softening occurred during deformation at each crosshead speed, the data at $\varepsilon = 0.01$ are considered to represent a constant structure condition.

All creep data at $\varepsilon = 0.01$ and $\varepsilon = 0.20$ were determined by the rapid change in crosshead speed technique except data for $\varepsilon = 0.20$ at 800, 900 and 1000°C. For these tests the strain softening rate was not great; typically, in a strain interval $\Delta\varepsilon \cong 0.07$ the flow stress softened about 5 pct. A correction for softening in previous strain intervals was made for these data using a forward extrapolation technique. The criterion used was that at each instantaneous crosshead speed change, the ratio of flow stresses at the two strain rates at constant strain should equal the ratio of corrected flow stresses for the same strain rates. This method assumes that the stress exponent for creep is constant during strain softening and that the strain softening rate is independent of strain rate. The first assumption is satisfied, as shown later in this chapter, and the second is approximately true for the data used where softening rates were not great. Let σ^*_i and $\Delta\sigma_i$ be the initial maximum stress and decrease in stress, respectively, in strain interval i at strain rate $\dot{\varepsilon}_i$. Then, according to the criterion, the stress corrected for strain softening, σ_i, can be calculated using:

$$\frac{\sigma_{i+1}}{\sigma_i} = \frac{\sigma^*_{i+1}}{\sigma^*_i - \Delta\sigma_i}$$

If α_i is the relative softening in strain interval i relative to the final (minimum) stress,

$$\alpha_i = \frac{\Delta\sigma_i}{\sigma^*_i - \Delta\sigma_i}$$

then

$$\sigma_{i+1} = \sigma^*_{i+1} (1 + \alpha_i) \frac{\sigma_i}{\sigma^*_i}$$

which is a recursion formula in which the flow stress σ_{i+1} is compensated for softening in the previous strain interval. If i = 1 is the first 20 pct strain at $\dot{\varepsilon}_1 = 10^{-5}$/s, i = 2 is the next strain interval at $\dot{\varepsilon}_2 = 10^{-4}$/s, etc., then the formulae used are:

$$\sigma_3 = \sigma^*_3 (1 + \alpha_2)$$

$$\sigma_4 = \sigma^*_4 (1 + \alpha_2) (1 + \alpha_3)$$

.

.

.

$$\sigma_{i+1} = \sigma^*_i (1 + \alpha_2) (1 + \alpha_3) \ldots (1 + \alpha_i)$$

where, as intended, no correction is made for softening during the first 20 pct strain ($\alpha_1 = 0$).

The strain rate-flow stress data determined at $\varepsilon = 0.01$ and $\varepsilon = 0.20$ are listed in Tables 6.1 and 6.2 and plotted in Figs. 6.4 and 6.5. At stresses less than about 10,000 psi, the data at each temperature exhibit a stress exponent very near to $n = 3$. To calculate activation energies for creep, Q, the following equation was assumed:

TABLE 6.1

CREEP DATA AT $\varepsilon = 0.01$

T, °C	σ, psi	$\dot{\varepsilon}$, 1/s
670	5360	2.9E-6*
	9500	7.5E-6
	8900	7.6E-6
	8400	7.5E-6
	8300	7.6E-6
	9790	1.9E-5
	12600	1.9E-5
	15500	1.8E-4
	26200	1.9E-3
700	6600	7.4E-6
	12400	7.6E-5
	19800	7.6E-4
	27900	7.8E-3
800	2940	8.4E-6
	5860	8.0E-5
	12800	8.7E-4
	20500	8.7E-3
900	2200	9.4E-6
	4310	9.5E-5
	7030	9.6E-4
	13500	1.0E-2
1000	850	1.0E-5
	2040	1.0E-4
	4420	1.0E-3
	8640	1.0E-2

* 2.9E-6 is a compact notation for 2.9×10^{-6}

TABLE 6.2

CREEP DATA AT $\varepsilon = 0.20$

T, °C	σ, psi	$\dot{\varepsilon}$, 1/s
670	4110	9.8E-6*
	6100	2.5E-5
	14100	2.5E-4
	20100	9.4E-4
	23900	2.5E-3
	27300	4.8E-3
	31900	2.7E-2
	34900	2.8E-2
800	2120	8.9E-6
	5310	9.3E-5
	12100	9.9E-4
	22200	1.1E-2
	28800	6.3E-2
900	1610	9.1E-6
	3510	9.3E-5
	8300	9.7E-4
	15900	1.0E-2
	23000	5.4E-2
1000	1070	3.6E-6
	1790	2.3E-5
	3820	2.5E-4
	8310	3.0E-3
	16700	3.2E-2

* 9.8E-6 is a compact notation for 9.8×10^{-6}

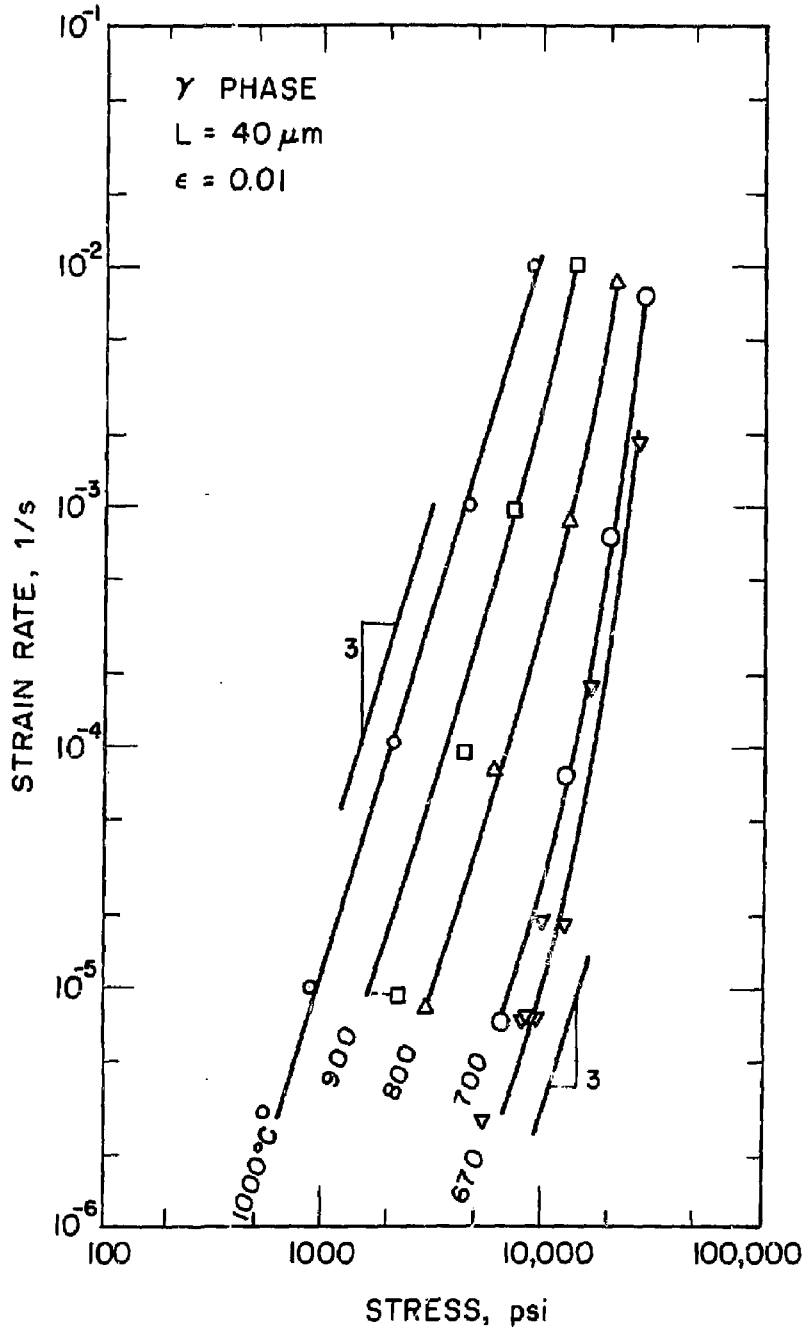

Fig. 6.4. Creep data obtained at $\varepsilon = 0.01$ show a stress exponent of three at stresses below about 10,000 psi.

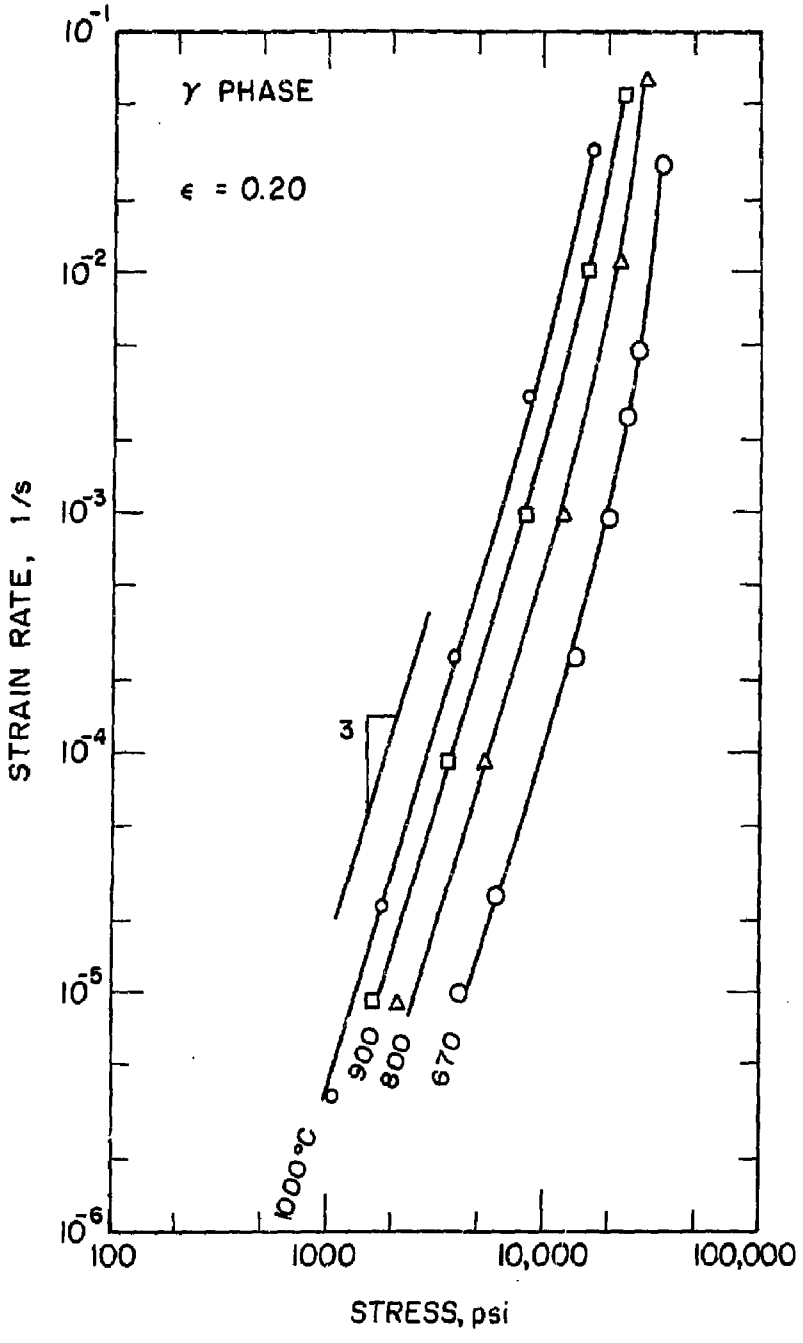

Fig. 6.5. Creep data obtained at $\varepsilon = 0.20$ also show a stress exponent of three at stresses below about 10,000 psi.

$$\dot{\varepsilon} = k \exp(-Q/RT) \ (\sigma/E)^n$$

The data at each temperature were fitted with lines at constant slope n = 3 (as shown in Figs. 6.4 and 6.5) and the creep activation energy was calculated at constant stress from the slope of a log $\dot{\varepsilon}$ vs. 1/T plot, Fig. 6.6. Because of lack of data, no correction for the variation of elastic modulus with temperature was made. There are some data at 700, 800 and 900°C from Bugrov et al. (1968, 1972), plotted in Fig. 5.6 (Chapter V), but the data are not consistent with the recent work of Armstrong et al. (1973b). Armstrong et al. found the elastic modulus for γ-U to be 3.3×10^6 psi, independent of temperature in the range 770 - 930°C. The data of Bugrov et al. (1972) show the modulus for U-6.8ONb-3.33Zr decreasing from 9.4×10^6 psi at 700°C to 2.0×10^6 psi at 900°C, which would not be expected if the alloying additions had a relatively minor effect. Also, their value at 900°C appears too low compared to data for γ-U. A rough estimate of the modulus for U-7.5Nb-2.5Zr can be obtained by assuming a linear modulus variation with composition (at. fraction) in the ternary diagram. Using data at 700 - 1000°C for γ-U [Armstrong et al. (1973b)], Nb [Armstrong and Brown (1965)] and β-Zr [Armstrong and Brown (1964)], the elastic modulus for U-7.5Nb-2.5Zr is calculated as 6.2×10^6 psi, independent of temperature (in this temperature range the modulus of Nb and Zr increase and decrease, respectively, with increasing temperature). For data correlations presented later in this chapter, the elastic modulus for U-7.5Nb-2.5Zr was assumed to be 6×10^6 psi in the 670 - 1000°C temperature range.

From Fig. 6.6, the activation energy for creep at $\varepsilon = 0.01$ is 51 kcal/mole. This value can be compared with activation energies for

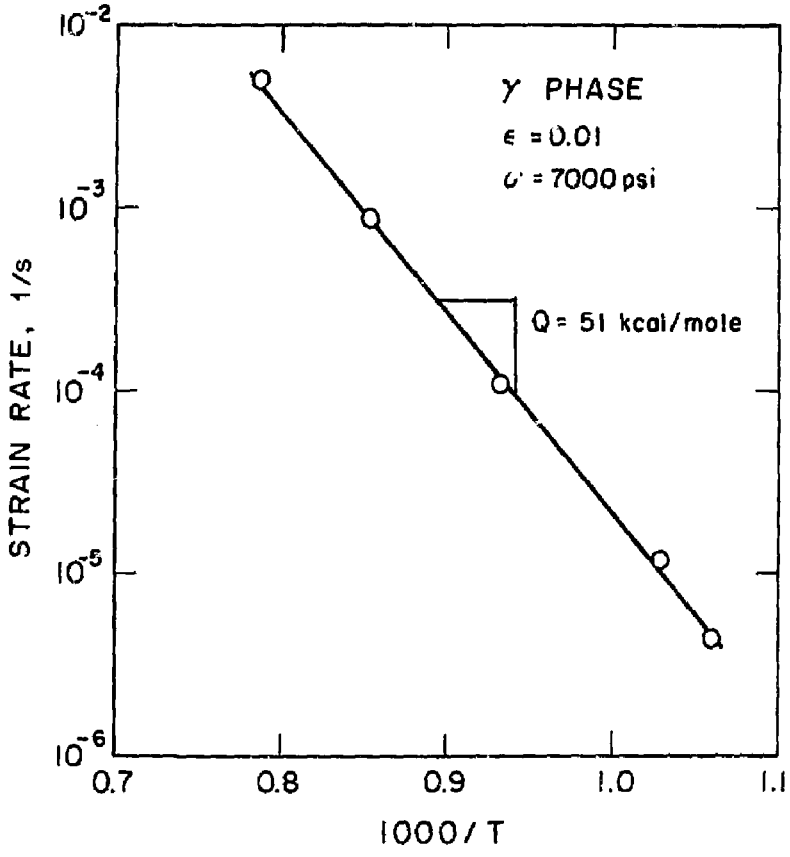

Fig. 6.6. The activation energy for the creep data at $\varepsilon = 0.01$ is 51 kcal/mole. No correction for the temperature variation of the elastic modulus was made.

lattice diffusion calculated from Weertman's (1968) average diffusion coefficient, Fig. 5.17 (Chapter V), which range from 59.7 kcal/mole at ≈685°C to 54.9 kcal/mole at ≈950°C. It appears that the creep activation energy is associated with lattice diffusion for deformation at $\varepsilon = 0.01$. As discussed later in this Chapter, an activation energy was not calculated for the data at $\varepsilon = 0.20$ because microstructure changed significantly with temperature.

Microstructure

Compression samples deformed in the γ phase region were unloaded and water-quenched within 60 s of unloading. During the unloaded period before quenching, the specimen remained close to test temperature inside the heavy metal compression cage. Quenching was rapid enough to preserve the γ phase (no transformation to $\alpha + \gamma_1$ was observed).

Structural changes occurring during the rapid strain softening at 670°C and $\dot{\varepsilon} \cong 10^{-5}$/s (Fig. 6.1) are shown in the optical micrographs in Figs. 6.7 and 6.8. In Fig. 6.7, after 1.3 pct plastic strain the originally straight grain boundaries of the annealed material are wavy from grain boundary migration. "Ghost" boundaries indicating the original boundary position can be seen in Fig. 6.7. After a strain $\varepsilon = 0.49$ substructure is well-developed within the grains, Fig. 6.8 (bottom photo). In the top photograph in Fig. 6.8 subgrain boundaries are not revealed as clearly by the etch as in the bottom photograph. In addition, many new small grains about 6 μm in size are present in the region of the original grain boundaries (Fig. 6.8, top photo). These small grains appear rather blurred (Fig. 6.8, top photo). The probable reason is that extensive grain boundary migration has occurred in these regions.

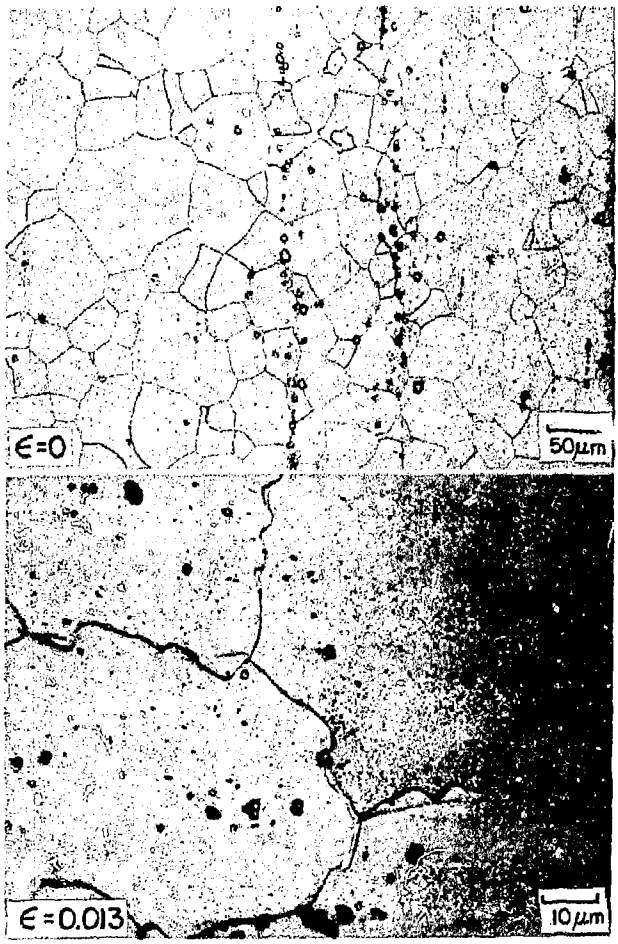

Fig. 6.7. Originally straight grain boundaries shown after annealing at 1000°C for 1 h to produce a 40 μm grain size (top photo, $\varepsilon = 0$) become rumpled after deformation to $\varepsilon = 0.013$ at 670°C and $\dot{\varepsilon} = 8 \times 10^{-6}$/s.

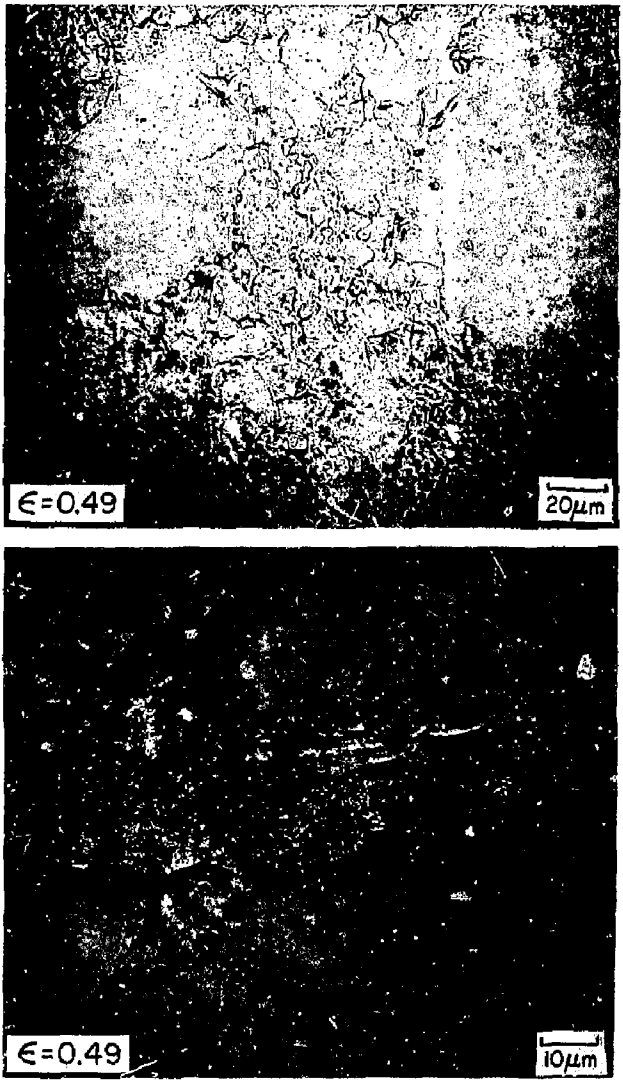

Fig. 6.8. After deformation to $\varepsilon = 0.49$ at 670°C and $\dot{\varepsilon} = 9 \times 10^{-6}/s$, many new small grains about 6 μm in size are present in the region of the original grain boundaries (especially evident in the top photo) and substructure is well-developed (bottom photo).

The bottom micrograph in Fig. 6.8 appears to contain about three original large grains (40 μm grain size) with a triple point near the center of the photograph. A network of subgrain boundaries is well-developed within the large grains. At the original grain boundaries, small grains (≈6 μm grain size) appear to be forming. Subgrain boundaries are not observed in these new grains and recrystallization during creep is thought to be the mechanism by which they were formed.

One specimen deformed at 670°C and $\dot{\epsilon} \cong 10^{-5}$/s to $\epsilon = 0.5$ was maintained under the final load of testing during the time that the furnace and atmosphere cover tube were removed and during the water quench. No difference in microstructure from that in Fig. 6.8 was detected. Thus the microstructures in Fig. 6.8 are probably representative of the deforming structure.

The formation of recrystallized grains was also apparent at other temperatures and strain rates. Fig. 6.9 shows microstructures at 670, 800 and 1000°C after deformation at $\dot{\epsilon} \cong 3 \times 10^{-2}$/s. Under these conditions, the recrystallized grain size ranged from about 1 μm at 670°C to about the original grain size (40 μm) at 1000°C. Considering the structures after deformation at 670°C at $\dot{\epsilon} \cong 10^{-5}$/s (Fig. 6.8) and $\dot{\epsilon} \cong 3 \times 10^{-2}$/s (Fig. 6.9), the recrystallized grain size decreases with increasing stress. The microstructures at 800°C and 1000°C are consistent with this observation, although temperature may also affect the recrystallization mechanism. The grains without substructure at 1000°C, Fig. 6.9, could have formed by recovery after unloading and before quenching. However, a recrystallization mechanism is preferred because recovery would not be expected to occur completely in one grain and very

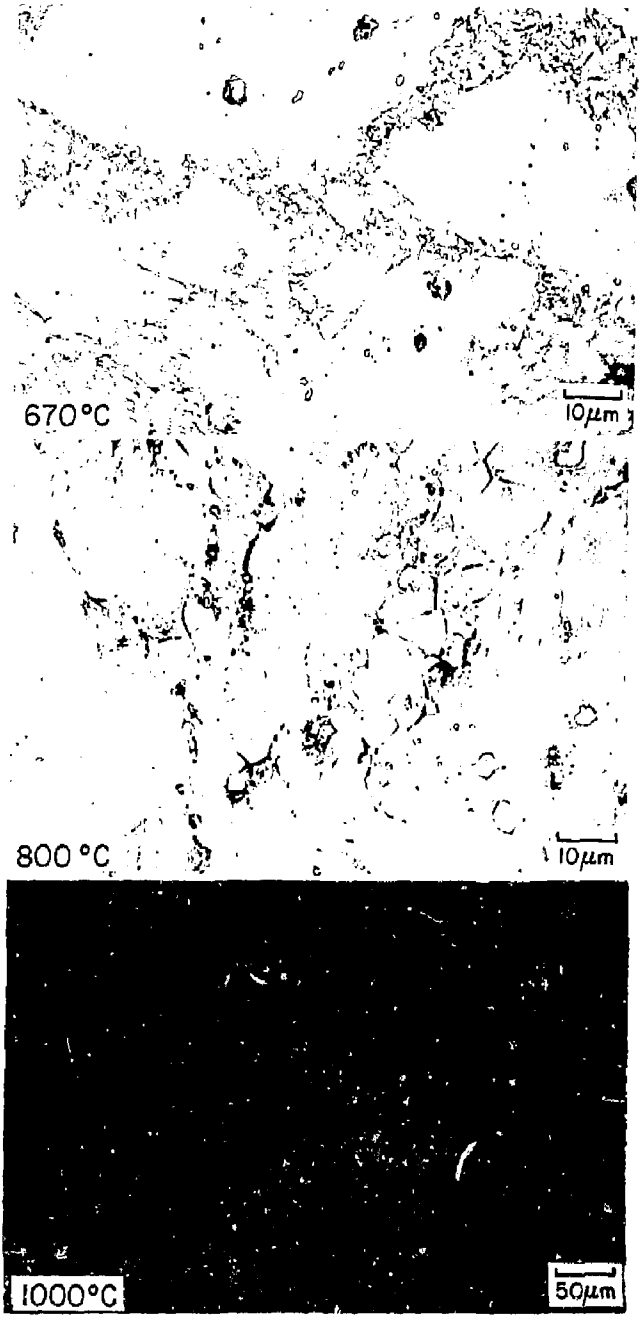

Fig. 6.9. Microstructures of specimens deformed at different temperatures at $\dot{\epsilon} \cong 2 \times 10^{-3}/s$ show that the recrystallized grain size ranges from about 1 μm at 670°C to about 40 μm at 1000°C.

little in an adjacent grain. Recrystallization could have occurred during the time at temperature after unloading and before quenching.

Micrographs such as the top photograph in Fig. 6.9 could be interpreted as evidence for precipitation of a second phase at grain boundaries. However, an electron microprobe scan across several polished (but unetched) sections of samples (such as the top photograph in Fig. 6.9) did not show any compositional variations. Thus we interpret this fine structure as a fine-grain region of the microstructure.

The dislocation substructure proved very difficult to reveal. Cathodic etching [Duran and Fisher (1971)] as well as various electrolytic solutions were tried, but the best results were obtained using the standard 2 pct oxalic acid electrolyte with an open circuit potential of about 1 volt. Attempts to thin foils for transmission electron microscopy did not prove successful.

Discussion

Viscous Glide Creep

The creep data obtained at $\dot{\epsilon} = 0.01$ show that at stresses less than about 10,000 psi the stress exponent is 3 and the activation energy for creep is about equal to that for lattice diffusion. This evidence suggests that the solid solution alloy is deforming by a viscous glide mechanism. Weertman (1960) has shown that alloy additions to several pure metals can lower the stress exponent from about 5 for the pure metal to about 3 for the solid solution alloy. Weertman interpreted the three-power behavior using a microcreep mechanism [Weertman (1957)] where dislocation glide is controlled by a Cottrell-Jaswon mechanism. Whereas Weertman's (1960) creep expression for this viscous glide mechanism indicated a

strain rate dependence on solute concentration and the fractional difference in size between solute and solvent atoms, Bird et al. (1969) presented a derivation independent of concentration and atom size difference for the case where all dislocations within a crystal drag Cottrell atmospheres. Their equation is:

$$\frac{\dot{\gamma}\, k\, T}{D_L\, G\, b} = A \left(\frac{\tau}{G}\right)^3 \qquad (6\text{-}1)$$

In Eq. (6-1) the constant A represents $2/\alpha^2$ where α is the constant in the expression

$$\tau = \alpha G\, b\, \sqrt{\rho} \qquad (6\text{-}2)$$

used in the derivation of Eq. (6-1). In Eq. (6-2), ρ is the dislocation density within a grain or subgrain. Eq. (6-2) has been experimentally verified for several metals, with $\alpha \cong 0.6$ [Bird et al. (1969)]; therefore, $A \cong 6$.

Sherby and Burke (1968) proposed that solid solution alloys deforming by a viscous glide mechanism ($n = 3$) be called Class I alloys and those deforming by a dislocation climb-controlled mechanism ($n = 5$) be called Class II alloys. Cannon and Sherby (1970) suggested that Class I and Class II alloys could be separated on a diagram based on volume size factor Ω_{sf} [King (1966)] and elastic modulus E at temperatures of creep deformation. Volume size factor is a measure of the difference in atom size for solute and solvent atoms and data for many binary systems are available in King's (1966) paper. In Fig. 6.10 the U-Nb binary system is plotted on the diagram from Cannon and Sherby (1970). No volume size factor data is available for the U-Zr binary system, so we assume that data for U-Nb approximate that for the U-7.5Nb-2.5Zr

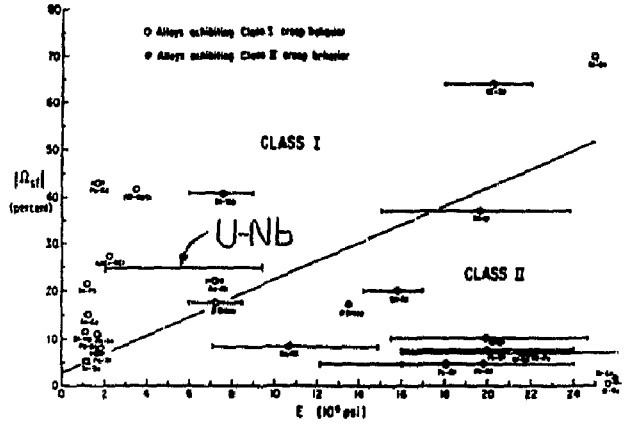

Fig. 6.10. The U-Nb alloy is predicted to be a Class I solid solution on the diagram by Cannon and Sherby (1970). The volume size factor is from King (1966) and the modulus range is from Bugrov et al. (1972).

alloy. The modulus range in Fig. 6.10 was taken from Bugrov et al. (1972) for the temperature range 700 - 900°C, although as discussed earlier in this chapter, the modulus range for 670 - 1000°C is probably a smaller range within the range plotted. According to Fig. 6.10, the U-7.5Nb-2.5Zr solid solution alloy is predicted to be a Class I alloy. This observation and the observed stress exponent of three strongly suggest that the deformation mechanism at $\varepsilon = 0.01$ is viscous glide.

The creep data for $\varepsilon = 0.01$ (Table 6.1) are plotted as $\dot{\gamma} \kappa T/(D_L G b)$ vs. τ/G in Fig. 6.11. Creep parameters used to calculate points in Fig. 6.11 are summarized in Table 6.3. The stress exponent is three with power law breakdown occurring at $\tau/G \cong 2 \times 10^{-3}$. In the three-power law region, a best-fit line gives a value of 11 for the constant A in Eq. (6-1). This value of A is in excellent agreement with the predicted value of 6 in Eq. (6-1). Since the creep properties of several Class I alloys have been shown to fit Eq. (6-1) [Bird et al. (1969) and Murty et al. (1972)], the U-7.5Nb-2.5Zr alloy probably deforms by the viscous glide mechanism during initial straining ($\varepsilon = 0.01$).

The viscous glide creep equation, Eq. (6-1) with A = 11, is compared in Fig. 6.11 with a possible superplastic creep equation for the 40 μm grain size (68 μm grain diameter) structure. The superplastic creep equation, determined in Chapter V, was plotted in Fig. 6.11 in the following form:

$$\frac{\dot{\gamma} k T}{D_L G b} = 485 \left(\frac{b}{d}\right)^2 \left(\frac{D_B}{D_L}\right) \left(\frac{\tau}{G}\right)^2 \qquad (6\text{-}3)$$

Because D_B/D_L is temperature dependent, Eq. (6-3) is plotted as a different line of slope two at each temperature. Only lines for Eq. (6-3) at the lowest and highest temperatures are plotted in Fig. 6.11.

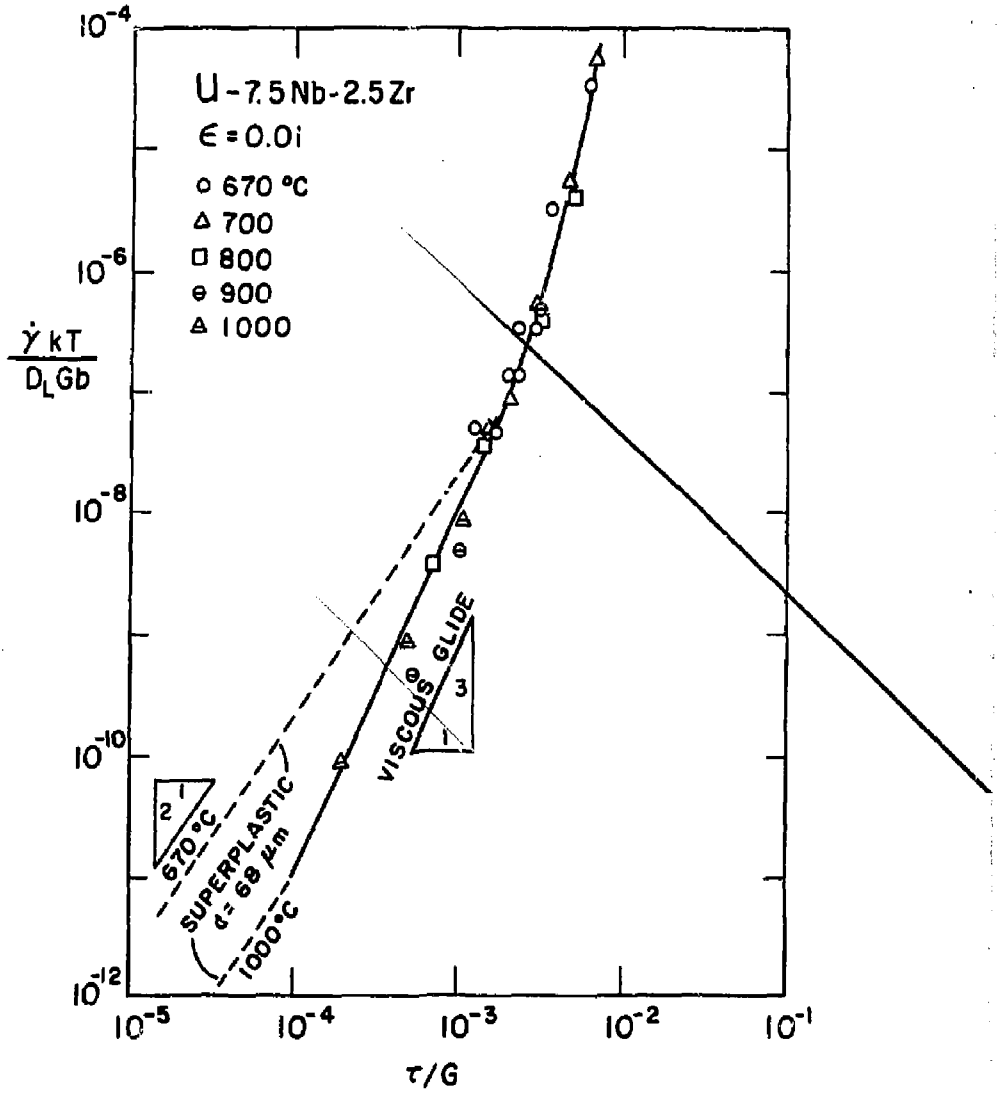

Fig. 6.11. Creep data obtained at ε = 0.01 are compared with the viscous glide creep equation(solid line) determined as a best-fit to the data at stresses below power-law breakdown where τ/G = 2×10^{-3}. A superplastic creep mechanism is expected to contribute negligibly to deformation in the stress range of the data.

The range of data in Fig. 6.11 clearly is contained within the viscous glide creep region, although data for the lowest stress at each temperature fall about at the transition point expected between superplastic and viscous glide creep mechanisms. Within the range of data in Fig. 6.11, the superplastic creep mechanism would be expected to contribute negligibly to the total strain rate compared to the viscous glide creep mechanism.

Another possible interpretation of the three power stress exponent could be as a transition from superplastic creep (n = 2) to dislocation slip-climb creep (n = 5). However, considering the wide range of temperature and stress for which a stress exponent $n \cong 3$ in Fig. 6.4, this type of analysis does not seem reasonable.

TABLE 6.3

SUMMARY OF CREEP PARAMETERS

T, °C	D_L, cm^2/s	T/T_m	D_B, cm^2/s
670	3.0E-15*	0.584	6.5E-9
700	7.9E-15	0.602	1.16E-8
800	1.35E-13	0.664	6.4E-8
900	1.33E-12	0.726	2.6E-7
1000	8.4E-12	0.788	8.6E-7

* 3.0E-15 is a compact notation for 3.0×10^{-15}

Another possible creep mechanism with a three-power stress dependence is that developed by Nabarro (1967) in which strain is produced by dislocation climb alone. If this mechanism is controlling deformation, then the creep equation is Eq. (6-1) where the constant A is given by

$$A = \frac{1}{\pi \ln\left(\frac{4}{\pi}\frac{G}{\tau}\right)}$$

Considering the range in τ/G for the data in Fig. 6.4 in the three-power law region, the Nabarro (1967) creep mechanism predicts the constant A to be in the range 0.048 to 0.035. Although the Nabarro (1967) creep equation is the same form as that for the viscous glide mechanism, it predicts creep rates which are about 200 times slower than observed. Weertman (1968) derived a creep equation for Nabarro's model which predicts strain rates about one order of magnitude faster than Nabarro's (1967) equation, but this still does not fit the data.

A final creep mechanism with a three-power stress dependence is the Nabarro subgrain model [Weertman (1968)] in which strain is produced by a diffusion creep mechanism within subgrains. The creep equation for the Nabarro subgrain model is also given by Eq. (6-1), but the constant A is about equal to the A value for the Nabarro (1967) climb mechanism [Weertman (1972) and Murty et al. (1972)]. Therefore, the Nabarro subgrain model also predicts strain rates lower than observed for the U-7.5Nb-2.5Zr alloy. Clearly, the viscous glide creep model is in better agreement than Nabarro's climb model or the Nabarro subgrain model for creep of the U-7.5Nb-2.5Zr alloy at low strains ($\varepsilon = 0.01$).

The creep data for $\varepsilon = 0.01$, Fig. 6.11, show that the strain rate is faster than a three-power law creep equation would predict at high stresses. Power law breakdown occurs at a stress where $\tau/G \cong 2 \times 10^{-3}$. In terms of strain rate compensated for temperature with the diffusion coefficient, $\dot{\varepsilon}/D$, power law breakdown is found to occur at about $\dot{\varepsilon}/D = 10^{9}$.

There is a large amount of evidence that deviation at high stresses from five-power law behavior for pure metals occurs at $\dot{\varepsilon}/D \cong 10^{9}$ where $\tau/G \cong 7 \times 10^{-4}$ [Sherby and Burke (1968)], but to our knowledge the only reported data showing power law breakdown at high stresses for materials deforming by a viscous glide mechanism are from Weertman (1960). In Weertman's (1960) paper, deviation from a three-power law for In-Pb, In-Cd, In-Tl, In-Sn and Pb-Sn alloys occurred at $\sigma \cong 300$ psi where the In-rich alloys were tested at ~320 K and the Pb-rich alloy at ~450 K. Estimating the elastic modulus for these alloys at $E \cong 1.5 \times 10^{6}$ psi, the data in Weertman's paper indicate that power law breakdown occurs at $\tau/G \cong 3 \times 10^{-4}$. Other data in the literature for viscous glide deformation at high stresses do not show power law breakdown: Al-5.5Mg tested to $\tau/G = 2 \times 10^{-3}$ [Horiuchi et al. (1965)]; Ni-54Al tested to $\tau/G = 2 \times 10^{-3}$ [Vandervoort et al. (1966)]; Ag_2Al tested to $\tau/G = 1.3 \times 10^{-3}$ [Howard et al. (1963)]; Al-3.3Mg tested to $\tau/G = 1 \times 10^{-3}$ [Horiuchi et al. (1965)]; and Al-3Mg tested to $\tau/G = 1 \times 10^{-3}$ [Murty et al. (1972)].

Our results and that of Weertman (1960) indicate that power law breakdown does occur at high stresses for materials deforming by viscous glide; however, our data and other data for Al-Mg, Ni-Al and Ag_2Al suggest that the stress for power law breakdown is greater for the viscous glide creep mechanism than dislocation climb-controlled creep.

The probable cause of power law breakdown is excess vacancy generation at high stresses leading to enhanced diffusion coefficients [Weertman (1957) and Armstrong et al. (1973a)]. Excess vacancies would be expected to affect viscous glide creep because dislocation climb must still take place, even though it is not rate-controlling. Enhanced atom diffusion could

also increase the glide rate for dislocations dragging Cottrell atmosphere.

Another explanation of power law breakdown in a viscous glide creep model is that at high stresses dislocations can be torn from a dragging solute atmosphere [Weertman (1968, 1972)]. This analysis could account for the varying values of τ/G for power law breakdown in viscous glide creep, for the power law breakdown stress could then vary with the alloy system.

Deformation Behavior at Large Strains

The $\log \dot{\varepsilon}$ vs. $\log \sigma$ curves obtained at a constant strain $\varepsilon = 0.20$ are shown in Fig. 6.5. At each temperature the test should be representative of a constant structure condition, with the structure determined by near steady-state deformation at $\dot{\varepsilon} \cong 10^{-5}$/s. As shown in Fig. 6.1, a constant flow stress with strain was observed at $\varepsilon = 0.20$ for tests at 800, 900 and 1000°C at $\dot{\varepsilon} \cong 10^{-5}$/s, indicating steady state deformation behavior. The flow stress at 670°C, however, was still decreasing at $\varepsilon = 0.20$.

A comparison of Figs. 6.4 and 6.5 show that (at stress below ~10,000 psi) the stress exponent is about three in each case. This similarity of stress exponents suggests that the viscous glide creep mechanism is probably controlling deformation at constant microstructure at $\varepsilon = 0.20$.

A comparison of Figs. 6.4 and 6.5 also shows that at $\varepsilon = 0.20$ the material strengthened at 900 and 1000°C and weakened at 670 and 800°C compared to data at $\varepsilon = 0.01$. These changes are a reflection of the behavior occurring during the 20 pct strain interval, Fig. 6.1. The

observed strengthening and weakening can be related to microstructural changes.

During deformation at 670°C at $\dot{\varepsilon} \cong 10^{-5}$/s, the micrographs show that small grains were formed at grain boundaries. These grains could form by a grain boundary migration process [Richardson et al. (1966)], subgrain boundary migration and coalesence [Exell and Warrington (1972)] or other recrystallization processes. Since the new grains were formed at grain boundary locations, sliding at grain boundaries could have influenced the formation of the new grains. The observed wavy grain boundaries at $\varepsilon = 0.013$, Fig. 6.7, could have formed by the grain boundary sliding and migration mechanism suggested by Walter and Cline (1968), Fig. 6.12. Once an originally straight grain boundary is perturbed due to slip in the grains or the formation of a subgrain boundary intersecting the grain boundary, sliding causes shear zones to form in the adjacent grains because the grain boundary is slightly curved. The increased strain energy in the shear zones provides a driving force for grain boundary migration. Further sliding with migration leads to a rumpled boundary surface. Once bulging of the grain boundary reaches a hemispherical shape, continued sliding and migration would produce a new grain. The micrographs at 670°C are in general agreement with this model. Subgrain boundary structure is most developed near grain boundaries where shear zones during sliding would concentrate dislocation generation. Also, the distance between grain boundary bulges (Fig. 6.7) is approximately equal to the size of the nucleated grains (Fig. 6.8).

The structure of the specimen deformed at 670°C and $\dot{\varepsilon} \cong 10^{-5}$/s to $\varepsilon = 0.20$ consists of a 40 μm grain size structure wherein the grain

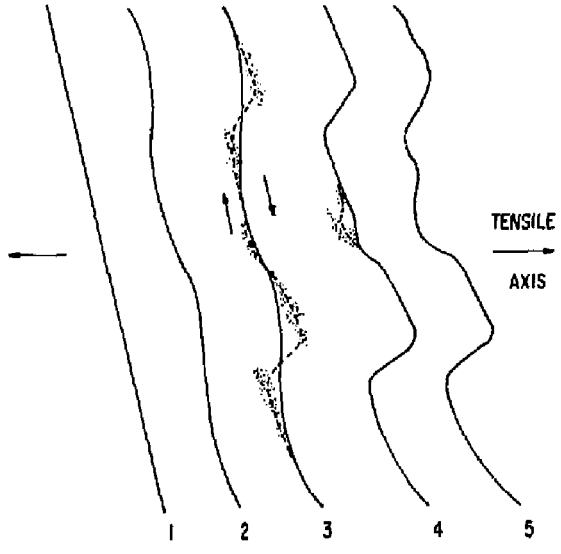

Fig. 6.12. The grain boundary sliding and migration process of Walter and Cline (1968) causes an originally smooth grain boundary to become rumpled. Once a boundary becomes slightly curved, shear zones formed during sliding provide a driving force for grain boundary migration, leading to a rumpled surface.

boundaries are replaced by a thick web of fine-grain structure. This web of fine-grain structure thickens with strain where, at $\varepsilon = 0.49$, the fine-grain structure constitutes over one-half of the total volume, Fig. 6.13.

A decrease in grain size is probably the cause of strain softening at 670°C. No other mechanism could account for the observed softening where the flow stress continues to decrease with strain at $\varepsilon = 0.49$. Material weakening during creep of Class I alloys showing an inverted primary only occurs at $\varepsilon<0.05$ [Bird et al. (1969) and Horiuchi and Otsuka (1972)]. As analyzed by Matlock (1972), a decrease in grain size leads to an increase in strain rate at constant stress because of the increased contribution of grain boundary sliding in the deformation process. The compression test at 670°C and $\dot{\varepsilon} \cong 10^{-5}/s$ in which annealing after strain softening increased the flow stress to its original maximum value, Fig. 6.2, is consistent with the grain size increase during annealing.

The heterogeneous grain size distribution at 670°C is difficult to analyze, but the stress exponent $n \cong 3$ at $\varepsilon = 0.20$ suggests that a viscous glide creep mechanism is controlling the deformation rather than Rachinger sliding as in a superplastic mechanism ($n = 2$). The fine-grain structure at the grain boundaries of the original homogeneous 40 μm grain size material is a weak structure compared to the large 30 - 40 μm grains. Specimens weaken with strain because the volume fraction of fine-grain structure increases with strain. However, because of the presence of the large 30 - 40 μm grains, deformation of the large grains apparently must accompany the Rachinger sliding mechanism expected to

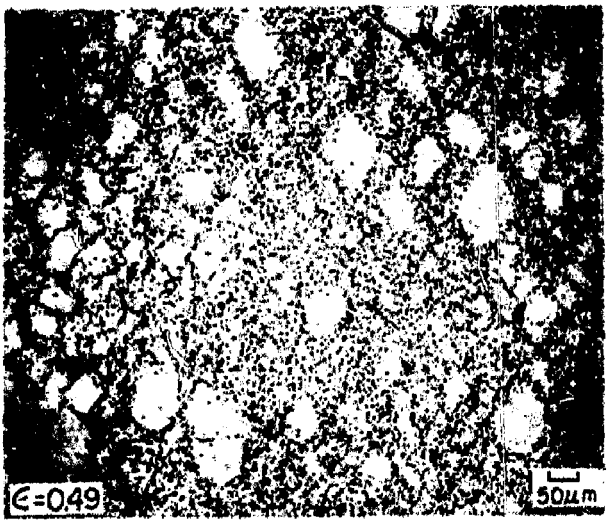

Fig. 6.13. A low-magnification micrograph after deformation to $\epsilon = 0.49$ at 670°C and $\dot{\epsilon} = 9 \times 10^{-6}$/s shows that the fine-grain structure constitutes over one-half of the total volume.

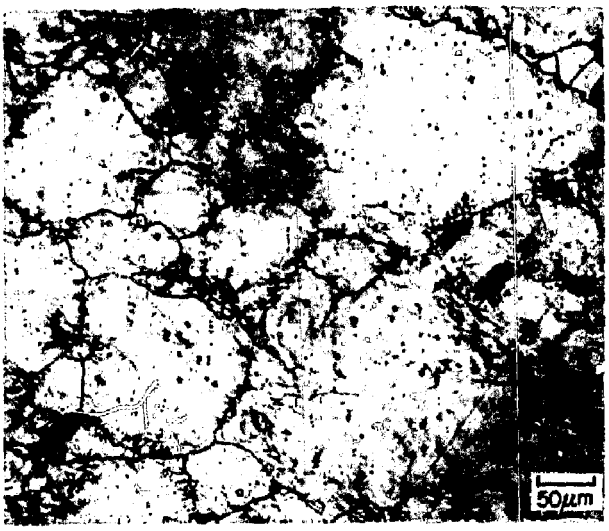

Fig. 6.14. A region in the "dead zone" at the top or bottom of a compression specimen after deformation to $\epsilon = 0.67$ at 1000°C. After 20 pct strain at $\dot{\epsilon} = 4 \times 10^{-6}$/s, the strain rate was increased in steps to 3×10^{-2}/s. This structure with a 54 μm grain size and almost no evidence of recrystallization is probably representative of the structure present after the initial 20 pct strain at $\dot{\epsilon} = 4 \times 10^{-6}$/s.

occur in the fine-grain regions. Thus, the viscous glide deformation mechanism in the large grains would then be rate-controlling because it is the slower of the two processes required for deformation.

Whereas specimens deformed at 670°C and $\dot{\varepsilon} \cong 10^{-5}$/s soften with strain, specimens at 1000°C show hardening. According to microstructural evidence, this hardening is probably due to subgrain formation and grain growth. The microstructure at 1000°C after deformation at $\dot{\varepsilon} = 3 \times 10^{-2}$/s, Fig. 6.9, shows some grains containing subgrains and others (which probably formed by recrystallization) containing no subgrains. In the same longitudinal section, grains in the "dead zones" at the top and bottom of the longitudinal section (total strain was $\varepsilon = 0.67$) were 54 μm in size and subgrains were evident near grain boundaries, Fig. 6.14. Almost no recrystallized grains are seen in Fig. 6.14. The 54 μm grain size is probably representative of the structure present after the initial 20 pct strain at $\dot{\varepsilon} = 4 \times 10^{-6}$/s. The recrystallized grains in Fig. 6.9 are about the same size as the original grain size (40 μm) and would not be consistent with the observed hardening under initial straining. After the strain rate was increased in steps to 3×10^{-2}/s (where the strain interval was $\Delta\varepsilon = 0.2$), recrystallization probably occurred in the heavily deformed regions (and not in the "dead zones" present at large strains) where the local flow stress was high. It is not known whether recrystallization occurred during deformation in the strain interval $\Delta\varepsilon \cong 0.2$ at 3×10^{-2}/s or after unloading before quenching.

The microstructures indicate that strain hardening at 1000°C and $\dot{\varepsilon} \cong 4 \times 10^{-6}$ is probably due to an increase in grain size from 40 to 54 μm and subgrain formation. Hardening due to subgrain formation is

simply normal primary creep [Cf. Bird et al. (1969)]. Class I solid solution alloys (n = 3) typically show a small primary or an inverted primary during creep at constant stress [Bird et al. (1969)], indicating that subgrains may not develop. However, microstructural evidence that subgrains do not form when a viscous glide creep mechanism is rate-controlling is found for only two systems: W-25Re [Vandervoort and Barmore (1969)]; Al-5.1Mg (at. pct) and Al-6.9Mg (at. pct) [Horiuchi and Otsuka (1972)]. However, in other work on Al-Mg alloys, x-ray back reflection photographs indicated that subgrains did form during creep of Al-1.62Mg. (at. pct) [Sherby and Dorn (1953)] and Al-2.1Mg [Sherby et al. (1956)]. Thus the evidence that subgrains do not form in Class I alloys is very weak.

Micrographs for the U-7.5Nb-2.5Zr alloy show that subgrains do form during deformation at all test temperatures (670 - 1000°C). The subgrain structure is initially developed near grain boundaries, probably because stress concentrations at sliding boundaries increase dislocation generation in these regions. The most developed substructure was formed after deformation at 670°C and $\dot{\epsilon} \cong 10^{-5}$/s to $\epsilon = 0.49$, Fig. 6.8. In this sample the final flow stress was 3800 psi; using the relation [Sherby and Young (1972)],

$$\lambda = 4\ b\left(\frac{\sigma}{E}\right)^{-1}$$

the subgrain size λ is calculated to be 1.9 μm. For the regions of Fig. 6.8 (bottom photo) in which subgrain boundaries are delineated by the etch, this calculated value is about equal to the observed subgrain size.

The present investigation suggests that subgrains can develop in

alloys deforming by the viscous glide creep mechanism. This observation indicates that dislocation mobility is great enough to allow formation of a periodic dislocation array with a net decrease in free energy [Holt (1970)].

Although the creep data in Fig. 6.5 at $\varepsilon = 0.20$ was taken at constant strain (and, therefore, constant structure), the structure is different at each temperature. The structure at each temperature was determined after a 20 pct strain interval at $\dot{\varepsilon} \cong 10^{-5}/s$. The structures ranged from a heterogeneous grain size distribution involving ~6 μm grains and 30 - 40 μm grains at 670°C to a relatively homogeneous ≈54 μm grain size structure at 1000°C. Subgrains were observed at all temperatures, except in the recrystallized small grains. Because the structure varies with test temperature, it would not be meaningful to calculate an activation energy for the creep data obtained at $\varepsilon = 0.20$.

Conclusions

When annealed to form a single γ phase with a 40 μm grain size, the U-7.5Nb-2.5Zr alloy deformed by a viscous glide creep mechanism during initial straining ($\varepsilon = 0.01$) at 670 - 1000°C. The creep equation was found to be:

$$\frac{\dot{\gamma}\, k\, T}{D_L\, G\, b} = 11 \left(\frac{\tau}{G}\right)^3$$

The measured creep activation energy was 51 kcal/mole, which is in reasonable agreement with the 54.9 to 59.7 kcal/mole range calculated for the average lattice diffusion coefficient in the ternary alloy. Power law breakdown was found to occur at $\tau/G \cong 2 \times 10^{-3}$. This stress is higher than that for power law breakdown in a dislocation climb-controlled creep mechanism, but is reasonable in realtion to other

viscous glide creep data.

Structural changes occurred during deformation at 670 - 1000°C. At stresses less than about 1600 psi, hardening was observed which was related to subgrain formation and grain growth. At stresses greater than about 1600 psi, softening occurred. The softening was related to the formation of small recrystallized grains at grain boundaries, the probable mechanism being a grain boundary shear and migration process. Subgrains formed during deformation at all temperatures, especially near grain boundaries. Constant structure tests at $\varepsilon = 0.20$ (after an initial 20 pct strain at $\dot{\varepsilon} \approx 10^{-5}/s$) showed a three-power stress exponent at all temperatures, indicating that the viscous glide creep mechanism was probably operative after structural changes occurred.

CHAPTER VII

SUMMARY AND CONCLUSIONS

The elevated temperature deformation behavior of a monotectoid-composition U-7.5Nb-2.5Zr alloy was studied in the temperature range 500 - 1000°C as a function of microstructure. The major results and conclusions are outlined in the following paragraphs.

The lamellar $\alpha + \gamma_1$ structure (0.1 - 0.5 μm interlamellar spacing) formed by isothermal transformation was stable for at least 24 h during annealing at temperatures just below the monotectoid temperature (≈637°C or $0.56T_m$). Concurrent deformation during annealing greatly enhanced the rate of spheroidization, but the spheroidization kinetics were slower than observed in a eutectoid-composition Fe-C alloy at the same homologous temperature and strain rate. This difference is probably due to a difference in grain boundary diffusion coefficients or a difference in the surface energy of the phase boundaries for the two materials. Although incomplete spheroidization was observed after strains as large as $\varepsilon = 1.9$, the results are in qualitative agreement with spheroidization mechanisms proposed for steels. The activation energy for spheroidization was found to be about that estimated for grain boundary diffusion in the γ_1 phase. A high stress deformation condition led to a finer spheroidite size than a low stress condition, consistent with a model for deformation-enhanced spheroidization where subgrain boundaries act as high diffusivity paths and spheroidite spacing is related to the subgrain size.

A fine-grain equiaxed $\alpha + \gamma_1$ structure can be most efficiently produced by employing a quench-cold work-anneal treatment before hot working.

An equiaxed structure with a 0.5 μm grain size was produced by gamma quenching, cold working to $\varepsilon = 0.5$, annealing at 550°C for 24 h and hot working at 600°C to $\varepsilon = 1.5$ (total strain).

The equiaxed $\alpha + \gamma_1$ structure with a stable 1.7 μm grain diameter was superplastic only at temperatures immediately below the monotectoid temperature. At 635°C, maximum elongations were about 550 pct. Superplastic creep (625 - 636°C) was described by the phenomenological equation,

$$\frac{\dot{\gamma}\, k\, T}{D_B\, G\, b} = 485 \left(\frac{b}{d}\right)^2 \left(\frac{\tau}{G}\right)^2 \qquad (7\text{-}1)$$

for which general agreement with data of other superplastic materials is reported. In Eq. (7-1), $\dot{\gamma}$ is the shear strain rate, k is Boltzmann's constant, T is the absolute temperature, D_B is the grain boundary diffusion coefficient, G is the shear modulus, b is Burgers vector, d is the grain diameter and τ is the shear stress.

At high stresses where $\tau/G > 10^{-3}$ there was a transition from superplastic creep to dislocation climb-controlled creep where the stress exponent is 5. Creep data at 550 - 600°C were in this transition range centered at $\tau/G \cong 10^{-3}$, while data at 500 - 525°C exhibited only five-power creep.

Because the composition of the γ_1 phase changed significantly in the range 500 - 625°C and because the diffusion coefficient is sensitive to the Nb and Zr content, the diffusion coefficient in the γ_1 phase was strongly temperature-sensitive. An apparent activation energy for lattice diffusion at equilibrium γ_1 composition was calculated to be 130 kcal/mole between 500 and 625°C. This value compares favorable with an average value of 123 kcal/mole calculated from creep data at 513 - 613°C. Therefore, in the dislocation climb region and the transition region, creep is believed to be controlled by lattice diffusion. The creep activation energy

at 631°C was about 60 kcal/mole, which was related to grain boundary diffusion and is consistent with superplastic creep behavior.

Grain boundary sliding with accommodation at grain corners is the mechanism most consistent with experimental observations for superplastic flow. An observed decrease in fiber texture during superplastic flow is most likely due to grain rotation and the relatively minor contribution of dislocation slip compared to the slip-recovery or dislocation climb-controlled creep mechanism. The accommodation mechanism is probably largely diffusion-controlled grain boundary migration, although no theory has been developed for this mechanism which agrees with observed creep behavior.

When annealed to form a single γ phase with a 40 μm grain size, the U-7.5Nb-2.5Zr alloy deformed by a viscous glide creep mechanism during initial straining ($\varepsilon = 0.01$) at 670 - 1000°C. The creep equation was found to be:

$$\frac{\dot{\gamma}\, k\, T}{D_L\, G\, b} = 11 \left(\frac{\tau}{G}\right)^3$$

where D_L is the lattice diffusion coefficient. The measured creep activation energy was 51 kcal/mole, which is in reasonable agreement with the 54.0 to 59.7 kcal/mole range calculated for the average lattice diffusion coefficient in the ternary alloy. Power law breakdown was found to occur at $\tau/G \cong 2 \times 10^{-3}$. This stress is higher than that for power law breakdown in a dislocation climb-controlled creep mechanism, but is reasonable in relation to other viscous glide creep data.

Structural changes occurred during deformation at 670 - 1000°C. At stresses less than about 1600 psi, hardening was observed which was related to subgrain formation and grain growth. At stresses greater than

about 1600 psi, softening occurred. The softening was related to the formation of small recrystallized grains at grain boundaries, the probable mechanism being a grain boundary shear and migration process. Subgrains formed during deformation at all temperatures, especially near grain boundaries. Constant structure tests at $\epsilon = 0.20$ (after an initial 20 pct strain at $\dot{\epsilon} \cong 10^{-5}$/s) showed a three-power stress exponent at all temperatures, indicating that the viscous glide creep mechanism was probably operative after structural changes occurred.

A comparison of creep data for the fine-grain equiaxed $\alpha + \gamma_1$ structure at 500 - 636°C with creep data at 670 - 1000°C for the single-phase structure with a 40 μm grain size shows the considerable weakening effect obtained at high temperature by a grain size refinement. The fine-grain structure at 636°C is in fact weaker than the coarse-grain structure at 1000°C for strain rates $\leq 10^{-3}$/s. For the strain rate range 10^{-6} to 10^{-3}/s, the fine-grain structure at 550°C has about the same flow stress as the coarse-grain structure at 670°C. At higher strain rates the weakening effect of grain size refinement is slightly less. For example, at a strain rate of 10^{-1}/s, the flow stress of the fine-grain structure at 636°C is about the same as the coarse-grain structure at 900°C.

In terms of hot forming operations, the fine-grain equiaxed $\alpha + \gamma_1$ structure allows the forming temperature to be markedly reduced from that required for the coarse-grain structure at a constant energy input. Lower forming temperatures could significantly reduce surface oxidation for the U-7.5Nb-2.5Zr alloy.

In terms of possible engineering applications for the fine-

grain equiaxed $\alpha + \gamma_1$ structure developed in the U-7.5Nb-2.5Zr alloy in this investigation, room temperature stress-strain curves are shown in Fig. 7.1 for data obtained by Wood (1972). The yield strength at 0.2 pct plastic strain is 153,000 psi but rapid strain hardening increases the flow stress to 207,000 psi at $\varepsilon = 0.03$. Tensile elongation is 10 pct (for a gage length/diameter ratio of four). Compared to gamma-quenched and aged treatments producing these strength levels [Peterson and Vandervoort (1964) and Jackson and Boland (1971)], the fine-grain equiaxed $\alpha + \gamma_1$ structure offers improved ductility. One sample was deformed to $\varepsilon = 0.59$ in compression (Fig. 7.1) with only one small surface crack observed.

Finally, in Fig. 7.2 the flow stress at $\dot{\varepsilon} = 10^{-4}/s$ is plotted versus temperature from 22 to 1000°C for the fine-grain $\alpha + \gamma_1$ structure and the coarse-grain γ structure. The fine-grain structure is strong at room temperature, but weak at high temperature compared to the coarse-grain structure. The superplastic range for the fine-grain structure is also shown in Fig. 7.2.

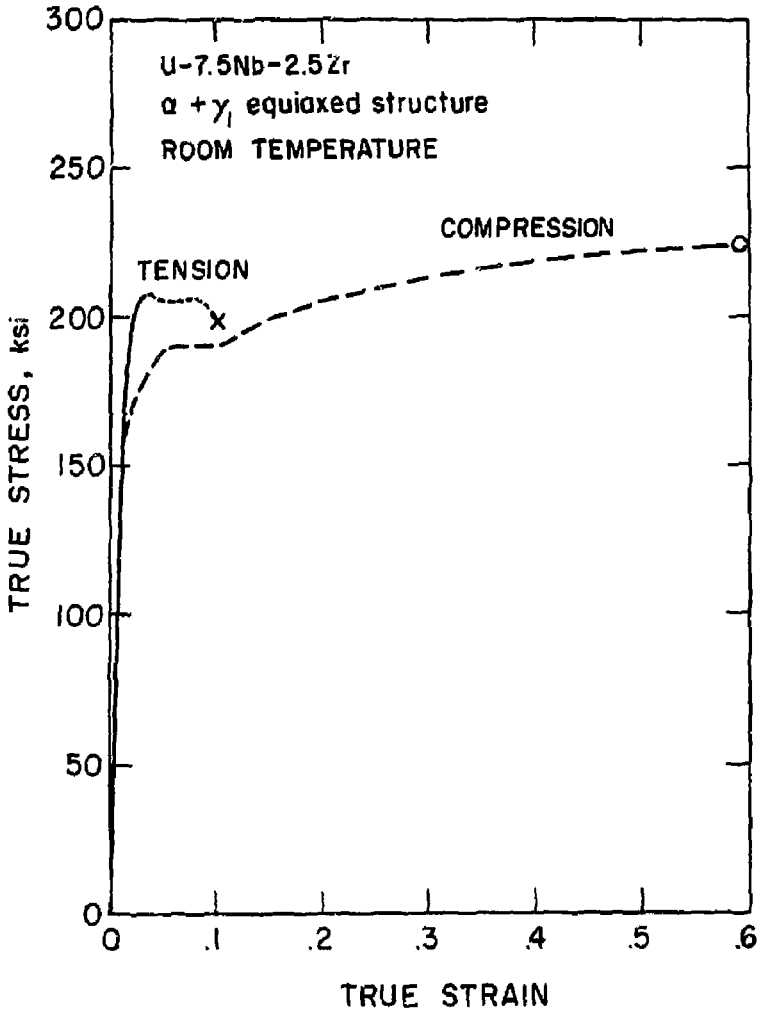

Fig. 7.1. Room temperature true stress-true strain curves for the U-7.5Nb-2.5Zr alloy optimally processed to achieve an equiaxed $\alpha + \gamma_1$ microstructure with a grain size of 0.5 μm. The yield stress at 0.2 pct plastic strain is 153,000 psi. The material work hardens to 207,000 psi at $\varepsilon = 0.03$ before local deformation (as suggested by the maximum in the load-extension curve) occurs, although the flow stress calculated assuming uniform elongation does not drop below 205,000 psi until $\varepsilon = 0.08$. Total elongation in 1 in. was 10 pct. In compression the stress-strain curve is not accurately defined except at the end point because of difficulties in compensating for deformation of thin teflon sheets used as a lubricant and extensometer errors.

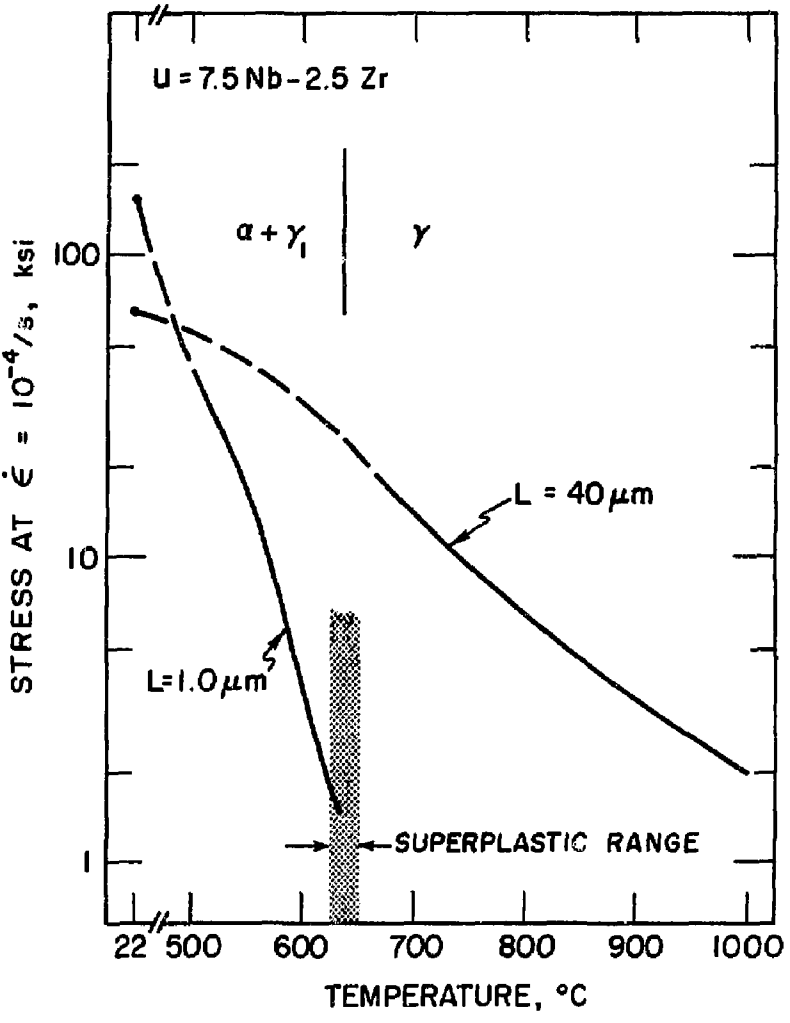

Fig. 7.2. The flow stress at $\dot{\epsilon} = 10^{-4}/s$ is plotted versus temperature for the fine-grain $\alpha + \gamma_1$ structure (L = 1.0 μm) and the coarse-grain γ structure (L = 40 μm). Room temperature flow stresses [Wood (1972)] are taken as the 0.2 pct offset yield strength. The superplastic temperature range is indicated.

APPENDIX A

A COMPUTER PROGRAM FOR THE INSTRON MACHINE

The general features of the computer program which computes true stress, true strain and true strain rate from Instron load-time curves are described in Chapter III. The purpose of this appendix is to illustrate how to use the program.

Language

The computer program is written in WATFIV, a fast, one-pass FORTRAN IV compiler for the IBM/360. Two subroutines (ATSG and ALI) used for interpolation between data points were taken from the IBM System/360 Scientific Subroutine Package, Version III. Subroutine DERIV, used to find the derivative of a curve at a point, was written independently. The text of the program is shown in Fig. A.1.

Data Input

Each line enclosed in parentheses below represents one input card with WATFIV format-free input (the parentheses are not part of data input):

Machine Stiffness

(temp, xhd1, chart1, scale1, load2 min, xhd2, chart2, scale2)

(X,Y)	Data Set 1	Optional
(-1,0)	End Data Set 1	req'd.
(X,Y)	Data Set 2	req'd. if Data Set 1 is used
(-1,0)	End Data Set 2	req'd.

Compression

(test no. > 0, run no., temp, xhd, chart, scale, length, diam)

Tension

(test no. < 0, length, temp, xhd, chart, scale, width, thickness)

or: ..., diam, -1)

Compression or Tension

(load mult. factor, load add. term, $n = d \ln\sigma / d \ln\dot{\varepsilon}$)

(X,Y)

	(-2,0)	change xhd or chart or
	(xhd, chart, scale)	scale to these new values
or:	(-1,0)	end of test
or:	(-9,0)	call new machine stiffness data
or:	(-99,0)	end of all data

Notes

1. The machine stiffness data are divided into two data sets so that data at low loads, e.g.,0 - 10001b, can be accurately specified along with high load data, e.g., 1000 - 10000 1b.

2. "Test no." must be an integer; other numbers are real, but a decimal point is not required.

3. Units are: temp, °C; xhd and chart, in/min; scale and load2 min, 1b; length, diam, width, thickness--inches.

4. (X,Y) are successive cards of data pairs where X is the time scale value (inches of chart) and Y is the load scale value (inches of chart).

5. The load multiplication factor and additive term (lb) are used to correct for a calibration error in the load cell and an incorrect zero setting on the chart paper.

6. Note that all tension or compression data sets end with a negative

value for X, and all endings except (-99,0) require additional data to follow.

7. Several interrupted compression tests on the same sample can be run if a "-1" is written for "length" on the second and following tests. The final calculated specimen length will be passed as the initial length to the following data set. In this case each test will begin at zero strain.

Data Output

The data output gives one page for each strain interval at constant crosshead speed. Typical data output, including stiffness data, are shown in Fig. A.2. Most of the output format is self-explanatory, and only brief comments will be made.

The error column ("ERR") is the error code for the interpolation subroutine ALI used with the machine stiffness curve: (0) no error; (1) the required accuracy could not be reached because of rounding errors; (2) the required accuracy could not be reached with the number of points used -- increase the number of machine stiffness points; (3) two points have the same "Y" value. The first "J" column gives the number of machine stiffness points used in the interpolation, and the last "J" column gives the number of points used to calculate the strain rate correction in subroutine DERIV. The first stress column is the calculated stress at the given strain rate; the second stress column is the stress corrected to the median strain rate for that data set. The median strain rate is easily identified as the value on the line where the two stress values are equal.

Fig. A.1. Computer Program Listing

```
$WATFIV
      REAL LO,LOAD,L,M,MACHL(40),LEND
      INTEGER TEST
      DIMENSION X(40),Y(40),STRAIN(40),WORK(40),ARG(40),VAL(40),STRESS(4
     CO),STRNRT(40), TIME(40),MERR(40),JN(40),DYDX(40),J(40),NEND(5),CH(
     C5),SC(5),E(40)
2     CALL ML
1     READ,TEST,RUN,TEMP,XHEAD,CH(1),SC(1),LO,DO
      READ,FM,FA,M
      XEND=0.
      DELT=0.
      IIII=TEMP
      IF(LO.GT.0.) GO TO 5
      LO=LEND
      DO=DEND
5     IF(TEST)4,4,3
3     II=RUN
      WRITE(6,101)TEST,CH(1),II ,SC(1),IIII,LO,XHEAD,DO
101   FORMAT('1','TEST NO. = ',I3,29X,'CHART SPEED (IN/MIN) = ',F5.2/' R
     CUN NO. = ',I3,  30X,'SCALE (LBS) = ',F6.0/' TEMPERATURE = ',I4,'C'
     C,24X,'INITIAL LENGTH (IN) = ',F6.4/' CROSSHEAD SPEED (IN/MIN) = ',
     CF8.5,8X,'INITIAL DIAMETER (IN) = ',F6.4)
      A=3.141593*DO**2/4.
      B=-1.
      GO TO 109
4     L=RUN
      W=LO
      T=DO
      WRITE(6,105)TEST,SC(1),IIII,L,XHEAD,W,CH(1),T
105   FORMAT('1','TEST NO. = ',I4,28X,'SCALE (LBS) = ',F6.0/' TEMPERATUR
     CE = ',I3,'C',25X,'INITIAL LENGTH (IN) = ',F7.4/' CROSSHEAD SPEED (
     CIN/MIN) = ',F8.5,8X,'INITIAL WIDTH (IN) = ',F6.4/' CHART SPEED (IN
     C/MIN) = ',F5.2,15X,'INITIAL THICKNESS (IN) = ',F6.4)
      IF(T)107,107,106
106   A=W*T
      GO TO 108
107   A=3.141593*W**2/4.
108   LO=L
      B=1.
109   WRITE(6,104)FM,FA,M
104   FORMAT(' LOAD CALIBRATION FACTOR = ',F5.3,'; ',F5.1,' LB  M = ',F
     *5.3/)
103   NO=1
      DO 22 K=1,5
      DO 21 N=NO,30
      READ,X(N),Y(N)
      IF(X(N))20,21,21
21    CONTINUE
20    NEND(K)=N-1
      IF(X(N).NE.-2)GO TO 23
      READ,XHD,CH(K+1),SC(K+1)
      IF(XHD.NE.XHEAD)GO TO 23
22    NO=N
23    N=N-1
      WRITE(6,102)N
102   FORMAT(' ','STRAIN',10X,'STRESS (PSI)',4X,'STRAIN RATE (1/SEC)',10
     CX,'X',5X,'Y',4X,I2/' ',7X,'ERR J',3X,'(M=0)    (M=M)',16X,'(CORRECT
     CION)',17X,'J')
      IS=1
      DO 40 KK=1,K
```

```
      IEND=NEND(KK)
      DO 30 I=IS,IEND
      DELTAL=DELT+(X(I)-XEND)*XHEAD/CH(KK)
      LOAD=Y(I)*.1*SC(KK)*FM+FA
      CALL MINTRP(LOAD,MACHL(I),MERR(I),JN(I))
42    E(I)= (DELTAL-MACHL(I))/LO*8
      IF(1.+E(I))54,54,36
36    STRAIN(I)=ALOG(1.+E(I))*R
34    STRESS(I)=LOAD/A*(1.+E(I))
      STRNRT(I)=XHEAD/60./LC/(1.+E(I))
30    TIME(I)=DELTAL*60./XHEAD
      IS=NEND(KK)+1
      DELT=DELTAL
40    XEND=X(IEND)
35    DO 37 I=1,N
      NN=N
      CALL ATSG(TIME(I),TIME,MACHL,WORK,N,ARG,VAL,NN)
      CALL DER(V(ARG,VAL,NN,DYDX(I),J(I))
      DYDX(I)=DYDX(I)/LO/(1.+E(I))
      STRNRT(I)=STRNRT(I)-DYDX(I)
37    DYDX(I)=DYDX(I)/(STRNRT(I)+DYDX(I))*100.
      IS=1
      DO 45 KK=1,K
      IEND=NEND(KK)
      DO 38 I=IS,IEND
      IF(M.EQ.0.) GO TO 39
      IF(STRNRT(I))32,32,33
32    S=0.
      GO TO 38
33    S=STRESS(I)*(STRNRT(N/2+1)/STRNRT(I))**M
      GO TO 38
39    S=STRESS(I)
38    WRITE(6,31)STRAIN(I),MERR(I),JN(I),STRESS(I),S,STRNRT(I),DYDX(I),X
     C(I),Y(I),J(I)
31    FORMAT('0',F6.3,2I3,F9.0,F8.0,F14.9,F11.3,' %',F8.2,F6.2,I4)
      IF(KK.EQ.K)GO TO 53
      WRITE(6,46)CH(KK+1),SC(KK+1)
46    FORMAT('0','CHART SPEED (IN/MIN) = ',F4.1,16X,'SCALE (LBS) = ',F6.
     *0)
45    IS=NEND(KK)+1
53    LEND=LO*(1.+E(IEND))
      DEND=DO*SQRT(LO/LEND)
54    IF(X(N+1).NE.-2)GO TO 52
      XHEAD=XHD
      CH(1)=CH(K+1)
      SC(1)=SC(K+1)
      WRITE(6,55)XHEAD,TEST,CH(K+1),SC(K+1)
55    FORMAT('1','CROSSHEAD SPEED (IN/MIN) = ',F7.4,27X,'TEST NO. ',I4/
     C' CHART SPEED (IN/MIN) = ',F4.1/' SCALE (LBS) = ',F6.0///)
      GO TO 103
52    IF(X(N+1).EQ.-9) GO TO 2
      IF(X(N+1).NE.-99) GO TO 1
      STOP
      END
      SUBROUTINE ATSG(X,Z,F,WORK,IROW,ARG,VAL,NDIM)
      DIMENSION Z(30),F(30),WORK(30),ARG(30),VAL(30)
      IF(IROW)11,11,1
1     N=NDIM
      IF(N-IROW)3,3,2
2     N=IROW
```

```
      NDIM=IROW
3     B=0.
      DO 5 I=1,IROW
      DELTA= ABS(Z(I)-X)
      IF(DELTA-B)5,5,4
4     B=DELTA
5     WORK(I)=DELTA
      B=B+1.
      DO 10 J=I,N
      DELTA=B
      DO 7 I=1,IROW
      IF(WORK(I)-DELTA)6,7,7
6     II=I
      DELTA=WORK(I)
7     CONTINUE
      ARG(J)=Z(II)
9     VAL(J)=F(II)
10    WORK(II)=B
11    RETURN
      END
      SUBROUTINE DERIV(X,Y,N,DYDX,J)
      DIMENSION X(30),Y(30),DER(30),D(30)
      IF(N.LE.1)GO TO 31
      IF(X(1).EQ.X(2)) GO TO 31
      D(1)=Y(1)/(X(1)-X(2))
      D(2)=Y(2)/(X(2)-X(1))
      DER(2)=D(1)+D(2)
      IF(N.EQ.2) GO TO 32
      DELT2=0.
      DO 10 J=3,N
      DELT1=DELT2
      K=J-1
      DO 15 I=1,K
      Z=X(I)-X(J)
      IF(Z.EQ.0.) GO TO 30
15    D(I)=D(I)*(X(I)-X(K))/Z
      Z=X(J)-X(I)
      IF(Z.EQ.0.) GO TO 30
      D(J)=Y(J)/Z
      DO 20 M=2,K
      Z=X(J)-X(M)
      IF(Z.EQ.0.) GO TO 30
20    D(J)=D(J)*(X(I)-X(M))/Z
      DER(J)=DER(J-1)
      DO 25 I=1,J
25    DER(J)=DER(J)+D(I)
      DELT2=ABS(DER(J)-DER(J-1))
      IF(J-5)10,11,11
11    IF(DELT2-DELT1)10,30,30
10    CONTINUE
      J=N
      DYDX=DER(J)
      RETURN
30    J=J-1
      DYDX=DER(J)
      RETURN
31    DYDX=0.
      J=0
      RETURN
32    DYDX=DER(2)
```

```
      J=2
      RETURN
      END
      SUBROUTINE ALI(X,ARG,VAL,Y,NDIM,EPS,IER,J)
      DIMENSION ARG(30),VAL(30)
      IER=2
      DELT2=0.
      IF(NDIM-1)9,7,1
1     DO 6 J=2,NDIM
      DELT1=DELT2
      IEND=J-1
      DO 2 I=1,IEND
      H=ARG(I)-ARG(J)
      IF(H)2,13,2
2     VAL(J)=(VAL(I)*(X-ARG(J))-VAL(J)*(X-ARG(I)))/H
      DELT2= ABS(VAL(J)-VAL(IEND))
      IF(J-2)6,6,3
3     IF(DELT2-EPS)10,10,4
4     IF(J-5)6,5,5
5     IF(DELT2-DELT1)6,11,11
6     CONTINUE
7     J=NDIM
8     Y=VAL(J)
9     RETURN
10    IER=0
      GO TO 8
11    IER=1
12    J=IEND
      GO TO 8
13    IER=3
      GO TO 12
      END
      SUBROUTINE ML
      REAL L1MAX
      DIMENSION X1(30),Y1(30),X2(30),Y2(30),ARG(30),VAL(30),WORK(30)
      INTEGER TEMP,SCALE1,SCALE2
      READ,TEMP,XHD1,CHART1,SCALE1,L1MAX,XHD2,CHART2,SCALE2
      WRITE(6,10)TEMP,L1MAX,L1MAX,XHD1,XHD2,CHART1,CHART2,SCALE1,SCALE2
10    FORMAT('1',10X,'MACHINE  STIFFNESS  DATA:   TEMPERATURE = ',I4,'C'
     C///' LOADS LESS THAN ',F6.0,' LBS',12X,'LOADS GREATER THAN ',F6.0,
     C' LBS'//' CROSSHEAD SPEED (IN/MIN) = ',F7.4, 4X,'CROSSHEAD SPEED (
     CIN/MIN) = ',F7.4/' CHART SPEED (IN/MIN) = ',F4.1,11X,'CHART SPEED
     C(IN/MIN) = ',F4.1/' SCALE (LBS) = ',I5,19X,'SCALE (LBS) = ',I5///)
      DO 20 N1=1,30
      READ,X1(N1),Y1(N1)
      IF(X1(N1).LT.0.) GO TO 30
20    CONTINUE
30    DO 31 N2=1,30
      READ,X2(N2),Y2(N2)
      IF(X2(N2).LT.0.) GO TO 40
31    CONTINUE
40    WRITE(6,41)
41    FORMAT('0',4X,'X',6X,'Y',36X,'X',6X,'Y'/)
      DO 42 I=1,30
      IF(I.GT.N1-1) GO TO 43
      IF(I.GT.N2-1) GO TO 44
45    FORMAT(' ',2F7.2,30X,2F7.2)
42    WRITE(6,45)X1(I),Y1(I),X2(I),Y2(I)
43    IF(I.EQ.N2-1) GO TO 69
      N=N2-1
```

```
      IF(N)69,69,59
59    DO 60 J=I,N
61    FORMAT(' ',44X,2F7.2)
60    WRITE(6,61)X2(J),Y2(J)
      RETURN
44    IF(I.EQ.N1-1) GO TO 69
      N=N1-1
      DO 62 J=I,N
63    FORMAT(' ',2F7.2)
62    WRITE(6,63)X1(J),Y1(J)
69    RETURN
      ENTRY MINTRP(ALOAD,AMACHL,MERR,L)
      IF(ALOAD.LT.L1MAX) GO TO 50
      IF(N2-1)70,70,51
51    Y=ALOAD/.1/SCALE2
      NN=6
      CALL ATSG(Y,Y2,X2,WORK,N2-1,  ARG,VAL,NN)
      CALL ALI(Y,ARG,VAL,X,NN,.005,IER2,J)
      L=J
      MERR=IER2
      AMACHL=X*XHD2/CHART2
      RETURN
50    IF(N1-1)70,70,52
52    Y=ALOAD/.1/SCALE1
      NN=6
      CALL ATSG(Y,Y1,X1,WORK,N1-1,  ARG,VAL,NN)
      CALL ALI(Y,ARG,VAL,X,NN,.005,IER1,J)
      L=J
      MERR=IER1
      AMACHL=X*XHD1/CHART1
      RETURN
70    AMACHL=0.
      MERR=0
      L=0
      RETURN
      END
$DATA
      DATA
$STOP
```

MACHINE STIFFNESS DATA: TEMPERATURE = 607C

LOADS LESS THAN 1000. LBS

CROSSHEAD SPEED (IN/MIN) = 0.0050
CHART SPEED (IN/MIN) = 5.0
SCALE (LBS) = 1000

X	Y
0.00	0.00
0.30	0.20
0.60	0.55
0.90	1.00
1.20	1.50
1.60	2.10
2.00	2.60
2.35	3.00
2.75	3.50
3.17	4.00
3.50	4.39
3.80	4.70
4.07	5.00
4.30	5.25
4.60	5.55
4.90	5.76
5.30	5.96
5.63	6.14
5.74	6.30
5.86	6.50
6.10	6.84
6.40	7.27
6.94	8.00
7.63	9.00
8.24	10.00

LOADS GREATER THAN 1000. LBS

CROSSHEAD SPEED (IN/MIN) = 0.0200
CHART SPEED (IN/MIN) = 5.0
SCALE (LBS) = 10000

X	Y
2.06	1.00
2.14	1.10
2.30	1.19
2.40	1.20
2.50	1.21
2.63	1.30
2.80	1.44
3.10	1.70
3.46	2.00
3.90	2.44
4.40	3.00
4.90	3.55
5.28	4.00
6.10	5.00
6.94	6.00
7.75	7.00
8.55	8.00
9.36	9.00
10.16	10.00

Fig. A.2. Typical Computer Output--Machine Stiffness Data

TEST NO. = 119
RUN NO. = 1
TEMPERATURE = 600C
CROSSHEAD SPEED (IN/MIN) = 0.00008
LOAD CALIBRATION FACTOR = 1.080; 0.0 LB

CHART SPEED (IN/MIN) = 0.02
SCALE (LBS) = 200.
INITIAL LENGTH (IN) = 0.4503
INITIAL DIAMETER (IN) = 0.2998
M = 0.390

STRAIN	ERR	J	STRESS (PSI) (M=0)	STRESS (PSI) (M=M)	STRAIN RATE (1/SEC)	(CORRECTION)	X	Y	3 J
0.010	0	3	1303.	1311.	0.000002902	2.921 %	1.30	4.30	3
0.011	0	3	1340.	1340.	0.000002947	1.593 %	1.50	4.43	3
0.016	0	3	1334.	1316.	0.000003056	-1.593 %	1.98	4.43	3

CROSSHEAD SPEED (IN/MIN) = 0.00050
CHART SPEED (IN/MIN) = 0.2
SCALE (LBS) = 200.

TEST NO. 119

STRAIN	ERR	J	STRESS (PSI) (M=0)	STRESS (PSI) (M=M)	STRAIN RATE (1/SEC)	(CORRECTION)	X	Y	6 J
0.020	0	3	2160.	2213.	0.000018092	4.169 %	2.86	7.20	6
0.024	0	3	2240.	2262.	0.000018803	0.811 %	3.60	7.50	6
0.032	0	3	2220.	2225.	0.000019135	-0.138 %	5.00	7.49	6
0.045	0	3	2253.	2253.	0.000019262	0.461 %	7.20	7.70	4
0.055	0	3	2259.	2247.	0.000019531	0.124 %	9.00	7.80	4
0.062	0	3	2240.	2219.	0.000019740	-0.236 %	10.20	7.79	4

Fig. A.2 (cont.) Typical Computer Output--Test Data

REFERENCES

Y. Adda and A. Kirianenko, J. Nucl. Mat. 6 (1962) 130.

C. N. Ahlquist and R. A. Menezes, Mater. Sci. Eng. 7 (1971) 223.

T. H. Alden, Acta Met. 15 (1967) 469.

T. H. Alden, Trans. ASM 61 (1968) 559.

T. H. Alden, J. Australian Inst. Metals 14 (1969) 209.

F. J. Ansuini and F. A. Badia, Met. Trans. 4 (1973) 15.

A. J. Ardell, Acta Met. 11 (1963) 591.

P. E. Armstrong and H. L. Brown, Trans. AIME 230 (1964) 962.

P. E. Armstrong and H. L. Brown, Trans. ASM 58 (1965) 30.

P. E. Armstrong, D. T. Eash and J. E. Hockett, to be published in J. Nucl. Mat. (1973b).

P. E. Armstrong, W. V. Green, O. D. Sherby and E. G. Zukas, submitted to Acta Met. (1973a).

M. F. Ashby, Scrip. Met. 3 (1969) 843.

D. H. Avery and W. A. Backofen, Trans. ASM 58 (1965) 551.

D. H. Avery and J. M Stuart, in Surfaces and Interfaces II, Physical and Mechanical Properties, ed. J. J. Burke, N. L. Reed and V. Weiss, Syracuse University Press, Syracuse, N.Y., p. 371 (1968).

W. A. Backofen, F. J. Azzarto, G. S. Murty and S. W. Zehr, in Ductility, American Society for Metals, Metals Park, Ohio, p. 279 (1968).

T. A. Badayeva and R. I. Kuznetsova, Russian Met. 1971 (2), 126 (1971).

A. Ball and M. M. Hutchison, Metal Sci. J. 3 (1969) 1.

A. A. Baranov, Russian Met. 1969 (3) 82 (1969).

C. R. Barrett and O. D. Sherby, Trans. AIME 233 (1965) 1116.

G. Beghi, R. Matera and G. Piatti, J. Mater. Sci. 5 (1970) 820.

J. E. Bird, A. K. Mukherjee and J. F. Dorn, in Quantitative Relation Between Properties and Microstructure, ed. D. G. Brandon and A. Rosen, Israel Universities Press, p. 255 (1969).

D. L. Bly, Y. Mishchenkov, O. D. Sherby and C. M. Young, to be published in J. Mater. Sci. (1973a).

D. L. Bly, R. A. White and O. D. Sherby, Research in Progress, Dept. of Materials Science and Engineering, Stanford University, Stanford, California (1973b).

V. A. Bugrov, V. K. Grigorovich and O. S. Ivanov, in AEC report no. AEC-tr-7212, p. 69 (1972).

V. A. Bugrov, V. K. Grigovovich, A. N. Kobylkin and O. S. Ivanov, Industrial Laboratory 34 (1968) 1194.

J. J. Burke and V. Weiss (Eds.), Ultrafine-Grain Metals, Syracuse University Press, Syracuse, New York (1970).

B. R. Butcher, G. C. Weatherly and H. R. Pettit, Metal. Sci. J. 3 (1969) 7.

W. R. Cannon, Phil. Mag. 25 (1972) 1489.

W. R. Cannon and W. D. Nix, Phil. Mag. 27 (1973) 9.

W. R. Cannon and O. D. Sherby, Met. Trans. 1 (1970) 1030.

P. Chaudhari, Acta Met. 15 (1967) 1777.

E. A. Chojnowski and W. J. McG Tegart, Metal Sci. J. 2 (1968) 14.

R. L. Coble, J. Appl. Phys. 34 (1963) 1679.

M. Cohen, Trans. Japan Inst. Metals 11 (1970) 145.

P. M. Cook, Proc. Conf. Properties of Materials at High Rates of Strain, Inst. Mech. Eng., London, pp. 86-97 (1957).

C. P. Cutler and J. W. Edington, Metal Sci. J. 5 (1971) 201.

G. J. Davies, J. W. Edington, C. P. Cutler and K. A. Padmanabhan, J. Mater. Sci. 5 (1970) 1091.

C. W. Dean, AEC report no. Y-1694 (1969).

G. E. Dieter, Mechanical Metallurgy, McGraw-Hill Book Co., New York, p. 509 (1961).

D. J. Dingley, in Proc. of the 3rd Annual Scanning Electron Microscope Symposium, Chicago, p. 329 (1970).

A. E. Dwight and M. H. Mueller, AEC report No. ANL-5581 (1957).

G. L. Dunlop and D. M. R. Taplin, J. Australian Inst. Metals 16 (1971) 195.

J. B. Duran and R. E. Fisher, Microstructures 2 (6), 1971, 23.

G. R. Edwards, Ph.D. Thesis, Dept. of Materials Science, Stanford University, Stanford, California (1971).

R. P. Elliott, Constitution of Binary Diagrams, First Supplement, McGraw-Hill Book Co., New York (1965).

S. F. Exell and D. H. Warrington, Phil. Mag. 26 (1972) 1121.

G. B. Fedorov, in High Purity Metals and Alloys, Fabrication, Properties and Testing, ed. V. S. Emelyanov and A. I. Evstyukhin, Plenum Press, New York, p. 65 (1967).

G. B. Fedorov, E. A. Smirnov and V. N. Gusev, Soviet At. Energy 27 (1969) 864.

G. B. Fedorov, E. A. Smirnov and V. N. Gusev, Soviet At. Energy 32 (1972) 8.

G. B. Fedorov, E. A. Smirnov and F. I. Zhomov, Metallurgiya i Metallovedenie Chistykh Metallov, No. 5, p. 92, Atomizdat, Moscow (1966).

J. C. Freche, W. J. Waters and R. L. Ashbrook, Metals Eng. Quart. 10 (1970) 58.

F. Garofalo, Fundamentals of Creep and Creep-Rupture in Metals, Macmillan Co., New York (1965).

A. E. Geckinli, Ph.D. Thesis, Dept. of Materials Science, Stanford University, Stanford, California (1973).

R. C. Gifkins, J. Inst. Metals 95 (1967) 373.

R. C. Gifkins, Optical Microscopy of Metals, American Elsevier Publishing Co., New York, p. 184 (1970).

J. Harrigan and O. D. Sherby, Mater. Sci. Eng. 7 (1971) 177.

E. W. Hart, Acta Met. 5 (1957) 597.

H. W. Hayden, S. Floreen and P. D. Goodell, Met. Trans. 3 (1972) 833.

H. W. Hayden, R. C. Gibson, H. F. Merrick and J. H. Brophy, Trans. ASM 60 (1967) 3.

C. Herring, J. Appl. Phys. 21 (1950) 437.

J. E. Hilliard, in Quantitative Microscopy, R. T. DeHoff and F. N. Rhines (eds.), McGraw-Hill Book Co., New York, p. 45 (1968).

D. L. Holt, Trans. AIME 242 (1968) 25.

D. L. Holt, J. Appl. Phys. 41 (1970) 3197.

R. Horiuchi and M. Otsuka, Trans. Japan Inst. Metals 13 (1972) 284.

R. Horiuchi, H. Yoshinaga and S. Hama, Trans. Japan Inst. Met. 6 (1965) 123.

C. A. P. Horton and C. J. Beevers, Acta Met. 16 (1968) 733.

E. M. Howard, W. L. Barmore, J. D. Mote and J. E. Dorn, Trans. AIME 227 (1963) 1061.

J. J. Irani and P. R. Taylor, Deformation Under Hot Working Conditions, Iron and Steel Inst. Pub. 108, p. 83 (1968).

Y. Ishida and M. Henderson Brown, Acta Met. 15 (1967) 857.

R. J. Jackson, AEC report no. RFP-1700 (1971).

R. J. Jackson and J. F. Boland, AEC report no. RFP-1652 (1971).

R. H. Johnson, Met. Rev. 15 (1970) 115.

R. H. Johnson, C. M. Packer, L. Anderson and O. D. Sherby, Phil. Mag. 18 (1968) 1309.

H. W. King, J. Mat. Sci. 1 (1966) 79.

T. G. Langdon, Phil. Mag. 22 (1970) 689.

S. L. Lapata and E. B. Kula, Trans. AIME 233 (1965) 288.

A. D. LeClaire, in Diffusion in Body-Centered Cubic Metals, American Society for Metals, Metals Park, Ohio, p. 3 (1965).

D. Lee, Acta Met. 17 (1969) 1057.

D. Lee, Met. Trans. 1 (1970) 1607.

D. Lee, J. Inst. Metals 99 (1971) 66.

E. U. Lee and E. E. Underwood, Met. Trans. 1 (1970) 1399.

T. L. Lin and D. McLean, Metal Sci. J. 2 (1968) 108.

W. H. McCarthy, Ph.D. Thesis, Dept. of Materials Science, Stanford University, Stanford, California (1966).

D. McLean, Phil. Mag. 23 (1971) 467.

P. J. Martin and W. A. Backofen, Trans. ASM 60 (1967) 352.

D. K. Matlock, Ph.D. Thesis, Dept. of Materials Science, Stanford University, Stanford, California (1972).

G. A. Mochalov, R. Kh. Tagirova, G. I. Terekhov and O. S. Ivanov, in AEC report no. AEC-tr-7212, p. 58 (1972).

W. B. Morrison, Trans. AIME 242 (1968) 2221.

K. L. Murty, F. A. Mohamed and J. E. Dorn, Acta Met. 20 (1972) 1009.

F. R. N. Nabarro, Report of Conference on the Strength of Solids, Phys. Soc., London, p. 75 (1948).

F. R. N. Nabarro, Phil. Mag. 16 (1967) 231.

H. Naziri and R. Pearce, J. Inst. Metals 98 (1970) 71.

R. B. Nicholson, in Electron Microscopy and Structure of Materials, ed. G. Thomas, R. M. Fulrath and R. M. Fisher, University of California Press, Berkeley, p. 689 (1972).

K. Nuttall,, J. Inst. Metals 100 (1972) 114.

C. M. Packer, R. H. Johnson and O. D. Sherby, Trans. AIME 242 (1968) 2485.

C. M. Packer and O. D. Sherby, Trans. ASM 60 (1967) 21.

H. Paqueton and A. Pineau, J. Iron Steel Inst. 209 (1971) 991.

C. A. W. Peterson and R. R. Vandervoort, AEC report no. UCRL-7869 (1964).

N. L. Peterson and R. E. Ogilvie, Trans. AIME 227 (1963) 1083.

R. Raj and M. F. Ashby, Trans. Met. 2 (1971) 1113.

R. Raj and M. F. Ashby, Met. Trans. 3 (1972) 1937.

S. H. Reichman, B. W. Castledine and J. W. Smythe, SAE J. 78 (1970) 59.

G. J. Richardson, C. M. Sellars and W. J. McG. Tegart, Acta Met. 14 (1966) 1225.

J. Robbins, O. C. Shepard and O. D. Sherby, J. Iron Steel Inst. 202 (1964) 804.

S. L. Robinson, Ph.D. Thesis, Dept. of Materials Science, Stanford University, Stanford, California (1972).

S. L. Robinson and O. D. Sherby, to be published in J. Nucl. Mat. (1973).

H. W. Schadler, Trans. AIME 242 (1968) 1281.

W. Schroeder and D. A. Webster, J. Appl. Mech. 16 (1949) 289.

O. D. Sherby and P. Burke, Prog. Mater. Sci. 13 (1968) 325.

O. D. Sherby and J. E. Dorn, Trans. AIME 197 (1953) 324.

O. D. Sherby, M. J. Harrigan, L. Chamagne and C. Sauve, Trans. ASM 62 (1969) 575.

O. D. Sherby and M. T. Simnad, Trans. ASM 54 (1961) 227.

O. D. Sherby, T. A. Trozera and J. E. Dorn, Proc ASTM 56 (1956) 789.

O. D. Sherby and C. M. Young, paper presented at the John E. Dorn Memorial Symposium, Cleveland, Ohio (1972).

F. A. Shunk, Constitution of Binary Alloys, Second Supplement, McGraw-Hill Book Co., New York (1969).

R. N. Stevens, Phil. Mag. 23 (1971) 265.

E. E. Underwood, Quantitative Stereology, Addison-Wesley Publishing Co., Reading, Mass. (1970).

J. L. Uvira and J. J. Jonas, Trans. AIME 242 (1968) 1619.

M. L. Vaidya, K. L. Murty and J. E. Dorn, submitted to J. Appl. Phys. (1972).

R. R. Vandervoort and W. L. Barmore, High Temperature Materials, 6th Plansee Seminar, ed. F. Benesovsky, Metallwerk Plansee AG., Reutte/ Tyrol (1969).

R. R. Vandervoort, A. K. Mukherjee and J. E. Dorn, Trans. ASM 59 (1966) 930.

J. L. Walter and H. E. Cline, Trans. AIME 242 (1968) 1823.

B. M. Watts and M. J. Stowell, J. Mat. Sci. 6 (1971) 228.

J. Weertman, J. Appl. Phys. 28 (1957) 1185.

J. Weertman, Trans. AIME 218 (1960) 207.

J. Weertman, Trans. ASM 61 (1968) 681.

J. Weertman, paper presented at the John E. Dorn Memorial Symposium, Cleveland, Ohio (1972).

D. H. Wood, unpublished research, Lawrence Livermore Laboratory, Livermore, California (1972).

D. A. Woodford, Trans. ASM 62 (1969) 291.

H. L. Yakel, J. Nucl. Mat. 33 (1969) 286.